Dipion Production in a 4 GeV/c π^+ d Experiment

Thesis submitted for the Degree
of Ph.D

Philip L. Woodworth

University of Birmingham

November 1973

Synopsis

A bubble chamber experiment is described using data from the C.E.R.N. 2 m bubble chamber filled with deuterium and exposed to a 4 GeV/c π^+ beam. Measurements are presented of the U.5. π^+ beam momentum, and the level of contamination in the beam is estimated. A brief review is given of the computer programs used in the processing of 2 m bubble chamber film for physics analysis.

The channel

$$\pi^+ d \rightarrow p_s\, p\, \pi^+ \pi^- \quad (\sigma = 2.10 \pm 0.17 \text{ m b}) \qquad (1)$$

is investigated and cross sections are obtained for the quasi-two-body reactions

$$\pi^+ d \rightarrow p_s\, p\, \rho^0 \qquad (\sigma = 1.21 \pm 0.16 \text{ m b}) \qquad (2)$$

and $$\pi^+ d \rightarrow p_s\, p\, f^0 \qquad (\sigma = 0.53 \pm 0.06 \text{ m b}) \qquad (3)$$

An Estabrooks and Martin amplitude analysis is made of reaction (2) using 5279 events from the mass interval

$$0.68 < M_{\pi\pi} < 0.88 \quad \text{GeV}/c^2$$

Results are presented on the spin structure and production mechanism of the ρ^0 meson. A comparison is made of the results of this analysis with those of a higher energy π^- p experiment and the predictions of a π exchange absorption model.

The isospin zero S wave $\pi\pi$ scattering phase shifts are obtained for $\pi\pi$ effective mass less than 1 GeV/c^2. Evidence is presented favouring a set of phase shifts rising slowly through the rho region to be 90° at about 900 MeV/c^2 in $\pi\pi$ effective mass.

An investigation is also made of the branching ratios of the f^o meson into final states other than $\pi^+ \pi^-$. These include

$$\pi^+ d \rightarrow p_s \, p \quad K^+ K^- \tag{4}$$

$$\pi^+ d \rightarrow p_s \, p \quad 2\pi^+ 2\pi^- \tag{5}$$

$$\pi^+ d \rightarrow p_s \, p \quad 2\pi^+ 2\pi^- \pi^o \tag{6}$$

$$\pi^+ d \rightarrow p_s \, p \quad \pi^+ \pi^- \; M M \tag{7}$$

$$\pi^+ d \rightarrow p_s \, p \quad 2\pi^+ 2\pi^- M M \tag{8}$$

where M M indicates missing particles. Evidence is presented for f^o decay into channels (4) and (5) and the decay rates are measured.

Acknowledgements

I should like to thank all members of the Birmingham high energy group for their frequent assistance. In particular, I am indepted to my supervisors, Prof. D.C. Colley and Dr. J.B. Kinson, for a considerable amount of help and advice.

Thanks are also due to Dr. M.F. Votruba at Birmingham and Drs. R.L. Sekulin and J.A. Charlesworth at the Rutherford Laboratory for many discussions and assistance concerning the analysis of this experiment. I am also very grateful to Prof. W.E. Burcham for taking a close interest in my progress.

I thank Dorothy Hastings for her efficient typing of this report.

Finally, I wish to thank my parents for their constant support during my time as a student.

CONTENTS

Page No.

Chapter 4

Cross Section Measurements in $\pi^+ d \rightarrow p p \pi^+ \pi^-$

Chapter 5

Analysis of ρ^o Production

Chapter 6

Branching Ratios of the f^o meson

Appendix 1

Appendix 2

Appendix 3

Introduction

The main purpose of the 4 GeV/c $\pi^+ d$ experiment is to study neutral meson resonances which contain a single neutral decay product and which are unable to be fitted in the charge symmetric $\pi^- p$ interaction owing to the presence of two neutral particles in the final state. Among such resonances are the η^o, the ω^o, the A^o_2 and the ϕ (1670). In addition, several reactions can be studied in both $\pi^- p$ and $\pi^+ d$. Notably, information can be obtained on the $\pi\pi$ interaction, available as a well-constrained 4 - c fit in $\pi^+ d$.

The experiment was planned as a collaboration between the Rutherford Laboratory, and the Universities of Birmingham and Durham, and the first exposure was undertaken in the C.E.R.N. 2m bubble chamber during the summer of 1970. The author has been concerned with the preparation and analysis of the Birmingham share of the data. A second exposure was made in December 1972 and altogether the collaboration has at its disposal 750 ,000 pictures.

So far the collaboration has investigated forward and backward ρ^o, f^o and ω^o production and coherent deuteron production. Subjects of interest in the future include hypercharge exchange reactions and a study of the whole neutral three pion system.

CHAPTER 1

Chamber and Beam

1.1 Exposure Details

This report contains an account of a π^+ d experiment at 4 GeV/c undertaken at C.E.R.N. using the 2 m chamber and U.5 beam.

The 2m chamber was double-pulsed for this experiment with two 20 msec expansions, separated by a gap of 150 msec. Each double-pulse is separated by about two seconds during which the C.E.R.N. accelerator and beam system serve other experiments and the internal accelerator beam is regenerated. Deuterium at a temperature of 31.3 ^{o}K is held in the bubble chamber at a pressure above the saturated vapour pressure of deuterium [Fig.1.1], and, on expansion with a piston, the pressure is reduced below the saturated vapour pressure leaving the deuterium in a superheated state. Charged particles passing through the chamber lose energy through local heating of the liquid at the rate of about 0.25 MeV/cm by ionising the deuterium and so initiating bubble formation. The bubbles marking the tracks are recorded in stereoscopic photographs using an electronic flash. The number of bubbles per cm of track length is regulated by the temperature and pressure inside the chamber and is usually adjusted to be about 14 for a relativistic particle. By varying the relative timing of the beam entry and the photographic flash, it is possible to adjust the bubble size in the chamber. However, the bubble image size obtained on film is essentially independent of this, being the diffraction spot from the real bubble magnified by the optical system to be approximately bubble size.

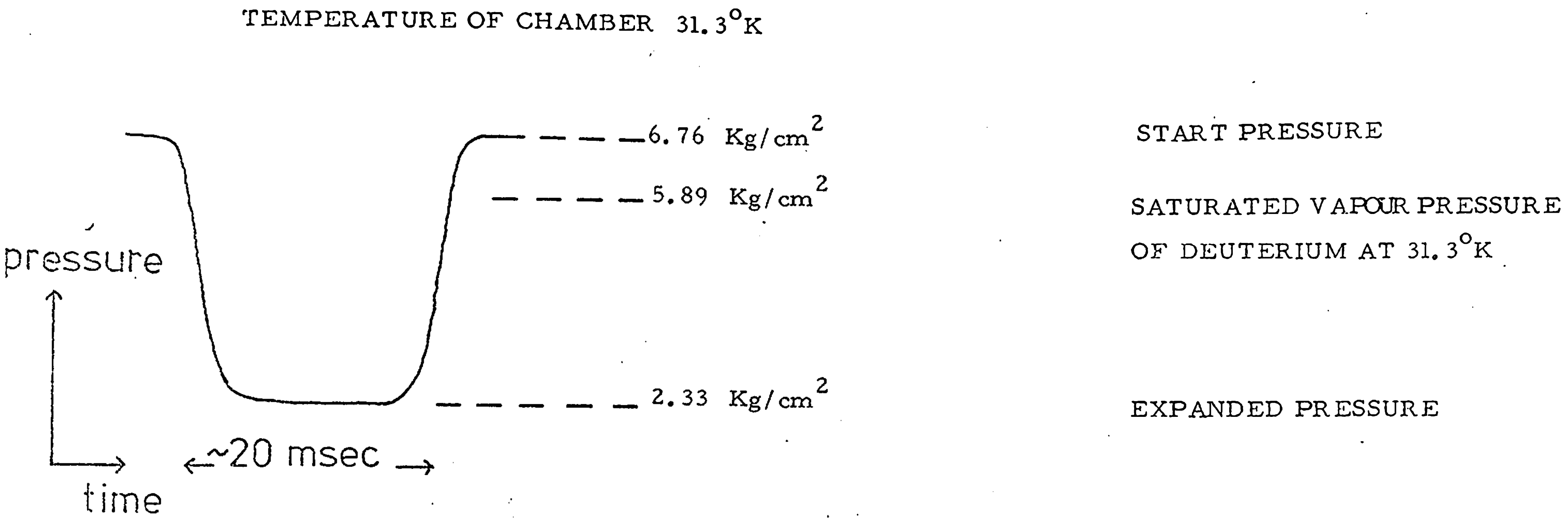

Fig. 1.1 EXPANSION PULSE OF THE 2 m CHAMBER

A schematic diagram of the 2m chamber is given in Fig. 1.2, together with the coordinate system used in this experiment. It should be noticed that this is a left-handed system. On each of the planes are etched fiducial marks which appear on the film and which enable geometric reconstruction to take place giving accurate spatial information about the paths followed by the charged particles. As the positions of the fiducial marks are known beforehand, the effects of camera lens distortion and film stretch may be parameterised in the reconstruction.

The U.5 beam is 181 m long from the external target to the bubble chamber and, when used to separate pions, contains only one Radio Frequency (R.F.) separator of 9 MW power. If the beam consists of the wanted particles plus a major contamination, the phase velocity of the R.F. cavity can be adjusted until there is zero net deviation through the cavity for the unwanted particles while the wanted particles are obtained with a slight sideways deflection. The ability of the R.F. cavity to separate pions from protons is shown in Fig. 1.3 which is a beam profile after the R.F. cavity across the front of the beam stopper. The central peak consists of protons, absorbed by the beam stopper, while the outer wings contain pions. There is almost complete separation between the two groups of particles. A detailed analysis of the beam contamination is given in the next section. The momentum bite of the U.5. beam system, with the conditions used in this experiment, is about 0.25% .

Operating details of the 2m chamber and the U.5. beam are given in two C.E.R.N. handbooks [Ref. 1].

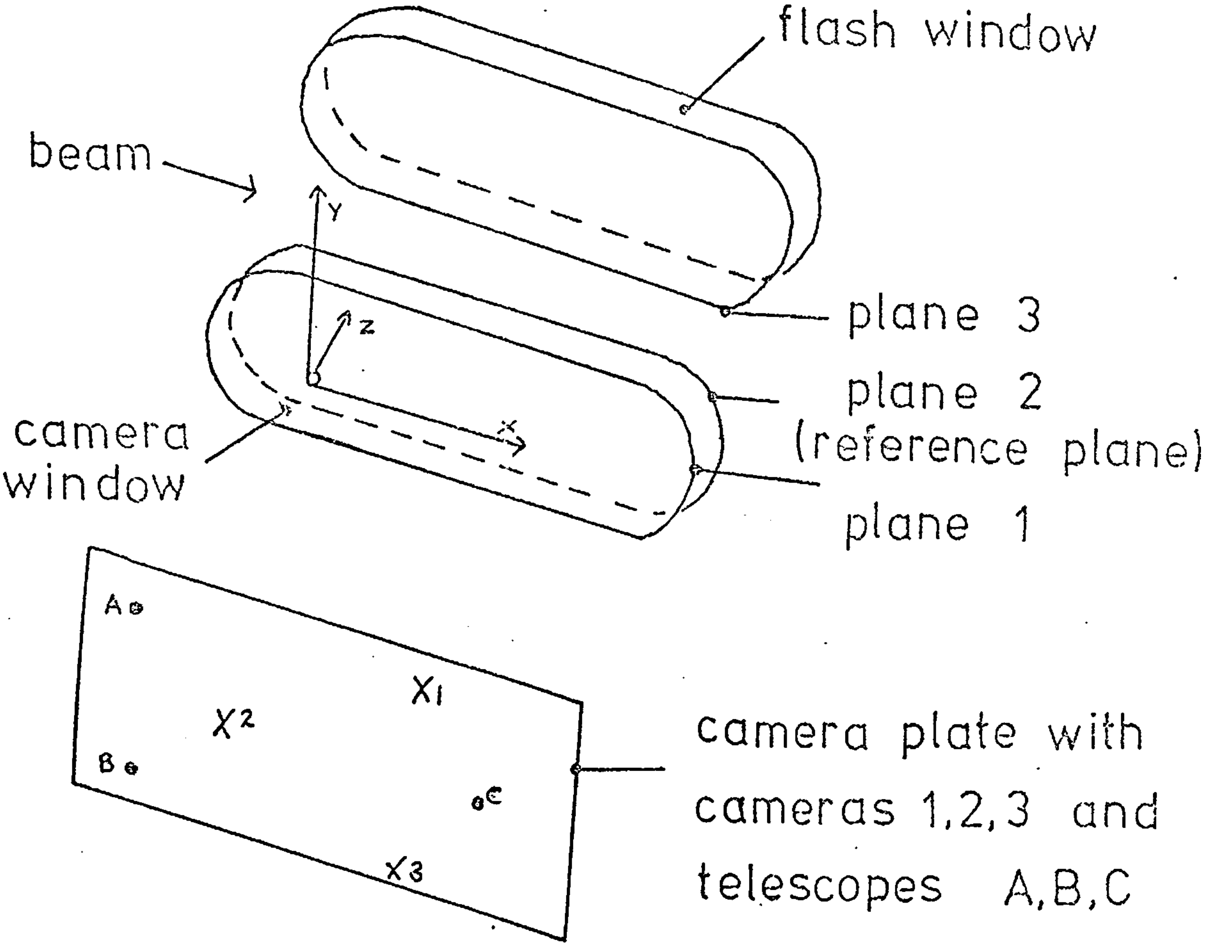

(x, y, z) is a Left-Handed system on Plane 2

x - axis Points along Beam

z - axis is Perpendicular to Plane 2, Points into Chamber

Fig. 1.2 SCHEMATIC DIAGRAM OF 2M CHAMBER

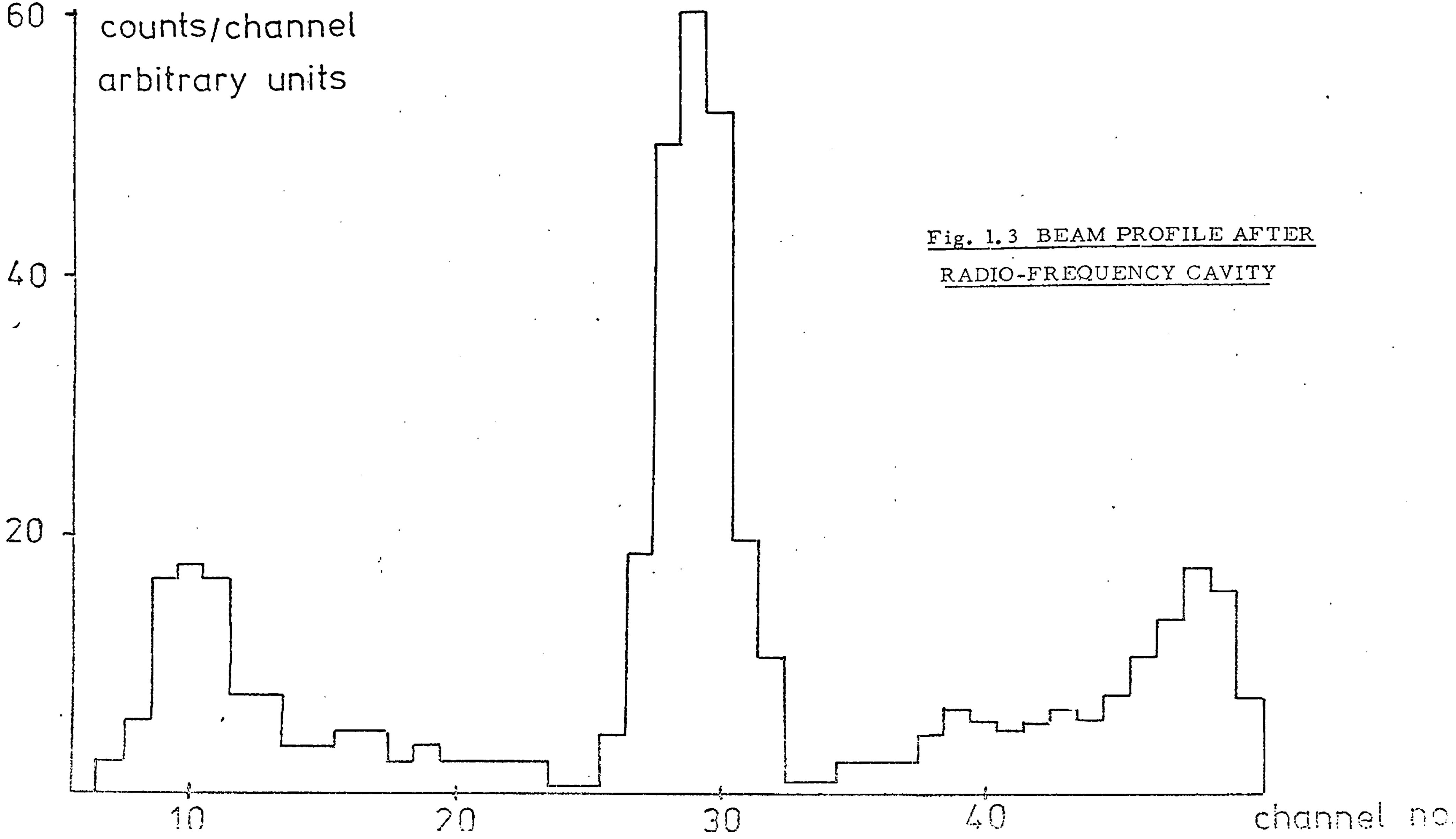

Fig. 1.3 BEAM PROFILE AFTER RADIO-FREQUENCY CAVITY

1.2 Contamination of the Beam.

Any contamination of the π^+ beam must be made up of the three charged particles p, K^+, μ^+. The muon contamination is particularly difficult to estimate. However, several methods may be employed to estimate the various contaminations present.

K^+ Contamination.

To estimate the K^+ contamination 3018 3 - prong events from six rolls of film were tried in the kinematics program for fits to the decay $K^+ \longrightarrow \pi^+ \pi^+ \pi^-$. No fits were obtained. The 3π mass spectrum, using measured quantities for the tracks, was plotted and no peak was observed at the K^+ mass. All events, except one, in this region had missing quantities inconsistent with zero. This one allows us to estimate an order of magnitude for the K^+ contamination.

The total path-length of the beam on the 6 rolls was 1.96×10^7 cm which, from the expression

$$L = \frac{N_\tau}{\psi} \frac{c\,\tau\,p}{m}$$

(where τ, p and m are the kaon lifetime, momentum and mass, L is the path-length and ψ is the $K^+ \rightarrow \pi^+ \pi^+ \pi^-$ branching fraction), requires about 365 3π decays if all the beam were pure kaon. The one event therefore corresponds to a beam contamination of 0.5% (after a correction of 4512/3018 for the total number of events seen on the film compared to the number actually measured). This implies that the K^+ contamination is negligible.

Proton Contamination.

An indication of the proton contamination came from measuring two rolls of 4 GeV/c proton film. The calculation partly follows the method of Gordon [Ref. 2], and involves three assumptions, the last two of which may be verified in various ways:-

1. the beam in the proton film is pure proton.
2. the probability for a proton induced event to "best fit" (i.e. to have a greater kinematic probability for) a pion beam hypothesis is approximately twice the probability of a pion induced event "best fitting" a proton beam hypothesis. (Verified by studying FAKE events). This assumption, while correct kinematically, is not exactly correct at the final Data Summary Tape stage owing to ionisation information. For each event there is, in general, one slow proton besides the spectator which is usually identifiable by ionisation. This means that the proton contamination found by this method is a slight over-estimate.
3. $$\sigma\,(\pi^+ d \longrightarrow pp\,\pi^+\pi^-) : \sigma\,(pd \rightarrow ppp\,\pi^-) = \sigma_{TOT}\,(\pi^+ d) : \sigma_{TOT}\,(pd)$$

(Verified by interpolating between the data points of Ref. 3)

The "best fits", as shown in Table 1.1, were obtained for the proton beam film and for a subsample of the pion film. The final result has been found to be insensitive to any cuts of spectator momentum or kinematic probability. Ionisation probability also does not help much as an event which is kinematically ambiguous is usually ambiguous by

Table 1.1

Best Fit.	"Pi Film".	"Proton Film".
$\pi^+ d \to p_s\, p\, \pi^+ \pi^-$	4550	14
$p\, d \to p_s\, p\, p\, \pi^-$	910	49

ionisation estimate also.

From the pion and proton beam film, the number of times an event "best fits" the opposite 4 - c hypothesis can be obtained, giving a "chance fit" parameter from the proton film which can be applied to the pion film. Any excess fitting of the proton beam hypothesis in the pion film gives the proton contamination. Such a method gives a proton contamination in this case of 6 ± 3%.

A more accurate method of determining the proton contamination is to make a special scan for δ-rays on several rolls of film. The maximum momentum of a δ-ray depends on the momentum and mass of the particle interacting with the electron. Protons at 4 GeV/c produce δ-rays with a maximum momentum of about 20 MeV/c whereas light particles (pions and muons) produce δ-rays with a maximum momentum of about 750 MeV/c. By counting the number of δ-rays between two limits above 20 MeV/c and comparing the number so obtained with the theoretical cross section [Ref.4], the number of light particles in the beam may be found. The theoretical cross section between two momentum limits is given by

$$\sigma(p_1 \rightarrow p_2) = \frac{25.5 \times 10^{-26}}{T_{max}} \left[\left(\frac{T_{max}}{p_1} - \frac{T_{max}}{p_2} \right) - \ln \left(\frac{p_2}{p_1} \right) \right]$$

where σ is in barns and the other quantities are in MeV. T max is the maximum possible kinetic energy of a δ - ray for this particular beam.

Five quarter rolls of film were scanned for δ-rays in seven equal momentum intervals between 21 and 167 MeV/c. The number of δ - rays found in each interval is shown in Table 1.2. A beam count was made also and the number found in each interval compared with the theoretical cross section. The resulting distribution is shown in Fig. 1.4 after a correction for a scanning efficiency of 91% found from check-scanning one quarter roll. Fig. 1.4 shows the observed distribution to be in good agreement with prediction. Although it is the total cross section between 21 and 167 MeV/c which is important in this calculation, the fact that the momentum distribution is in broad agreement with the theoretical prediction is a confirmation of our analysis.

Then, fraction of light particles in the beam =

$$\frac{\text{Experimental total cross section in the 7 intervals}}{\text{Theoretical} \quad .. \quad .. \quad .. \quad ..}$$

$$= \frac{0.995 \ \pm \ 0.07 \text{ mb}}{0.9932 \qquad \text{mb}} \quad = \ 1.00 \pm 0.07$$

corresponding to a proton contamination of 0 ± 7%.

A more qualitative method can also be used to observe any proton contamination. By replacing the pion beam with a proton, we replace the π^+ with a proton in the final state giving the possibility of N^* resonances in the resulting proton-pion mass plots. No such effects have been seen. From these several methods it can be stated that the proton and kaon contaminations are consistent with zero.

Muon Contamination.

We can approximately estimate the muon contamination from the total $\pi^+ d$ cross section and our δ- ray count of the number of

Table 1.2 Momentum Distribution of δ - Rays.

Seven equal momentum intervals between 21 and 167 MeV/c.

Interval	No. of δ - Rays
1	788
2	273
3	117
4	62
5	31
6	30
7	17

Total Beam Track count	=	42900
Total No. of beam tracks with δ - rays	=	1318
Total No. of beam tracks with δ - rays and a subsequent interaction	=	92

Efficiency of a single scan for δ rays	=	91 ± 5%
Efficiency of a single scan for δ rays with the beam track subsequently interacting	=	85 ± 20%

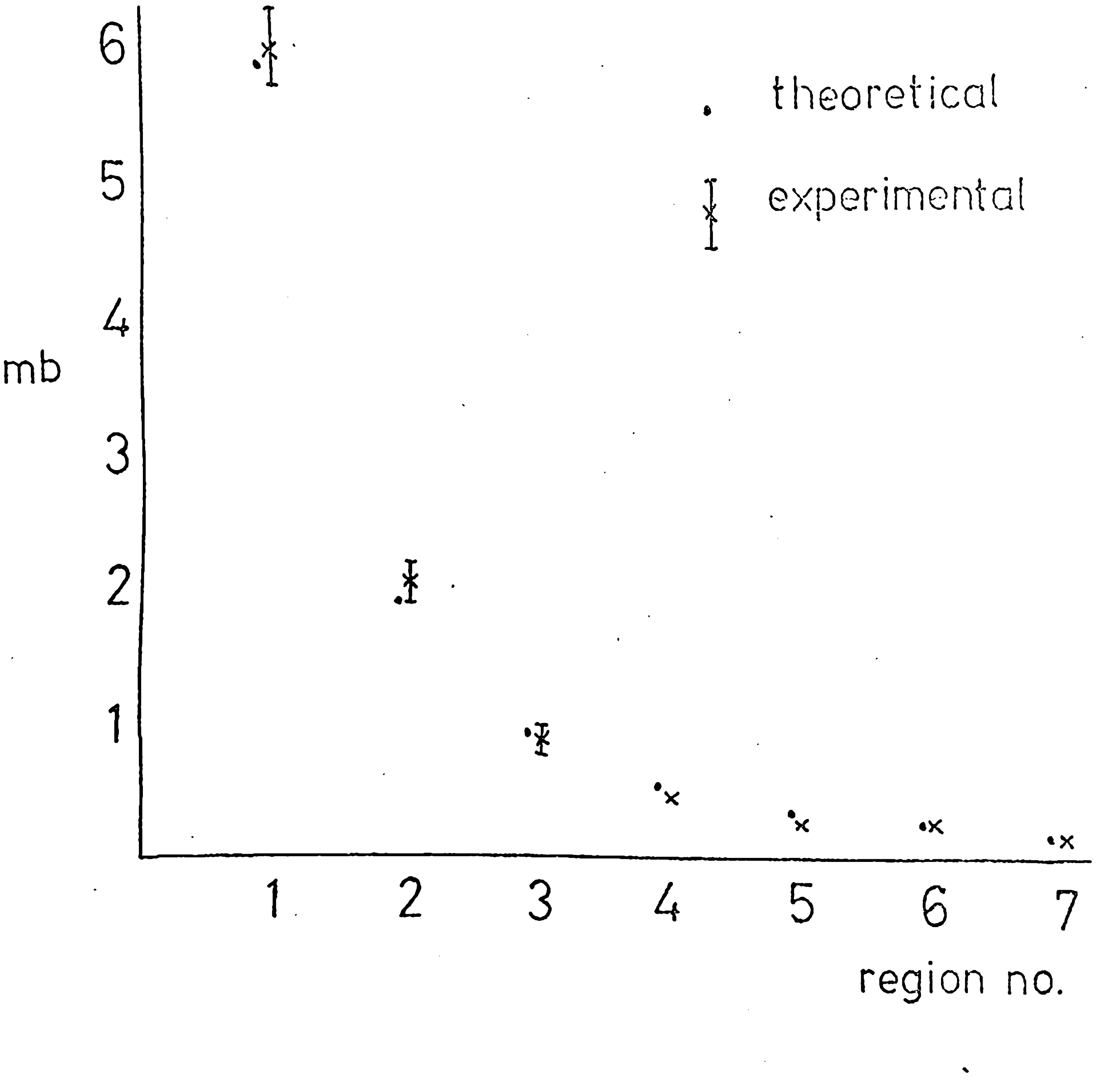

Fig. 1.4. δ-Ray Momentum Distribution

interacting beam tracks which also give a δ-ray between 20 and 167 MeV/c.

$$\text{Fraction of pions in beam} = \frac{\text{No. interacting beam tracks with fast } \delta\text{-rays}}{\text{No. expected (from the total } \pi^{+}d \text{ cross section of 57 mb)}} = 85 \pm 25\%$$

which corresponds to a muon contamination of 15 ± 25%.

An improvement can be made on this muon contamination estimate by considering the geometry of the C.E.R.N. U.5. beam [Ref. 1].

Pions decaying at 4 GeV/c in the 181 m of beam line produce muons with an approximately flat momentum distribution between 2.3 and 4 GeV/c. Only 44% of the 4 GeV/c pions separated at the start of the system will survive to reach the bubble chamber. Of the muons that are not swept out of the system previously, the vast majority are removed by the M5 - M6 - C9 combination forming a 1% momentum acceptance. Therefore, most of the muons in the beam at the bubble chamber are from decays in the last 8.7 m from C9 to the chamber. This corresponds to a muon contamination of about 6%.

1.3. Determination of the Beam Momentum.

As the $\pi^{+}d$ experiment is intended to be a high resolution experiment, it is essential that the beam characteristics be known as well as possible. Various checks which have been made on the beam momentum are outlined below.

During the exposure at C.E.R.N. the beam momentum at the final collimator was estimated to be 4.050 GeV/c. This figure was taken in our initial tests as the value of the beam momentum in the chamber. However, there is naturally a loss of momentum between the final collimator and the fiducial region in the chamber itself (whose entry point is defined in the 2 m coordinate system to be at $x = -15$ cm). This loss of momentum can be calculated from the known amount of metal, plastic scintillator and air between the final collimator and the fiducial region and is about 15 MeV/c, giving a beam momentum in the chamber of 4.035 GeV/c.

The magnetic field in the chamber, to which the measured momentum is directly proportional for a given radius of curvature, was checked by plotting the effective mass of the two pions which constitute the decay $K^o_s \rightarrow \pi^+ \pi^-$, and by seeing whether the resulting distribution was peaked at the accepted K^o mass. 318 K^o_s decays from the first rolls measured in the experiment gave an average effective mass-squared of

$$0.2477 \pm 0.0003\ (\text{GeV}/c^2)^2$$

compared to the present world average [Ref. 3] of

$$0.2478 \pm 0.00015\ (\text{GeV}/c^2)^2.$$

Other possible systematic sources of error in geometric reconstruction, such as spatial distortion in the chamber, liquid motion, etc., have been checked out as far as possible. Unfortunately, two rolls of so-called zero field film taken during the exposure, which would have been very useful in distortion studies, were found to be un-usable, owing to a residual field of about 0.3 Kg remaining in the chamber. This was found by determining the range and radius of curvature of several hundred slow δ -rays.

The simplest method of determining the beam momentum is to measure a series of beam tracks and to use the Geometry Program to fit them to a mass-dependent helix. The resulting momentum at the point x = - 15 cm can be obtained using the Range-Momentum Table in the program. Accordingly, 2679 beam tracks were processed in this way and the resulting distribution was found to peak at 4.04 GeV/c with a width, owing to measurement error, of 150 MeV/c. Taking 764 of these beam tracks with a track length greater than 60 cm, for which the measurement error is slightly better, gave a distribution peaked at 4.035 GeV/c. However, with such a large measurement error spread and with several possible systematic errors inherent in this method, these distributions can only be considered as a guide to the beam momentum.

A second, more accurate method is to consider the well constrained reaction

$$\pi^+ d \longrightarrow pp\pi^+\pi^-$$

One can obtain the real beam momentum by inserting a nominal momentum into the kinematics program and by looking at the resulting fits to this reaction. The "Missing Px" for this reaction (defined as the difference between the momentum of the beam and the sum of the measured momenta of the outgoing tracks in the x direction) is the amount by which the beam is incorrect. This method should be more exact than the measured momentum method as, in this case, information from the whole of the well-constrained event is considered and any systematic errors in track measurement should be reduced. The "Missing Px" for a large part of our initial data, using the nominal value of 4.050 GeV/c, was found to peak 15 MeV/c above zero, indicating that the nominal value was too high by this amount.

A guide to this discrepancy had already been obtained from a small number of events by considering the momentum "Stretch Function" defined as

$$S\left(\frac{1}{p}\right) = \frac{\left(\frac{1}{P\,\mathrm{fit}}\right) - \left(\frac{1}{P\,\mathrm{nominal}}\right)}{\sqrt{\left(\Delta\frac{1}{P\,\mathrm{nominal}}\right)^2 - \left(\Delta\frac{1}{P\,\mathrm{fit}}\right)^2}}$$

which should, on average, be zero, if the nominal beam momentum value is correct. In addition, if the errors on track measurement are calculated correctly the Stretch Function distribution should have an approximately normal distribution shape with a standard error of 1.0. The variable '1/p' is used as its errors are more normally distributed than 'p' owing to the fact that measurements are made of sagitta rather than radius. By varying the nominal beam momentum, one can observe the variation of the Stretch Function mean value, as shown in Fig. 1.5 for 305 events of early data. It is clear, even from these few events, that the beam momentum should be much lower than 4.050 GeV/c.

The spread in the Stretch Function distribution, together with the distribution of the kinematic probabilities for these fits enable us to

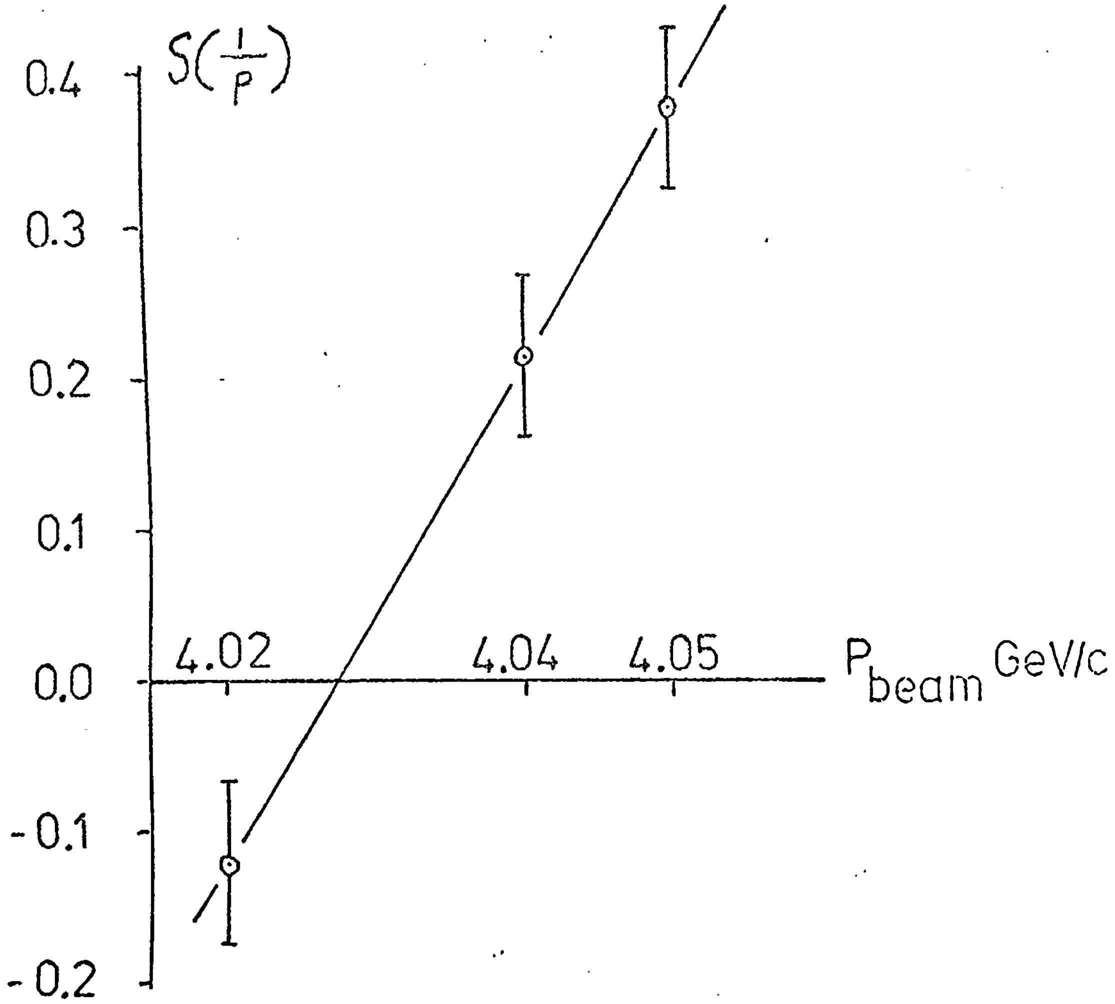

Data 305 4 prong 4 - c events of reaction

$\pi^+ d \longrightarrow p\, p\, \pi^+ \pi^-$

Fig. 1.5 VARIATION OF $S(\frac{1}{P})$ FOR 305 EVENTS OF EARLY DATA estimate the effective uncertainty in the beam momentum. A flat distribution of the kinematic probabilities is obtained only when both the error on beam measurement and the error on the secondary tracks are estimated correctly. By adjusting both these quantities for a large sample of the data an essentially flat distribution of the kinematic probabilities was obtained together with a standard error of the Stretch Function distribution of about 1.0 when the effective uncertainty on the beam was ± 15 MeV/c.

Similar values of the beam momenta were arrived at independently by the Rutherford Laboratory and consequently the whole data were processed using a beam momentum of 4.035 ± 0.015 GeV/c.

CHAPTER 2

Present Technical Status of the Experiment

2.1. General.

Birmingham received over one third of the film from the first exposure, amounting to approximately 130 thousand pictures or 171 segments (quarter rolls). The scanning and measuring were undertaken in two parts. In the first 25% of our film (Part 1), operators were instructed to measure essentially all events, except for one or two prong scatters. In the remaining three-quarters (Part 2), however, the operators measured only those events corresponding to an interaction on the neutron of the deuteron; in other words, only odd prong events or even prongs with a stopped spectator proton with a projected track length less than 20 cm. on all three views. In addition, they continued to measure events containing a neutral strange particle decay (vee), irrespective of whether these events were proton or neutron interactions.

Occasionally an event is found to be unmeasurable. A large number of events fall into this category because of a secondary interaction of one of the outgoing tracks, making the track too short for measurement. However, the largest number of unmeasurable events, at the first measurement stage, are those with another beam track being very close to the event vertex, making event identification by the H. P. D. (Hough Powell Device, a Flying Spot Digitiser) very difficult. Most of this second category though can be obtained at the remeasurement stage.

Even so, any loss of events into this category should not bias the data in any way. Events considered unmeasurable at this first measurement stage are designated 'Recorded Only'.

Scanning and measuring of Birmingham film were completed in October 1971 and yielded the following number of events:-

	Measured Events	Recorded Events	Total
Part 1	23501	6712	30213
Part 2	45477	13039	58516
Total	68978	19751	88729

The "Recorded Only" number for Part 2 includes 4300 events containing a charged strange particle decay (kink) which were not measured in this part of the film.

In addition, for contamination estimate purposes, two segments of 4 GeV/c film taken with a proton rather than a pion beam were measured. With the data from Durham and the Rutherford Laboratory, the first exposure contains about 180 thousand measured events, the last event being measured in late 1972.

Only about 81% of measured events reach the final D.S.T. (Data Summary Tape), mostly owing to Geometry track failure and (for Part 1 events) rejection by physicist at the final selection stage. All of the failed events from Part 1 were attempted for re-measurement by Conventional measuring machines, yielding another 3,500 events for the

D.S.T. At the present time, a number of the failed events from Part 2 have been re-measured, most of the vee events having been completed.

Measurement of the second exposure of this experiment began in June 1973. However, data from this exposure is not contained in this report.

2.2. The π^+d Processing System [Fig. 2.1].

The π^+d 4 GeV/c experiment was the first experiment at Birmingham to be processed by an almost completely automatic system. After two view pre-measurement by operators on SHIVA digitising tables, the third view was reconstructed by computer. Computer reconstruction of the third view speeds up the measurement rate considerably. The film was then measured by the H.P.D. which provides accurate track position and ionisation information after the HAZE pattern - recognition program [Ref. 5]. The pre-measurement on the SHIVA tables is necessary so as to provide guidelines (or "roads") either side of each track within which the computer controlled H.P.D. records all bubble positions. Pattern recognition is used in HAZE to sort all the information within the roads and, by using an averaging technique, provides accurate coordinate measurements (Master Points) along the length of each track.

The Rutherford Laboratory chain of Geometry and Kinematics programs was used [Ref. 6] with various Birmingham modifications. Events, which failed Geometry at the first pass were manually aided using

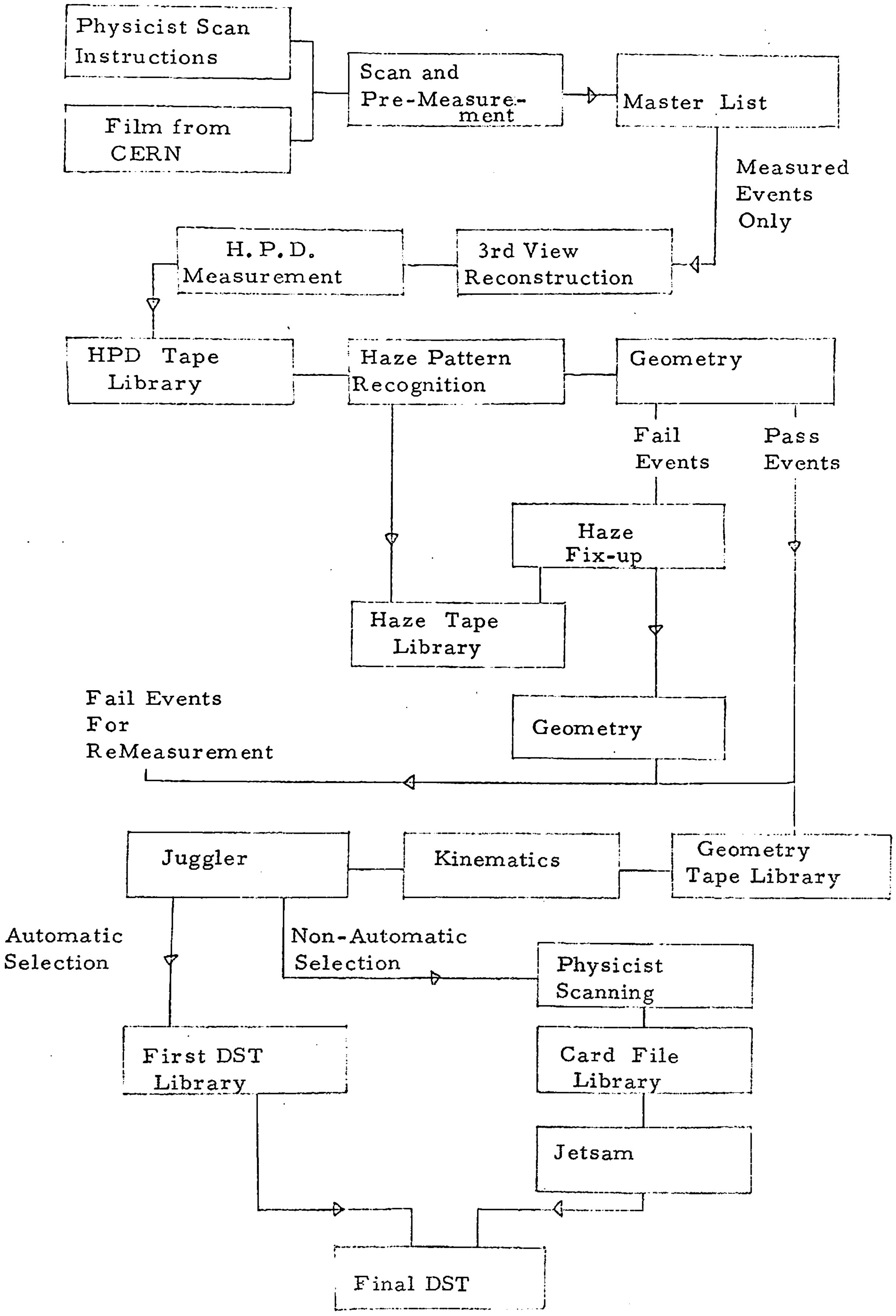

Fig. 2.1 The π^+d Processing System.

the C.R.T. HAZE-FIXUP program. Here an operator is able to correct any misplaced Master Points on a track and to pass the corrected track back to the Geometry program. Any events which still fail are tried for re-measurement by Conventional machines at a later date. Conventional machines are manually operated and, although slightly less accurate than an H.P.D., require no pre-measurement.

The author was responsible for an improved Geometry program (three-dimensional track reconstruction program), Kinematics program (hypothesis testing program for track-mass combinations), and a third program, JUGGLER, which uses the ionisation information from the H.P.D. to choose between the competing hypotheses which are kinematically possible. JUGGLER was capable of making a decision which could not be improved by a physicist on approximately 70% of events; the remainder (for Part 1) were looked at by physicists and their decisions were passed to the D.S.T.by the JETSAM C.R.T. program.

With an efficient system the end result is a D.S.T. containing information on all measured events in a form suitable for the physicist to use for his analysis. Development of the Birmingham processing system is still continuing.

2.3. The JUGGLER Automatic Selection Program.

The final part of the 4 GeV/c processing chain is the JUGGLER program developed by the author. This is taken from the R.H.E.L.

JUDGEION program developed independently at Birmingham by various people, notably S. W. O'Neale [Ref. 7]. The program computes an ionisation chi-square and confidence level for each view from the predicted ionisation (obtained from the momentum and mass of the track) and the measured ionisation (obtained from H. P. D. measurements) [Ref. 7]. This is done for each fit (mass combination) which is possible after kinematics.

Fits considered for ionisation (for a simple four-prong event, for example) would be:-

(a) All good kinematic fits i. e. fits which have not failed in the Kinematics program and which have a non-zero kinematic probability.

(b) All failed 1 - c fits (i. e. failed fits which hypothesised a missing neutral particle) whose missing mass-squared satisfy the criteria:-

$$MM^2 + 3\,\Delta\,MM^2 \geqslant (\text{Mass } \pi^o + \text{Mass Neutral})^2$$

Such fits can possibly have missing at least one π^o together with the hypothesised missing neutral particle. Such fits are called "Missing Mass Fits" or "Multi-Neutral Fits".

(c) All failed 4 - c fits (i. e. fits with no missing neutral) which have failed in Kinematics for some reason but which have missing mass and momenta consistent with zero. These events could in fact be the corresponding 1 - c fit with the π^o at rest, although in general this is unlikely.

For each fit we have an ionisation probability (confidence level) for each of the three views. Anti-selection now takes place with each fit being compared with all the others in turn. No fit is discarded on the basis of its own ionisation probability alone, but only if there exists another fit with far superior values. A given fit is rejected if there is another fit such that :-

<u>either</u> the ionisation probability of the second is greater than $2\frac{1}{2}$ times the ionisation probability of the first on all three views.

<u>or</u> the ionisation probability of the second is greater than 5 times the ionisation probability of the first on 2 views, and that the ionisation probability of the first is NOT 5 times the ionisation probability of the second on the final view.

This procedure does not stop a decision being made if there are only two views with good ionisation measurements. Occasionally the ionisation information on a view cannot be used or is not available or is incorrect (through overlapping tracks, for example). Then a two-view decision must be taken. To avoid a fit with low ionisation probabilities discarding another with even lower probabilities, all ionisation probabilities below a cut-off of 0.2% are raised to that cut-off before any comparisons are made.

As a test, 40 segments of Part 1 data were partially scanned for program errors and 8 segments were fully scanned, paying particular attention to events involving vees and those events where the ionisation program had difficulty in making a decision. The test showed that 3% of events were classified by the program wrongly; this figure was about 2% for unique events (i. e. events containing only one final ionisation choice) and increased as the ambiguity of the decision process increased.

Events containing a correct 4 - c or 1 - c fit almost never had the fit wrongly classified. The test showed that multi-neutral fits were largely responsible for these few classified incorrectly. However, no incorrect 4-c or 1 - c fit can be added in this way and the resulting data-set for these categories was found to be correct, although slightly reduced, with a corresponding slight increase in background to the multi-neutral channels.

About 20% of events contained additional fits which should, in principle, be excluded by the ionisation information but which are still ambiguous with the present technique. Most of these are multi-neutral fits. However, for these fits there is usually an important difference in the track-mass combinations, such as pion-proton inversion, enabling a physicist's decision to be made instead of a program decision. This is a consequence of the H. P. D. and the programming chain not being as yet as good an ionisation measuring device as one would like.

In practice, however, this 20% of events with additional fits do not constitute a serious problem. The vast majority are 1 - c fits with an additional incorrect multi-neutral combination and these can be classified at the D. S. T. by imposing a kinematic probability cut on the data. The remainder are composed of multiple ambiguities of multi-neutral fits whose physics usefulness is not seriously reduced by a small increase in ambiguity. It was evident that for the majority of our future analyses we could continue with this form of the program. The ionisation selection was seen to be almost as capable as physicists selection in producing data-sets for 4 - c and 1 - c fits for physics analysis once the behaviour of fit selection had been understood.

Our conclusion after this test was that the program was capable of reducing physicist scanning to about the 20% described above, and Part1 was processed accordingly. The remainder of the film was processed completely automatically (except for events with vees) using the results of the test to obtain data-sets for the common channels.

CHAPTER 3

The Channel $\pi^+ d \rightarrow p p \pi^+ \pi^-$

3.1. Event Selection

The most common 4 - constraint channel in this experiment, accounting for over 10% of the total data, is the reaction

$$\pi^+ d \rightarrow p p \pi^+ \pi^- \qquad (1)$$

Correct selection of this channel is facilitated by its being virtually unambiguous both kinematically and by ionisation density.

A total of 18780 events were obtained in the original data-set with a kinematic fit to reaction (1). Because a pion-proton kinematic ambiguity is occasionally possible, a few events contained more than one kinematic fit, giving a total of 19753 fits to reaction (1) in the original data-set. This number was reduced to the 16981 fits suitable for analysis by means of the following cuts on the data:-

(a) Removal of fits rejected by the ionisation program [303 fits removed]

(b) Removal of fits when the event contained a different 4 - constraint fit with a higher kinematic probability [1088 extra fits removed].

(c) Removal of fits with kinematic probability

$$P_{\chi^2} < 0.005$$

[676 extra fits removed]

(d) Removal of fits with Missing Mass Squared outside the range.

$$-0.03 < MM^2 < 0.008 \quad (GeV/c^2)^2$$

[705 extra fits removed]

A fit rejected by one of these cuts was usually rejected by at least one other also.

The 583 fits in the remaining 16981 which contained a spectator proton with momentum greater than 300 MeV/c were also removed, leaving 16398 events available for the study of $\pi\pi$ scattering.* As these 583 fits are far more than are expected from knowledge of the deuteron wave function, they are probably the result of some sort of double scattering rather than the "free nucleon" interactions in which we are interested. We are certain that these cuts do not bias the physics analysis in any way.

In Figs. 3.1 to 3.4 we show the general kinematic properties of fits to reaction(1) . There is no qualitative change of these properties in going from the original data-set to the reduced data-set. However, we feel that these cuts on the data are necessary in order to ensure a clean sample of events for analysis.

Figs. 3.1(a) and (b) and (c) show the Missing Px, Py and Pz distributions for seen proton spectators only. Figs. 3.2 (a), (b) and (c) show the same quantities for unseen spectators. From these distributions the spread due to measurement errors may be seen; the large spread in Δ Px is owing to all the fast tracks being in that direction, and the spread in ΔPz is greater than that in ΔPy owing to the small stereoscopic angle between the three cameras rendering geometric reconstruction more difficult in the z direction.

---

* The analysis described in Chapter 5 was based on a slightly reduced data set of 15485 events.

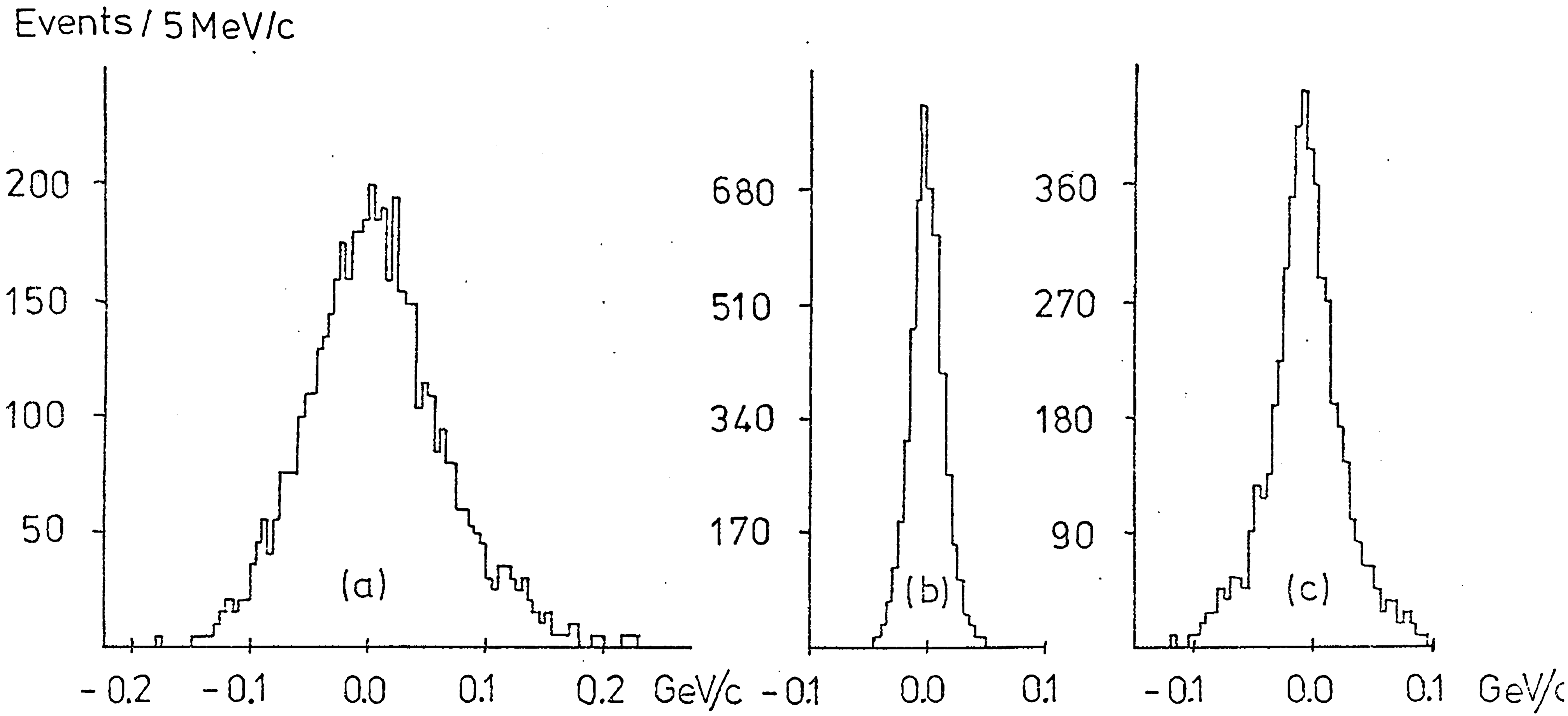

Fig. 3.1. Distributions of Missing Momenta for Seen Spectators

(a) ΔP_x (b) ΔP_y (c) ΔP_z

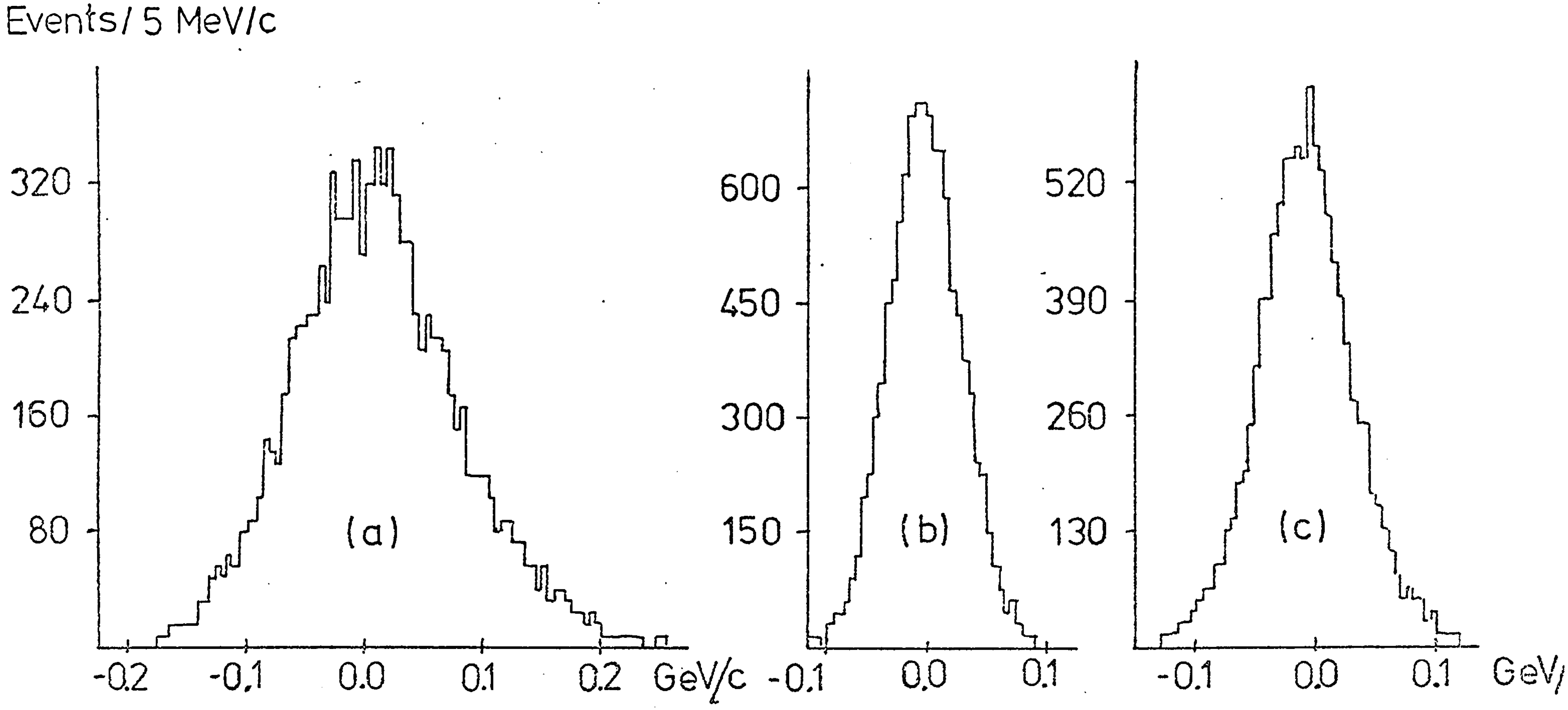

Fig. 3.2 Distributions of Missing Momenta for Unseen Spectators

(a) Δ P x (b) Δ P y (c) Δ Pz

The kinematic probability distribution is shown in Figs 3.3 (a) and (b) for seen and unseen spectators respectively. The errors involved in the kinematic fit are seen to be approximately correct from the flat behaviour of the distribution. The small peak at low probability, which is observed in most bubble chamber experiments, results, among other things, from occasional slight multiple scattering of the outgoing tracks which cannot be parameterised by the usual standard error on track measurement. They are, however, good events and should be included in the data-set. In the case of one-constraint fits (fits with one missing neutral particle) the low probability tail is usually larger and includes a number of wrongly classified fits.

In Figs. 3.4 (a) and (b) are shown the resulting Missing Mass Squared distributions for seen and unseen spectators respectively. It can be seen that all the distributions of missing quantities are more narrowly peaked towards zero for seen spectators than for unseen spectators, as should be expected if there is no knowledge of the momentum and direction of the spectator proton. The assumption made in the Kinematics program for the 3 - momentum of an unseen spectator is that the particle has the three components of momentum equal to zero with "measurement errors".

$$\varepsilon_x = \varepsilon_y = \pm 30 \text{ MeV/c} \qquad \varepsilon_z = \pm 40 \text{ MeV/c}$$

The error in the z direction is larger as it is easier to miss a spectator along the z direction because of their dipping towards or away from the cameras. The size of the errors is chosen such that the vector sum is about 60 MeV/c, the limit of visibility for a slow proton in a bubble chamber.

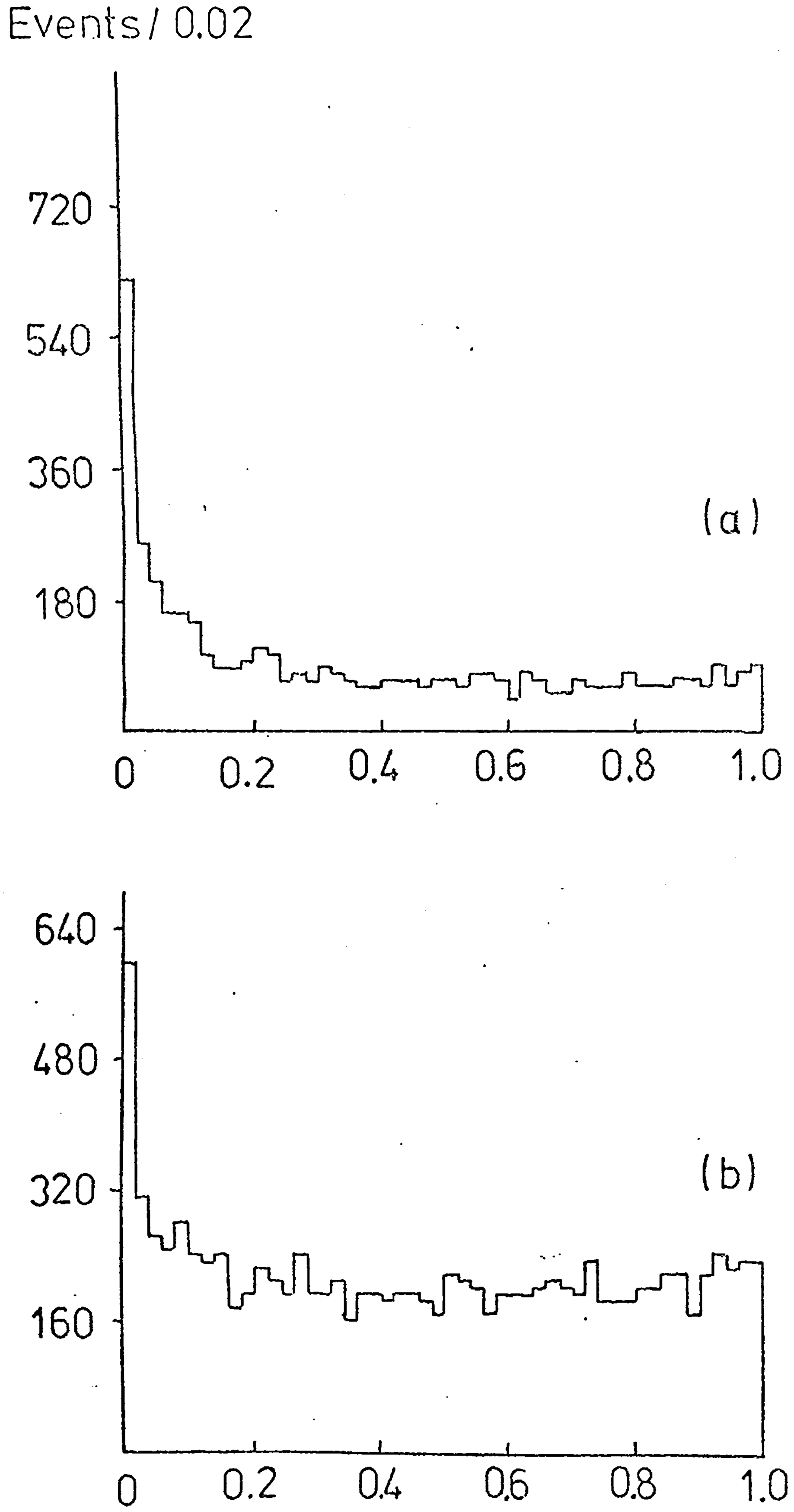

Fig. 3. 3. Kinematic Probability Distribution

(a) Seen spectator events

(b) Unseen spectator events

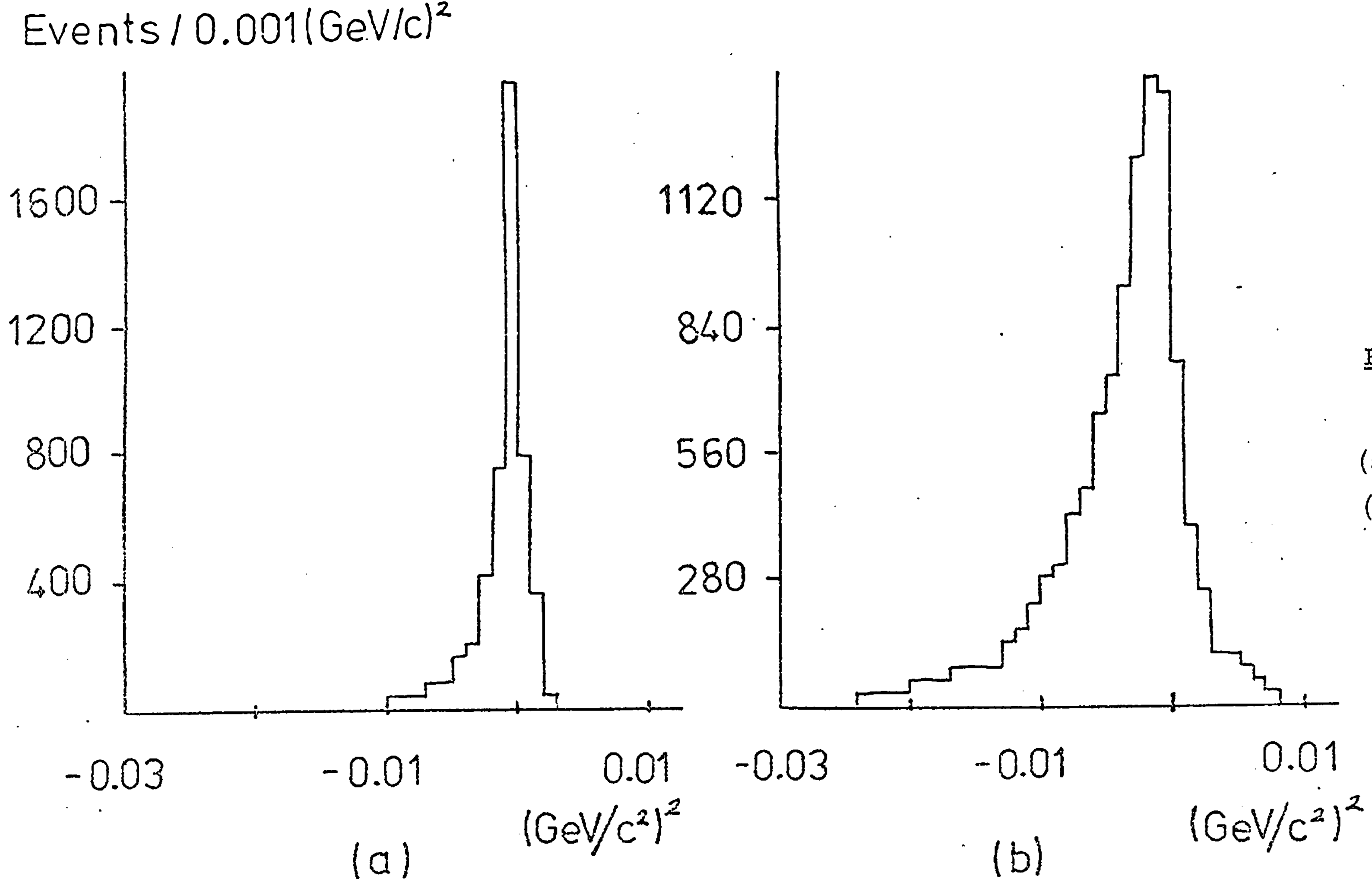

Fig. 3.4. Missing Mass Distributions

(a) Seen spectator events

(b) Unseen spectator events

The distributions of Missing Momenta and Missing Mass Squared are seen to be reasonably central about zero, consistent with the correct choice of beam momentum. There is a slight assymmetry in the Missing Pz distribution which has been ascribed to a possible chamber distortion effect and which is responsible for the anisotropic unseen spectator angular distributions described in the next section.

3.2. Spectator Distributions

In the majority of this experiment, events were selected for measuring by favouring those in which the neutron was involved in the strong interaction, and in which the proton was merely a spectator particle. In this Spectator Model (or Impulse Approximation) we assume the spectator proton to emerge from the interaction with the same momentum and direction it possessed within the deuteron. The basis for this approximation is that the binding energy between the neutron and proton within the deuteron is very small (2.23 MeV), and the extent to which this approximation is valid governs the extent we can study strong interaction pion-neutron collisions in deuterium. Formally the Impulse Approximation has three requirements:-

1) the radius of interaction of the incident particle is small compared to the nucleon-nucleon separation

$$\lambda_{\text{inc}} < \langle r \rangle_{\text{deuteron}}$$

2) the deuteron binding forces are negligible during the time of interaction and only serve to define the momentum of the target and hence of the bystander nucleon, since the two are equal and opposite in the Impulse Approximation.

3) scattering of secondary particles on the spectator nucleon may be neglected.

There are several wave function descriptions of the deuteron, among them the Hulthen wave function [Ref. 8.] The momentum distribution of the spectator proton is obtained from the Fourier Transform of the radial Hulthen wave function and is given by:-

$$p^2 \phi^2(p) = C\, p^2 \left[1/(p^2 + \alpha^2) - 1/(p^2 + \beta^2) \right]^2$$

where $\int \phi^2(p)\, p^2\, dp = 1$

α = 45.5 MeV = $(4.33 \text{ fermi})^{-1} = \sqrt{2 \mu B}$

μ = deuteron reduced mass = $M_n/2$

B = deuteron binding energy = 2.23 MeV

$\beta = j\,\alpha$

where j is a constant between 5 and 7. [Ref. 8.].

We define the spectator proton in this channel to be the slower of the two protons. Fig. 3.5 shows the experimental spectator proton momentum distribution for Part 1 of the data (when all four prong events were measured) together with the Hulthen prediction for j = 5.18 [Ref. 9.]. The curve has been normalised to the total number of events on the plot. The value of j slightly alters the shape of the distribution. We obtain good agreement up to 300 MeV/c with j = 5.18.

The good agreement between the Hulthen momentum distribution and experiment is not maintained at higher spectator momentum. We observe about 11% of spectators with momentum greater than 300 MeV/c compared to the Hulthen prediction of about 2%. Part 2 has only 4% of

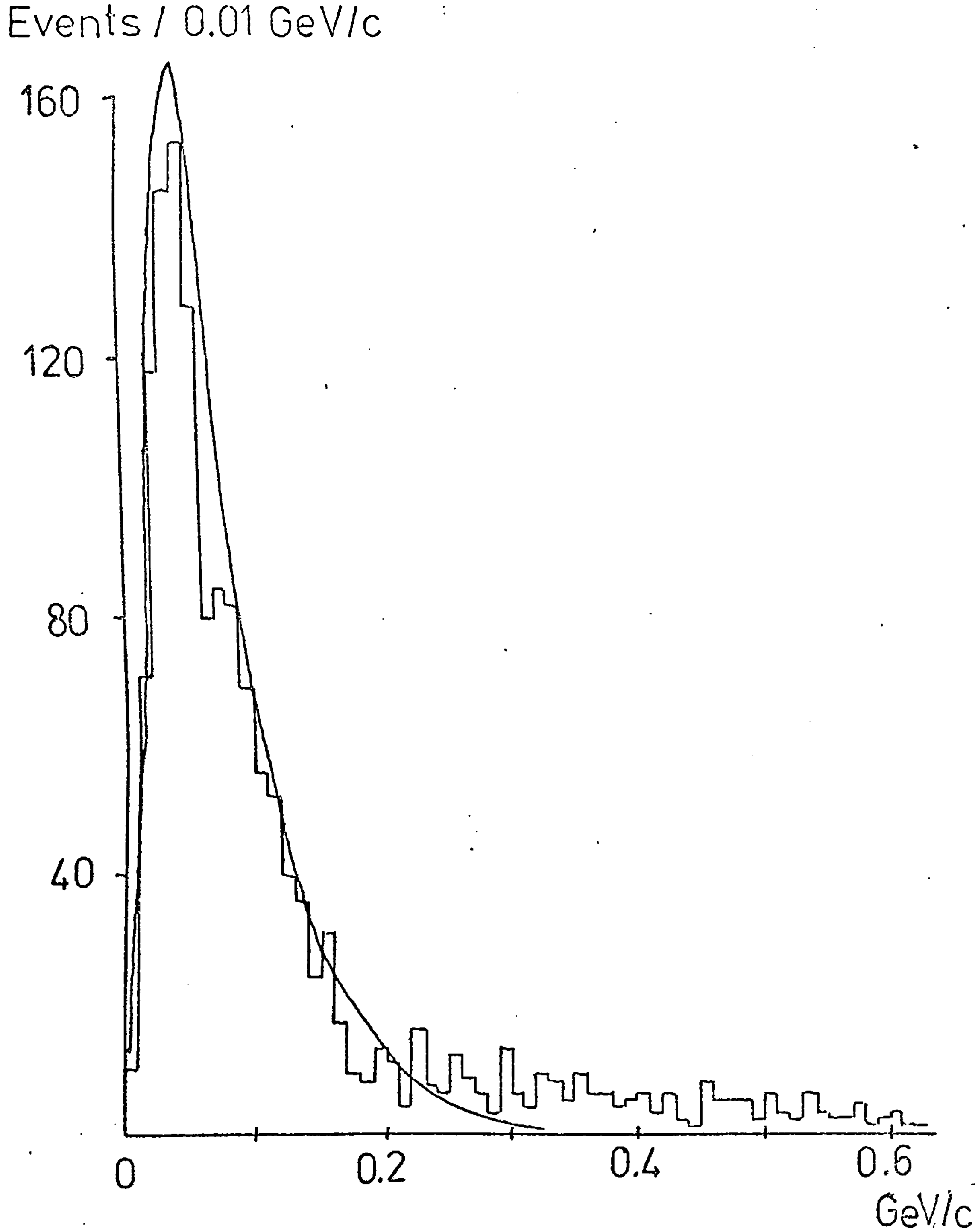

Fig. 3.5. Spectator Momentum Distribution
for Part 1 data with Hulthen Prediction

spectators with momentum over 300 MeV/c owing to the spectator momentum cut applied in its scanning instructions. The usual explanation for this excess is that, although the proton and neutron are loosely bound, they spend a certain amount of time close together, at which time the incoming beam could interact with both nucleons simultaneously. Also, after an interaction, the outgoing particles are within a couple of fermis of the spectator proton, and there is a few per cent probability of rescattering. Both of these effects result in fast, forward going nucleons and could cause the large spectator momentum tail.

However, the situation is far from clear and the spectator distributions show considerable dependence upon the peripherality of the reaction channels [Ref.10], and the number of particles in the final state. Fig. 3.6 shows an example of this in the $\pi\pi$ mass spectrum for spectator momentum over 300 MeV/c; f^o production would appear considerably reduced compared to f^o production for lower momentum spectators and compared to ρ^o production.

The spectator angles cos θ and ϕ are defined in Fig. 3.7, and the experimental distributions are shown in Figs. 3.8 (a) and (b). Figs. 3.9 (a) and (b) show the distributions for seen spectators only. For these angular distributions we have included data from both Parts 1 and 2 and have taken only events with spectator momentum less than 300 MeV/c. In the Impulse Approximation we expect the distribution in cos θ to depart somewhat from isotropy. The observed counting rate is proportional to the cross section and the flux while the latter is proportional to the relative

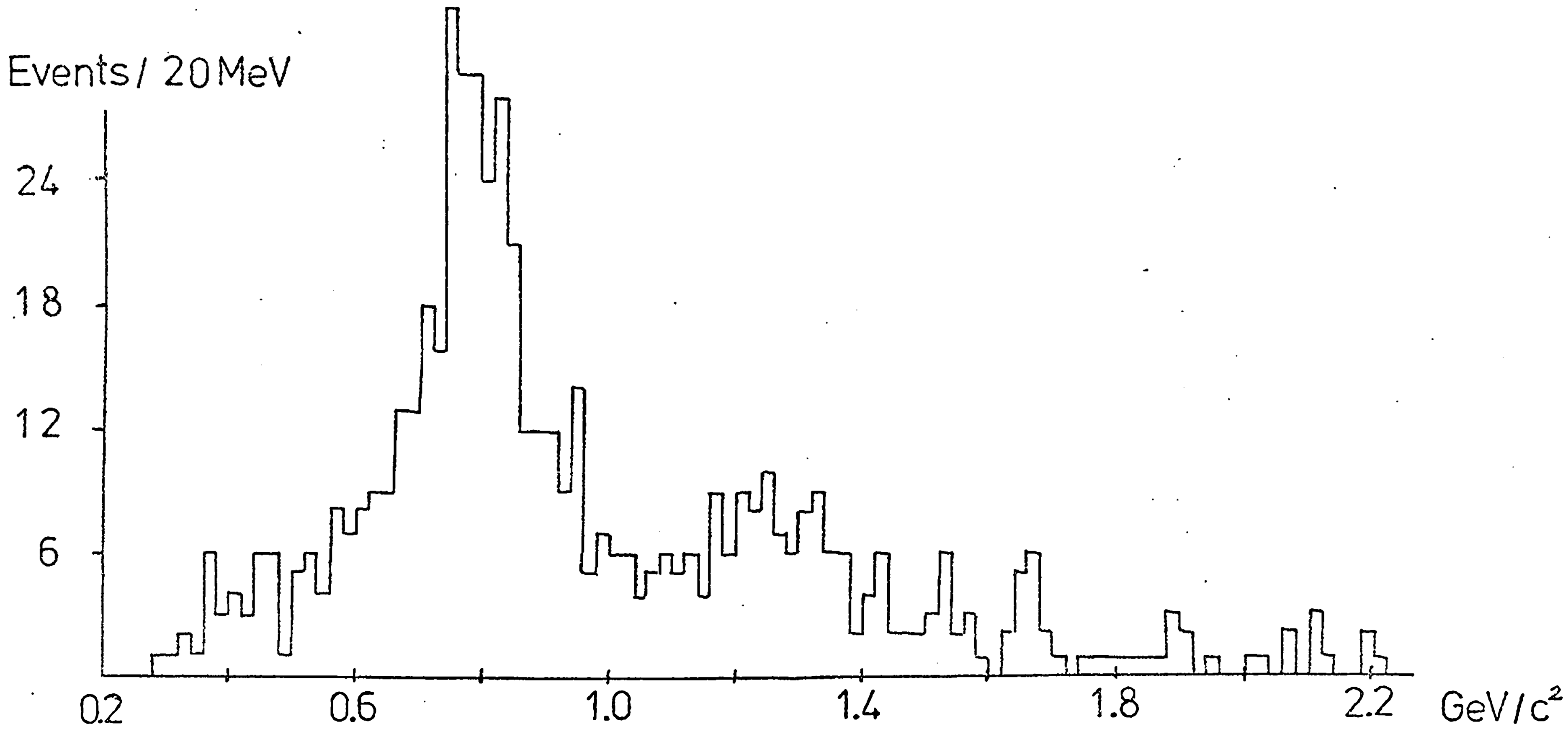

Fig. 3.6. $\pi^+\pi^-$ Mass Spectrum for $p_s > 300$ MeV/c

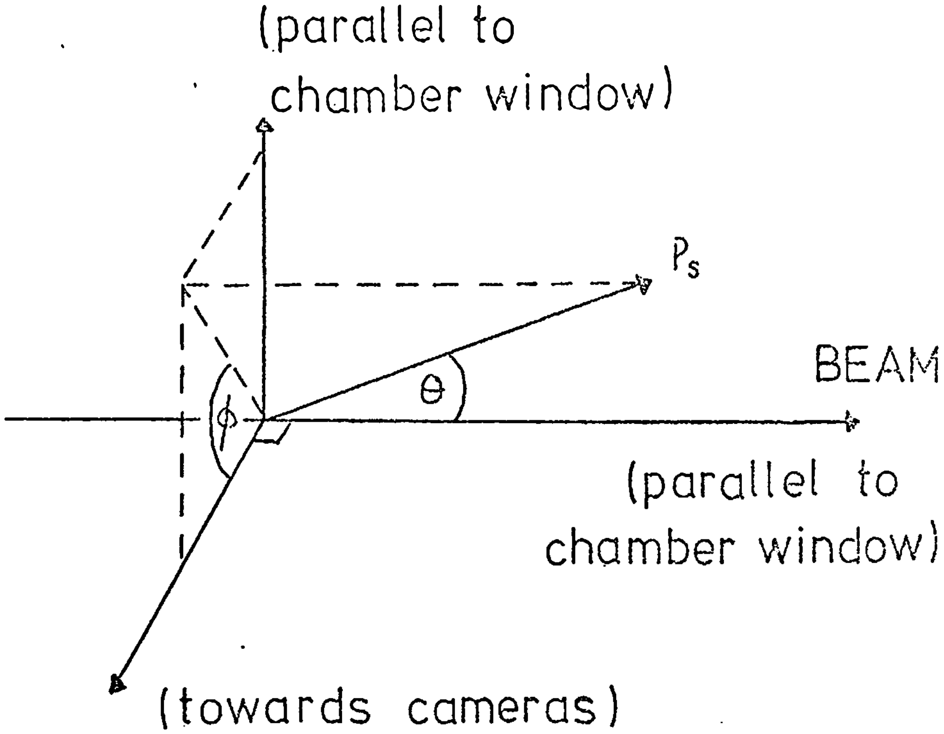

Fig. 3.7. Definition of cos θ and φ for Spectators

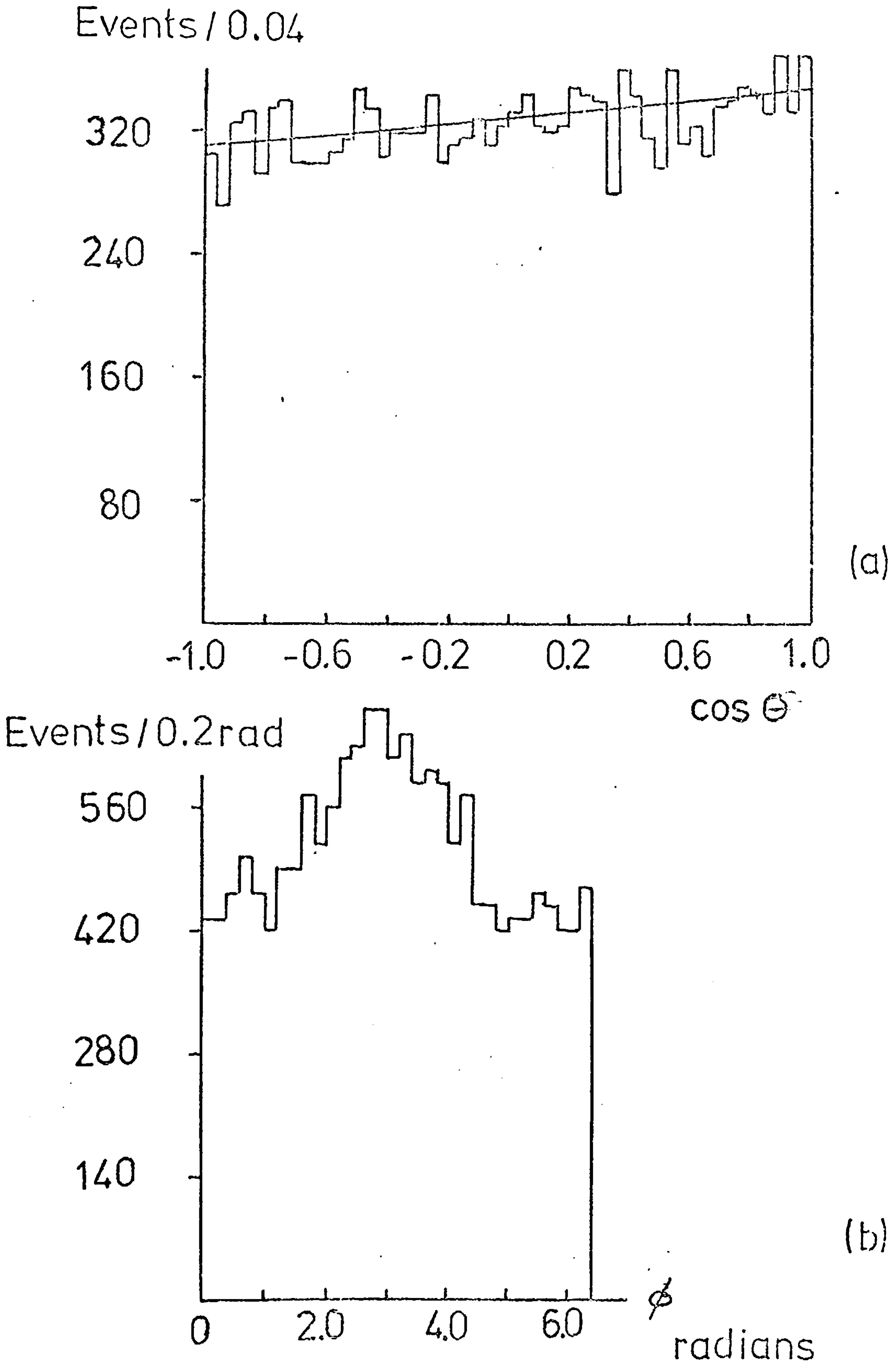

Fig. 3.8. Angular Distribution for all Spectators

(a) cos Θ , with Moller prediction

(b) ϕ

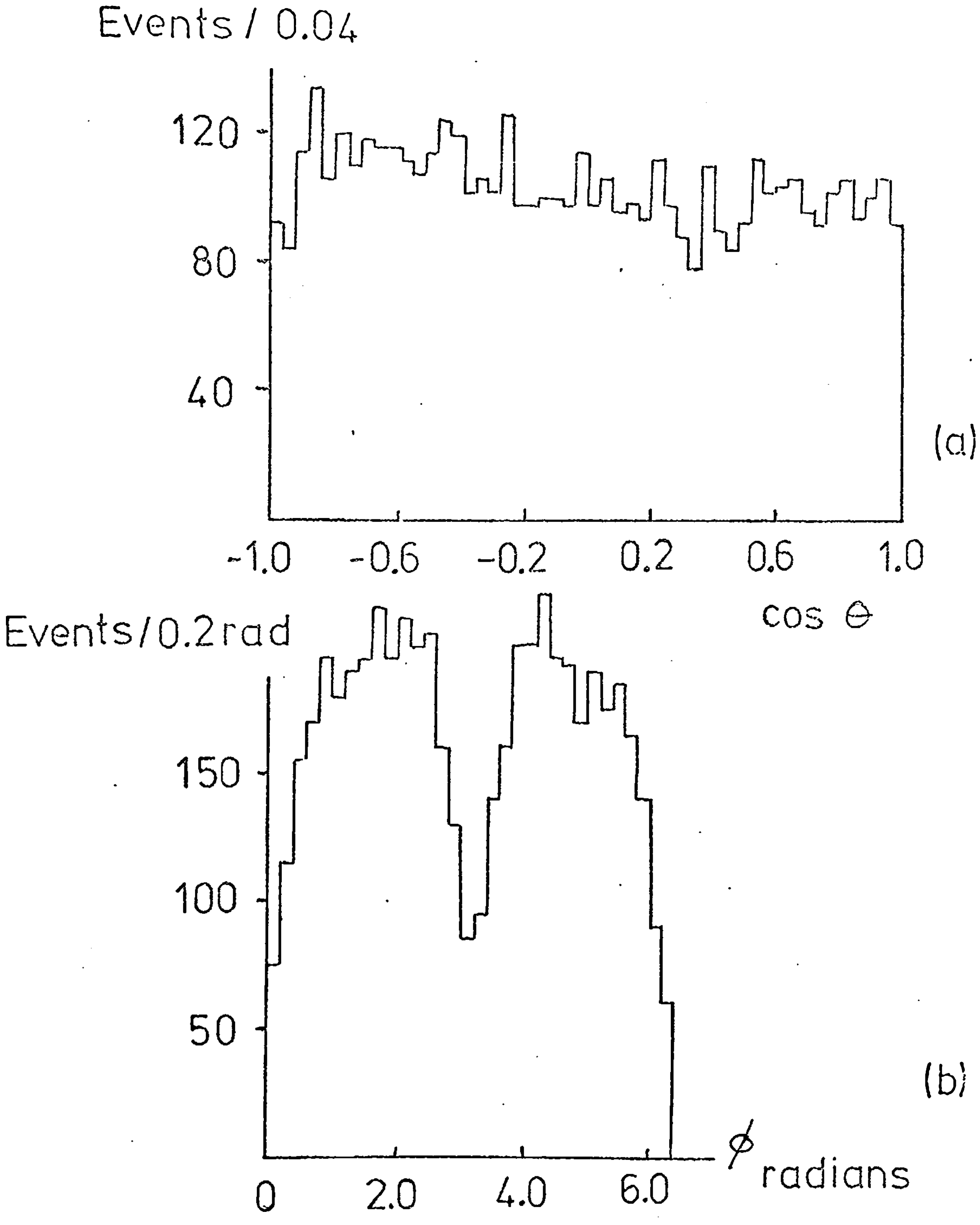

Fig. 3.9 Angular Distribution for Seen Spectators

(a) cos θ

(b) ϕ

velocity of beam and target so that high momentum, forward spectators are favoured. The experimental distribution can be predicted using the invariant flux factor of Moller [Ref. 11. 1]

This is

$$F = \sqrt{(p_b \cdot p_t)^2 - m_b^2 m_t^2} \; / \; (m_b m_t)$$

Here the momenta p_b and p_t are 4 - vectors and subscripts b and t refer to beam and target particles respectively. The Moller prediction, normalised to the data, is shown in Fig. 3.8 (a) for the Hulthen value j = 5.18. The anisotropy in cos θ, defined as

$$a = \frac{\text{Forward - Backward}}{\text{Forward + Backward}}$$

$$a_{\text{EXPT}} = 0.0266, \qquad a_{\text{MOLLER}} = 0.0278$$

is seen to be in good agreement with the Moller prediction.

Although cos θ is as expected we notice a severe distortion in the ϕ distribution. Fig. 3.9 (b) shows the distribution in ϕ for seen spectators only, the variation of which may be understood simply in terms of a scanning bias. Spectator protons coming towards ($\phi = 0$) or going away ($\phi = \pi$) from the cameras have a smaller projected length in the film plane and are therefore difficult to observe.

From the unequal limits we have given to the unseen spectator proton momenta (mentioned in the previous section), it can be seen that as the uncertainty in spectator momentum is larger in the z direction we should expect more unseen spectator protons to align themselves in the $\pm$ z direction rather than in either of the other two directions. This corresponds to an excess at (ϕ = 0) towards the cameras and (ϕ = π) away from the cameras, as well as the number we should expect at ϕ = 0 or π from the gap in the seen spectator distributions. However, the total distribution in ϕ for both seen and unseen spectators [Fig. 3.8 (b)] shows more aligned along ϕ = π than ϕ = 0. From knowledge of previous 2m chamber experiments the most probable explanation of this would be z - direction distortion in the reconstruction.

The centre of mass energy distribution for these events, leaving aside the spectator particle, is shown in Fig 3.10 (a) for all events, and in Fig. 3.10 (b) for events with spectator momentum greater than 100 MeV/c (corresponding to the four-prong events of the reaction $\pi^+ d \to pp\pi^+\pi^-$). The motion of the target nucleon results in a centre of mass energy spectrum about 300 MeV wide from a single incident beam momentum.

Fig. 3.11 is a scatter plot of the momentum of the slower proton (by definition the spectator) against the momentum of the faster proton. The degree of overlap of the distribution below 300 MeV/c can be seen, stressing the need for care when undertaking an analysis involving the interaction proton. An analysis using just the mass and four momentum transfer to the $\pi\pi$ system would not depend on the choice of reaction proton. However, an analysis which required the determination of decay angles, via the overall reaction centre of mass, could be affected to some extent.

Another effect of doing an experiment in deuterium, the Pauli effect, is reviewed for reaction (1) in the following section. Fig. 3.11 shows the loss of events at low $|t|$ due to this effect and a scanning bias, also

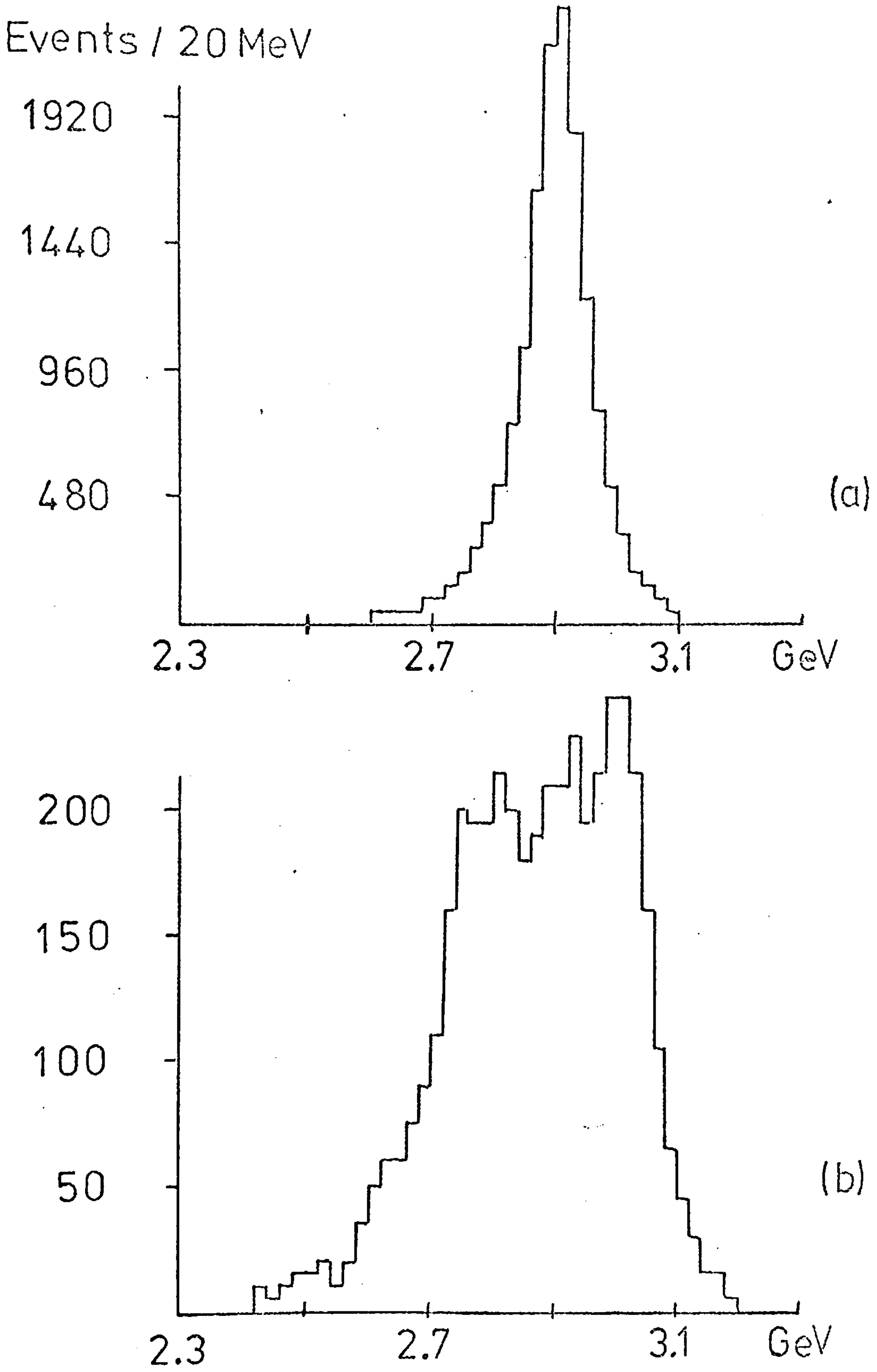

Fig. 3.10 Distribution of Centre of Mass Energy

(a) All events

(b) events with $p_s > 100$ MeV/c

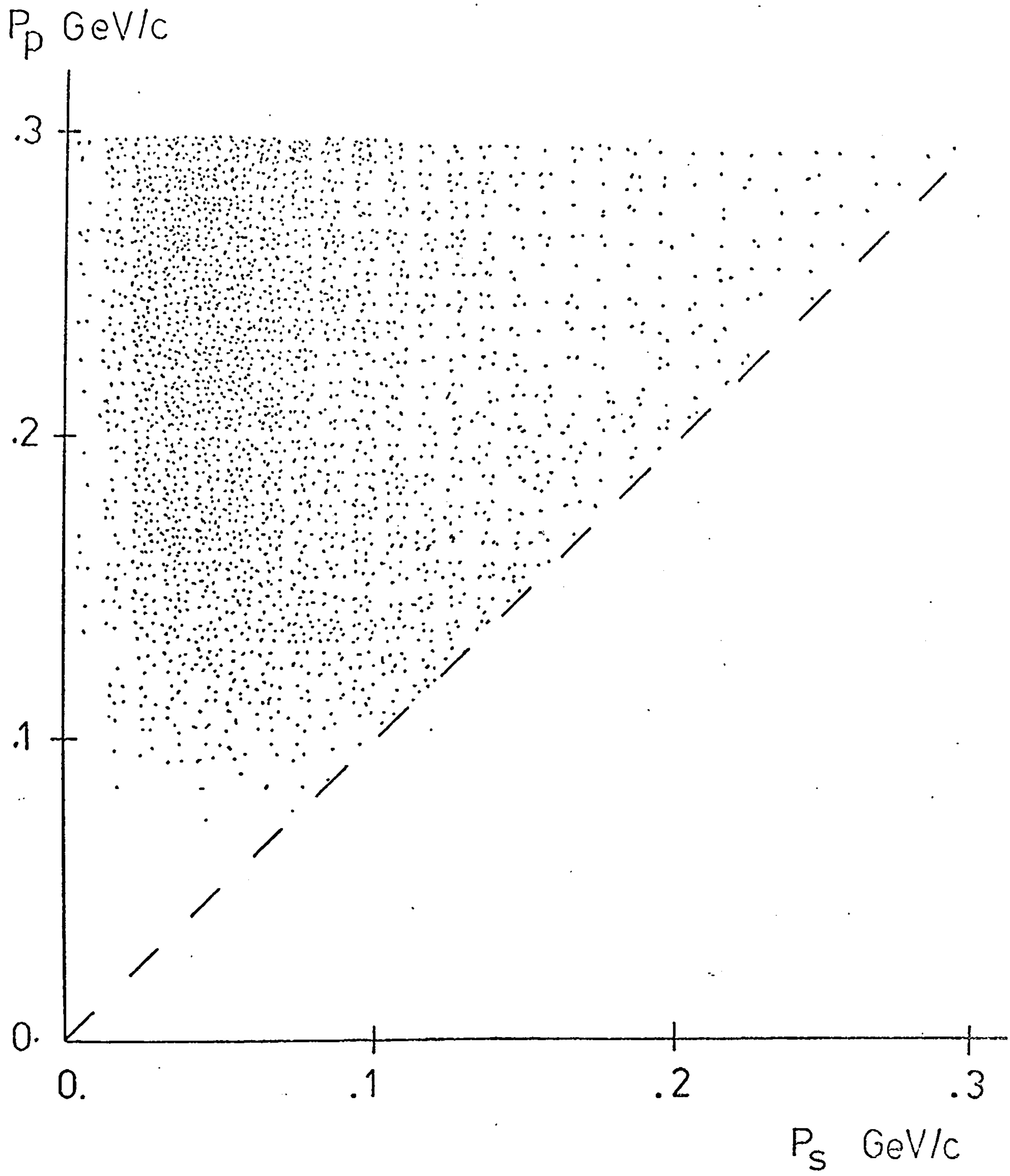

Fig. 3.11 Scatter plot of Reaction Proton Momentum (for $P_p < 300$ MeV/c) against Spectator Momentum.

discussed later.

3.3. Pauli Exclusion and the Drop in Differential Cross Section at Low Momentum Transfer.

A correction should be applied to this channel to correct for Pauli exclusion losses of certain angular momentum final states between the two protons. While the effect makes a negligible difference to the total cross section, it greatly affects events with $|t|(d \to pp) < 0.1\ (\text{GeV}/c)^2$. A quantitative treatment of the Pauli effect has been given by Benson [Ref. 10.] for several ideal exchange mechanisms.

In the Impulse Approximation, the charge exchange differential cross section in deuterium is written [Ref. 12.].

$$\frac{d\sigma}{dt}^{D} = \frac{d\sigma}{dt}^{H}_{\text{flip}} \left[1 - \frac{1}{3} H(t)\right] + \frac{d\sigma}{dt}^{H}_{\text{non flip}} \left[1 - H(t)\right]$$

where $\frac{d\sigma}{dt}^{H}_{\text{flip}}$ and $\frac{d\sigma}{dt}^{H}_{\text{non flip}}$ are the spin flip and non-flip free nucleon differential cross sections. The deuteron form factor, H (t), is given by

$$H = \int \psi^{*}(\vec{r})\, e^{(-i\vec{q}.\vec{r})}\, \psi(\vec{r})\, d\vec{r}$$

where ψ is the deuteron spatial wave function and $\vec{q}$ is the difference between the initial and final meson momenta in the laboratory.

For pion exchange one expects only spin flip of the interaction nucleon, allowing the differential cross section in deuterium including the Pauli effect to be written

$$\frac{d\sigma}{dt}^{D} = \frac{d\sigma}{dt}^{H}_{\text{flip}} \left[1 - \frac{1}{3} \quad H(t) \right]$$

The unpolarised deuteron can be described as three states of nucleon spin, up-up, down-down, and up-down plus down-up. If a spin is flipped in each of these states, only the third state necessarily becomes a state of S = 1 and is therefore forbidden, giving the (1 - 1/3) factor.

The deuterium reduction factor, R, defined

$$R = \frac{d\sigma}{dt}_{\text{deuterium}} \bigg/ \frac{d\sigma}{dt}_{\text{free neutron}}$$

computed for low momentum transfer is given in Table 3.1.

Another loss of events at low momentum transfer arises from a scanning bias. For a proton to be seen in a bubble chamber its minimum track length in the film plane must be about 1 mm. If the track dips towards or away from the cameras, the track must be correspondingly longer such that the projected length in the film plane remains the same. For our three prong events (i.e. events where the spectator proton is unseen) there is a possibility at low $|t|$ that the laboratory momentum of the reaction nucleon is so low, or has a dip such, that it remains unseen also. Even if the proton is just visible the probability of it being seen by an operator is very low. The result is a loss of events into the two prong category.

To estimate the magnitude of this effect we can study the spectators themselves. In Table 3.2. is shown the Visibility Factor for spectators

Table 3.1

Deuterium Reduction Factor for One Pion Exchange from the Pauli Exclusion Principle

BIN	$\lvert t \rvert (GeV/c)^2$	R
1	0 - 0.01	0.740
2	0.01 - 0.02	0.830
3	0.02 - 0.03	0.875
4	0.03 - 0.04	0.900
5	0.04 - 0.05	0.919
6	0.05 - 0.06	0.932
7	0.06 - 0.07	0.943
8	0.07 - 0.08	0.950
9	0.08 - 0.09	0.957
10	0.09 - 0.1	0.963

Table 3.2

Visibility Factor for Spectators

BIN	Momentum of Spectators (MeV/c)	V
1	0 - 100.08	0.114
2	100.08 - 141.73	0.853
3	141.73 - 173.82	0.989
4	173.82 - 201.0	1.0
5	201.0 - 225.03	1.0
6	225.03 - 246.86	1.0
7	246.86 - 267.01	1.0
8	267.01 - 285.84	1.0
9	285.84 - 303.601	1.0
10	303.601 - 320.461	1.0

defined as

V = No. Seen Spectators / Total Events

between certain laboratory spectator momentum limits. These limits correspond to the values of momentum transfer in Table 3.1. if the spectator had had zero initial laboratory momentum within the deuteron. This gives us a "Range-Visibility Curve" for the bubble chamber.

It is now necessary to assume that the Range-Visibility Curve for interaction protons is the same as that for spectators. As we have averaged over all spectators to obtain the curve, we can assume the curve to be also true for interaction protons provided they are produced isotropically in the forward hemisphere. The extent to which this is true is shown in Figs. 3.12. (a) to (d) for four intervals of momentum transfer. The distributions in cos θ for interaction protons can be seen to approximate to an isotropic distribution in the forward hemisphere as we reduce $|t|$. Fig. 3.12 (e) shows the distribution in ϕ for interaction protons for $|t| < 0.1\ (\mathrm{GeV}/c)^2$ clearly indicating the scanning bias.

For each value of $|t|$ we next generate the initial Fermi momentum of the neutron according to the Hulthen wave function, and thus predict the final momentum of the interaction proton in the laboratory. For each reaction proton so generated we have the Range-Visibility probability in the laboratory from Table 3.2., enabling us to predict, on average, the likelihood of seeing reaction protons with a certain value of $|t|$. This likelihood, which is a correction of V in Table 3.2. for the effect of the moving neutron target, is shown in Table 3.3.

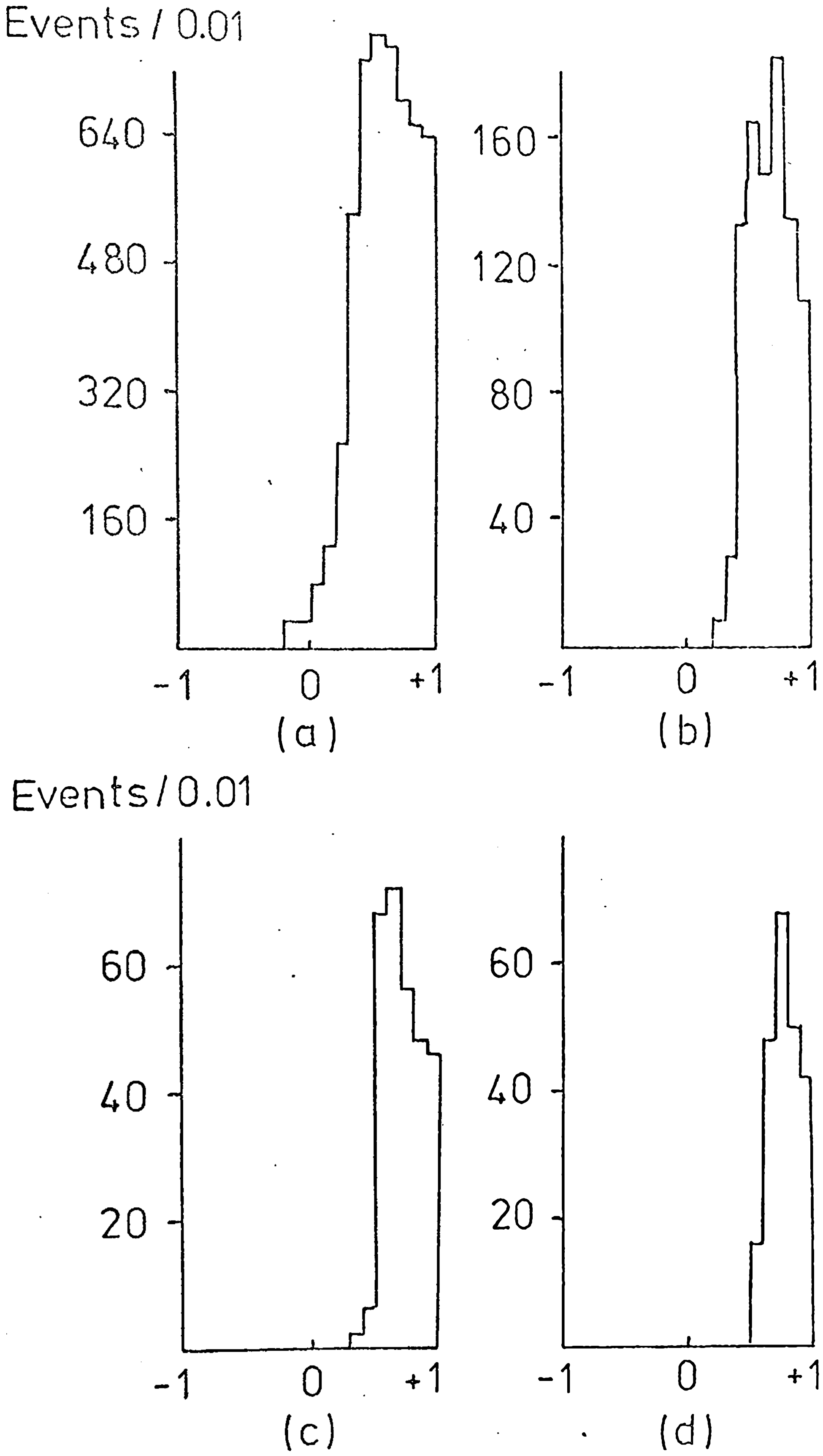

Fig. 3.12 cos θ Distributions about beam for Reaction Protons

(a) $|t| < 0.1$

(b) $|t| = 0.3 - 0.4$

(c) $|t| = 0.6 - 0.7$

(d) $|t| = 0.9 - 1.0 \ (\mathrm{GeV}/c)^2$

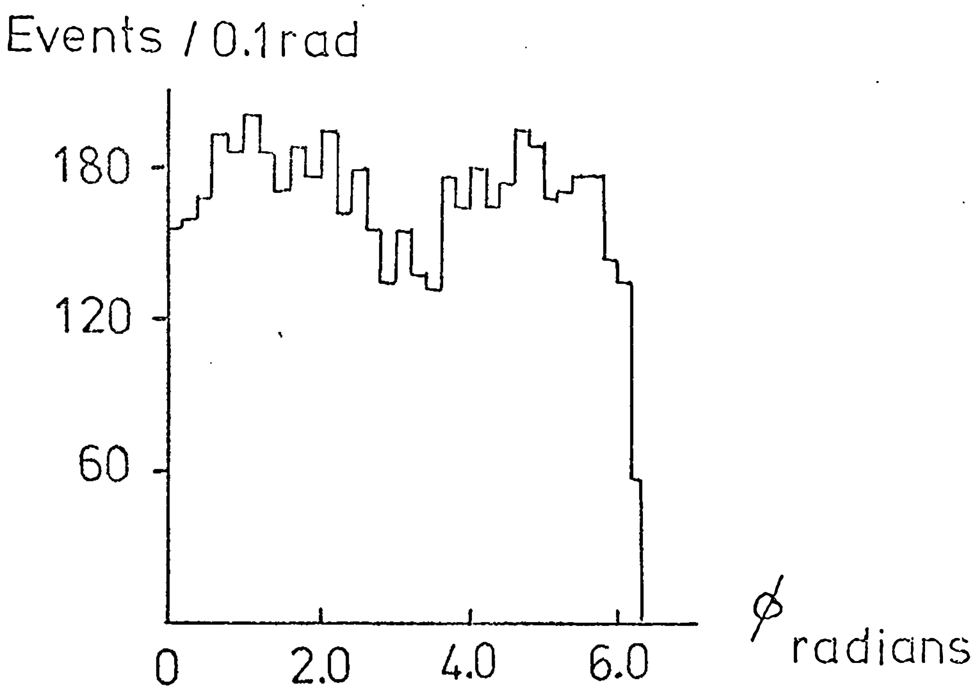

Fig. 3.12. (e) ϕ Distribution about beam for Reaction Protons for $|t| < 0.1$ (GeV/c)^2

Distributions in ϕ for $|t| > 0.1$ (GeV/c)^2 are isotropic.

Table 3.3

BIN	$\|t\|$ $(GeV/c)^2$	Visibility of Final State Protons	Observed Fraction of the Total Differential Cross Section(*)
1	0 - 0.01	0.173	0.128
2	0.01 - 0.02	0.587	0.487
3	0.02 - 0.03	0.802	0.702
4	0.03 - 0.04	0.895	0.806
5	0.04 - 0.05	0.932	0.857
6	0.05 - 0.06	0.956	0.891
7	0.06 - 0.07	0.966	0.911
8	0.07 - 0.08	0.978	0.929
9	0.08 - 0.09	0.983	0.941
10	0.09 - 0.1	0.987	0.950

(*) includes the Pauli effect

This method would not be valid if the angular distribution, and hence the visibility, of final state reaction protons was very different from that of spectators. At higher reaction proton momenta (when the proton is clearly visible anyway) this discrepancy is obvious, the reaction protons being very forward peaked in the laboratory while the spectators are isotropic. In this region our assumption is incorrect. However, at lower $|t|$ the reaction protons tend towards isotropy within the forward himisphere, allowing this assumption to be made. By dividing the original spectator data into regions of $\cos\theta$, it is possible to obtain Range-Visibility Curves at each value of $\cos\theta$, enabling the experimental interaction proton spectrum to be used without our assumption. If the Range-Visibility Curves for each value of $\cos\theta$ are found to be similar, the actual shape of the reaction proton distribution becomes unimportant. By dividing the data in this way we have no evidence for any sizeable change in the result.

Rather than use spectators to calibrate the Range-Visibility Curve, a theoretical calculation of the scanning bias can be made assuming that the reaction protons are isotropic and that there exists a sharp cut-off in the visible projected length in the chamber. Such calculations are in general qualitative agreement with the scanning bias found using spectators .

The total effect on the data, namely the product of this scanning bias with the Pauli effect, is shown in Table 3.3.

3.4. Resolution of the $\pi\pi$ System

The resolution, or error in the effective mass of the π π system, stems from the error in track measurement inherent in any bubble chamber experiment. Coulomb scattering errors combine with machine accuracy and the statistical spread of Master Points to produce an overall measurement error for a track on film. Typical measurement errors for $\pi^+ d$ are ~ 2 μ on film for the beam track and ~ 5 μ for secondary tracks whose momenta are determined from helix fitting. These measurement errors result in the measured errors in track momentum and angles. Stopping tracks, whose momenta are detemined by a range measurement, usually have smaller errors. The π π system is better determined than most other mass combinations owing to the pion tracks being relatively faster and thus having smaller multiple scattering errors than other outgoing tracks. Fitting lowers the track errors but the long pion track values and errors remain largely unchanged.

For each track in the π π system we know the fitted azimuth and dip angles and the momentum at the production vertex together with their errors. The effective mass-squared can be expressed.

$$M^2 = 2\mu^2 + 2E_1E_2 - 2\vec{p}_1 \cdot \vec{p}_2 \quad \text{with}$$

$$\vec{p}_1 \cdot \vec{p}_2 = p_1 p_2 \left([\cos d_1 \cos d_2] [\cos a_1 \cos a_2 + \sin a_1 \sin a_2] + \sin d_1 \sin d_2 \right)$$

and a_i, d_i, p_i are the azimuth, dip and momentum for track i. This expression was differentiated to obtain the resolution.

The resolution has been found to be 5 or 6 MeV in the rho region,

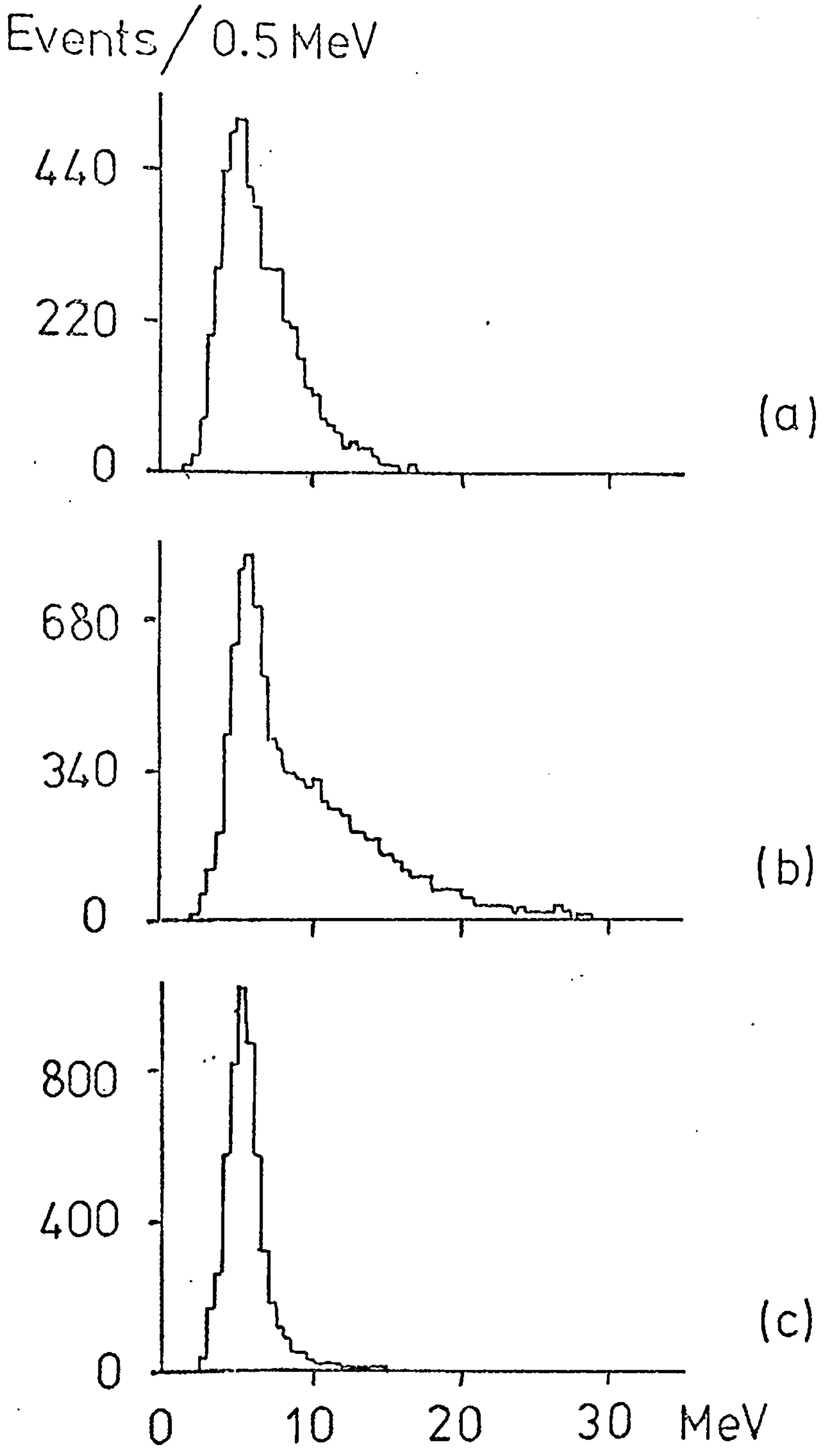

Fig. 3.13. Resolution of π - π Mass

(a) All seen spectator events

(b) All unseen spectator events

(c) All events in the ρ^0 region.

rising to about 20 MeV at the highest $\pi\pi$ mass. Figs. 3.13 (a) and (b) show the spread in resolution for the π π spectrum for seen and unseen spectators respectively; while Fig. 3.13 (c) shows the spread in resolution within the rho region only. The distributions have been found to be identical for both Rutherford and Birmingham data and to be insensitive to any cuts in the data other than that of a seen or unseen spectator, as shown by Figs. 3.13 (a) and (b). The resolution values quoted above have been determined using only the diagonal elements of the full error matrix owing to the off-diagonal terms not being easily accessible in the Kinematics program. However, this omission should have a very small effect on the result as the off-diagonal elements for a 4 - c fit are very small quantities.

Although the resolution in this experiment is no larger than to be expected in a bubble chamber experiment, it must be noted that the resolution is barely adequate for an investigation of, say, ρ - ω interference. Evidence for a four standard deviation dip exists in our data at the ω^o mass in one 5 MeV bin, leaving its significance doubtful when compared with the resolution. This necessarily governs the mass interval size in which the data may be reliably studied. In all the analyses which follow in this report, data have been collected into bins several times larger than the nominal resolution.

3.5. General Features of the Data.

The general features of reaction (1) are shown in the prism plot [Ref. 13] of Fig. 3.14 (a) in which the mass combinations M^2 ($\pi^+\pi^-$)

Fig. 3.14 (a) Prism Plot $\pi^+ n \longrightarrow p\pi^+\pi^-$

PRISM PLOT $\pi^+ n \rightarrow p \pi^+ \pi^-$. 4 GeV/c.

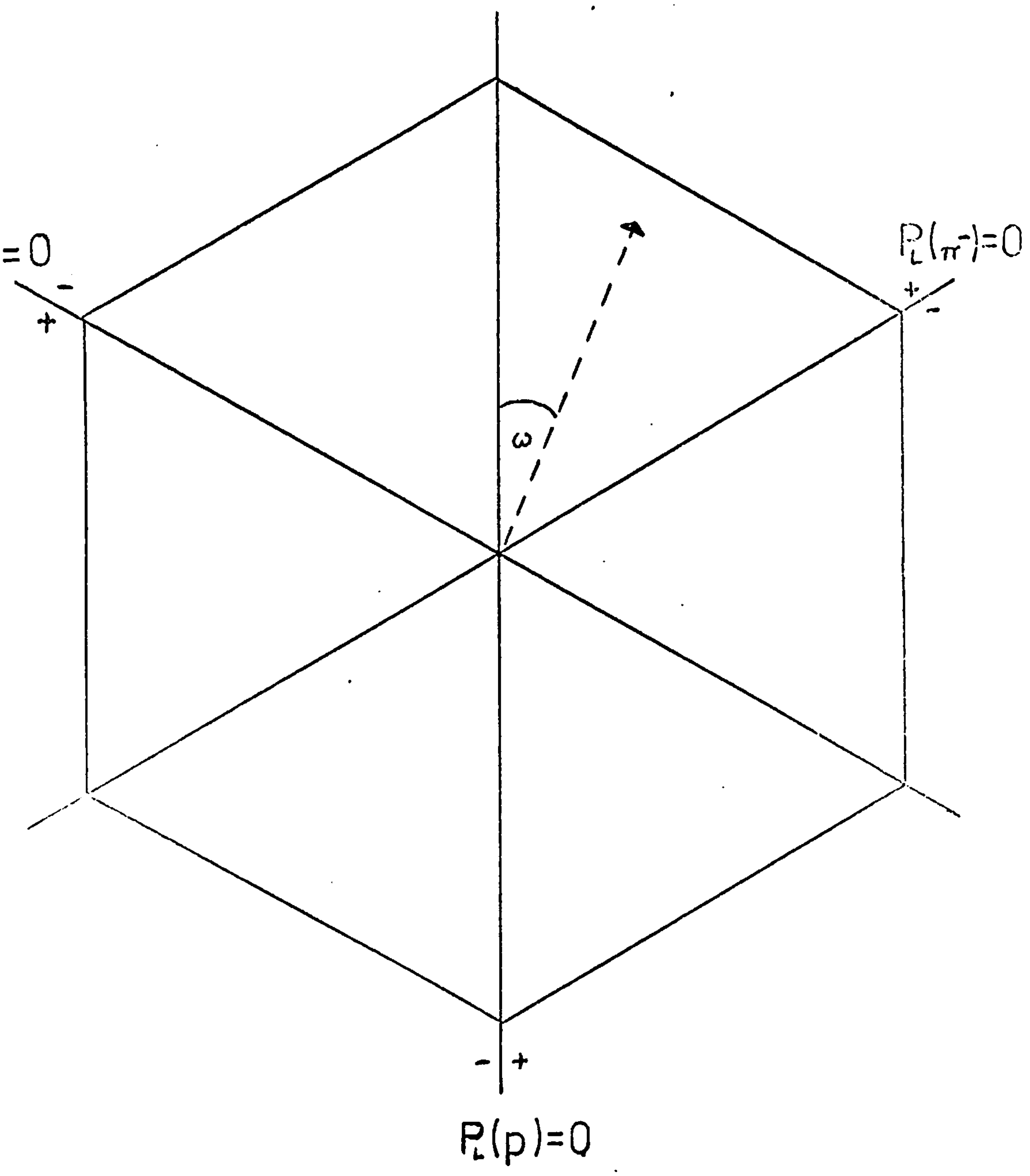

Fig. 3.14 (b) Definition of Van Hove angle as used in Fig. 3.14 (a) in terms of π^+, π^- and proton longitudinal momenta.

Fig. 3.15 Dalitz Plot p, π^+, π^-

Particle 1 = proton

Particle 2 = π^+

Particle 3 = π^-

Units are $(GeV/c^2)^2$

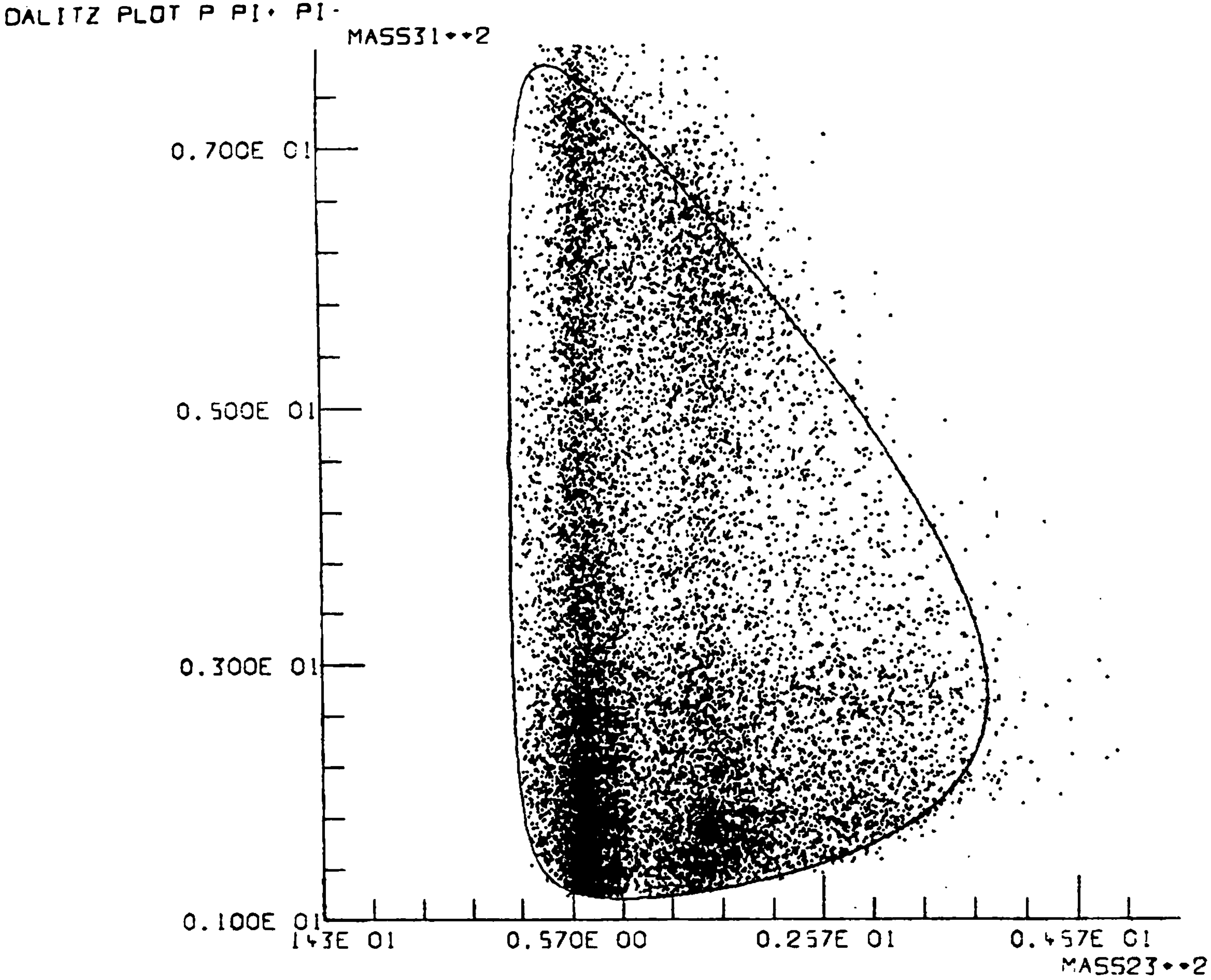
DALITZ PLOT P PI+ PI-
MASS31**2
0.700E 01
0.500E 01
0.300E 01
0.100E 01
143E 01
0.570E 00
0.257E 01
0.457E 01
MASS23**2

and M^2 (p π^-) are plotted parallel to the horizontal axes and the Van Hove angle ω is plotted parallel to the vertical axis. Fig. 3.14 (b) defines the Van Hove angle in terms of the centre of mass longitudinal momenta of the π^+, π^- and reaction proton. Events in which the $\pi^+ \pi^-$ system goes forward in the overall centre-of-mass lie in the upper half of this plot. Fig. 3.15 shows the Dalitz plot obtained by projecting the prism plot onto its horizontal plane.

The following main features of the prism plot are observed:-

(a) Strong bands due to forward ρ^o and f^o production. The bands have the characteristic appearance of a decay angular distribution peaked strongly forwards and backwards in the resonance centre-of-mass.

(b) Some backward production of these same states.

(c) An accumulation of events at high M^2 ($\pi^+\pi^-$), but with low M^2(p π^-), which could be interpreted as due to g^o production, or to production of a low mass N^* in the p π^- system. We note that any g^o production should be symmetric in M^2 (p π^-), although interference could alter its distribution. The distribution of the $\pi\pi$ invariant mass, $M\pi\pi$, is shown in Fig. 3.16; in this diagram one event corresponds to a cross section of 0.136 ± 0.011 μb (See Chapter 4.)

The peripheral nature of the data is further emphasised by a plot of the forward part of the centre-of-mass scattering angle from the beam to the $\pi\pi$ system, cos θ^*, in Fig. 3.17.

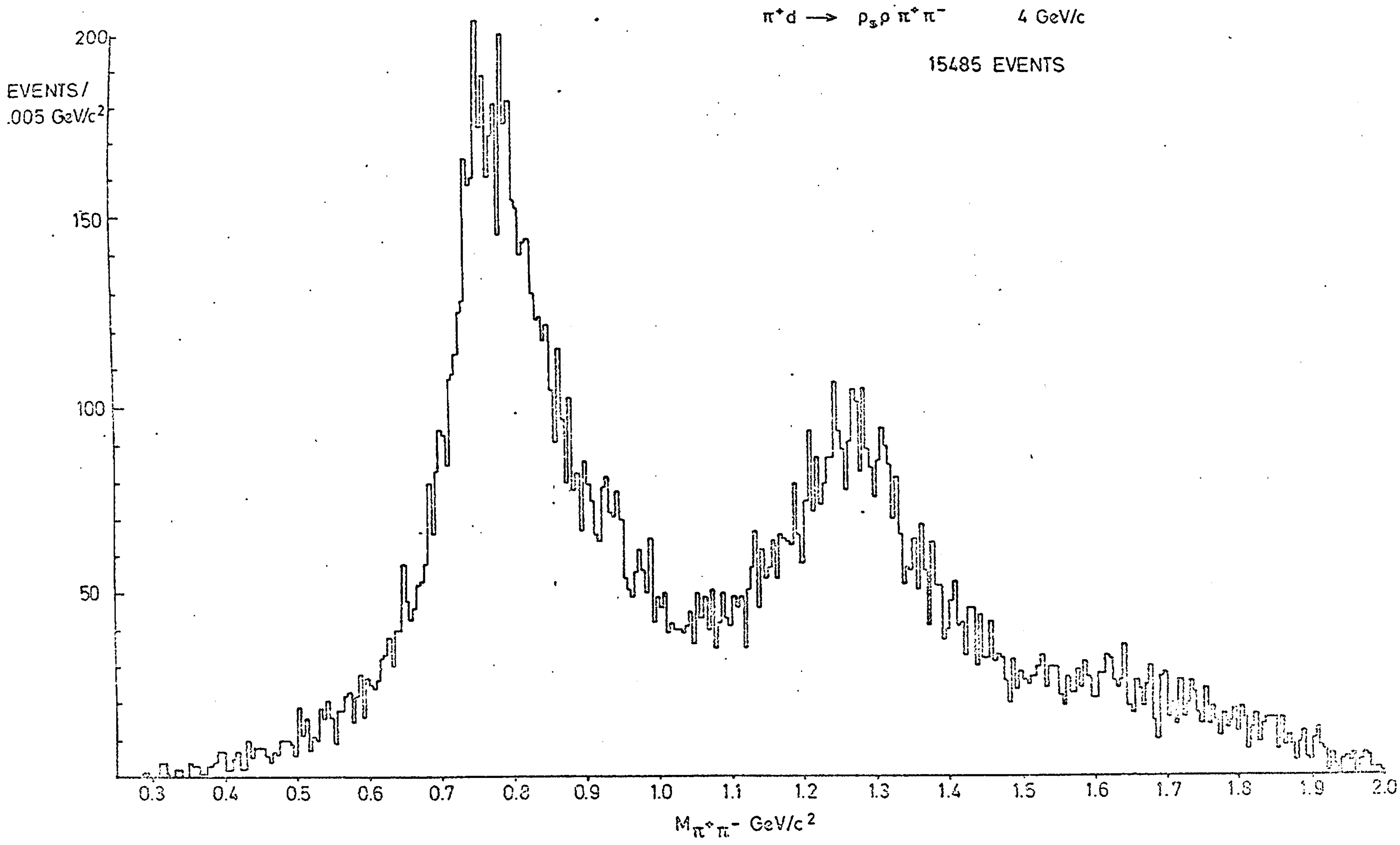
$\pi^+ d \longrightarrow p_s p \pi^+ \pi^-$ 4 GeV/c
15485 EVENTS
EVENTS/ .005 GeV/c^2
200
150
100
50
0.3
0.4
0.5
0.6
0.7
0.8
0.9
1.0
1.1
1.2
1.3
1.4
1.5
1.6
1.7
1.8
1.9
2.0
$M_{\pi^+\pi^-}$ GeV/c^2

Fig. 3.16

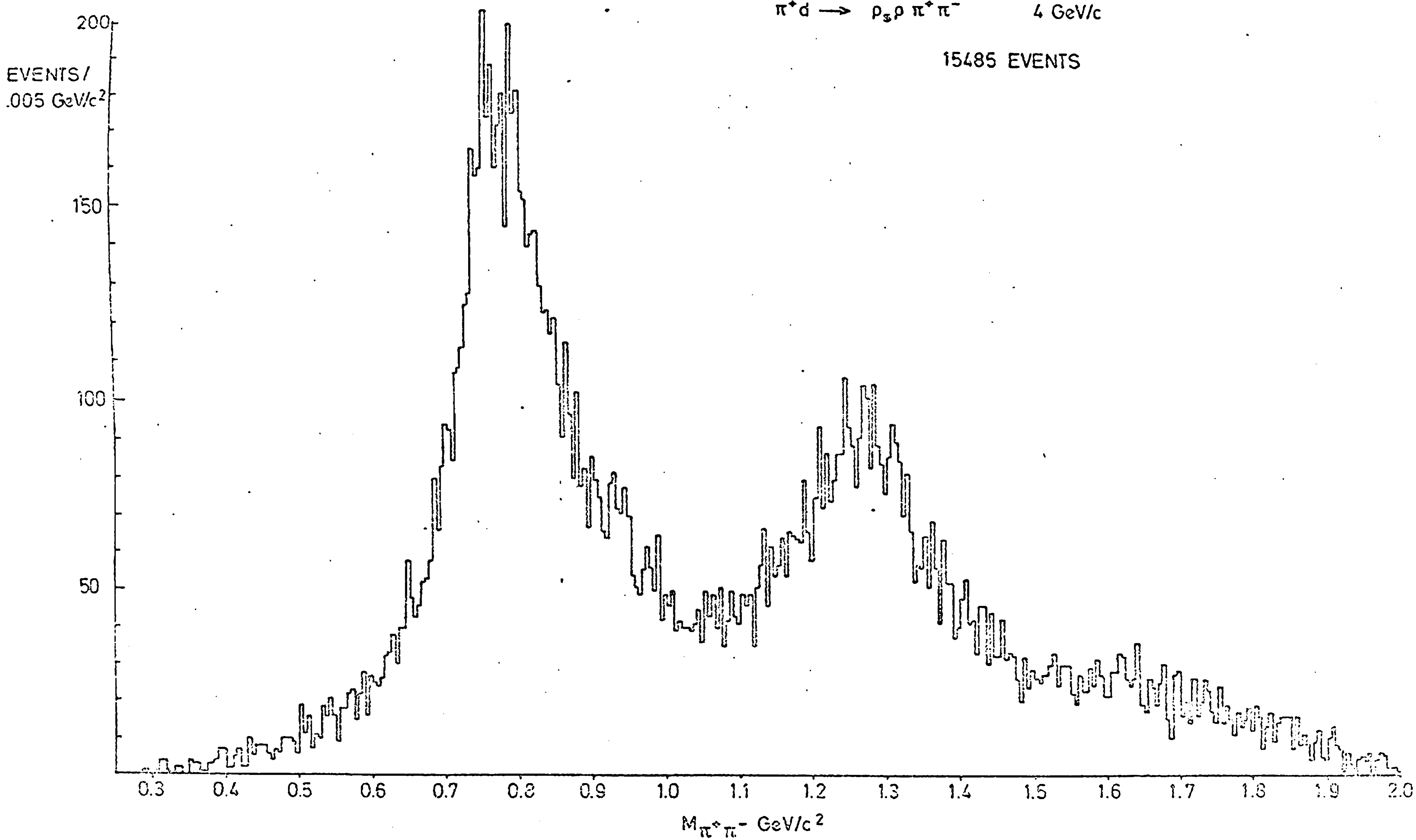
$\pi^+ d \longrightarrow p_s p \pi^+ \pi^-$ 4 GeV/c
15485 EVENTS
EVENTS/
.005 GeV/c²
200
150
100
50
0.3
0.4
0.5
0.6
0.7
0.8
0.9
1.0
1.1
1.2
1.3
1.4
1.5
1.6
1.7
1.8
1.9
2.0
$M_{\pi^+\pi^-}$ GeV/c²

Fig. 3.16

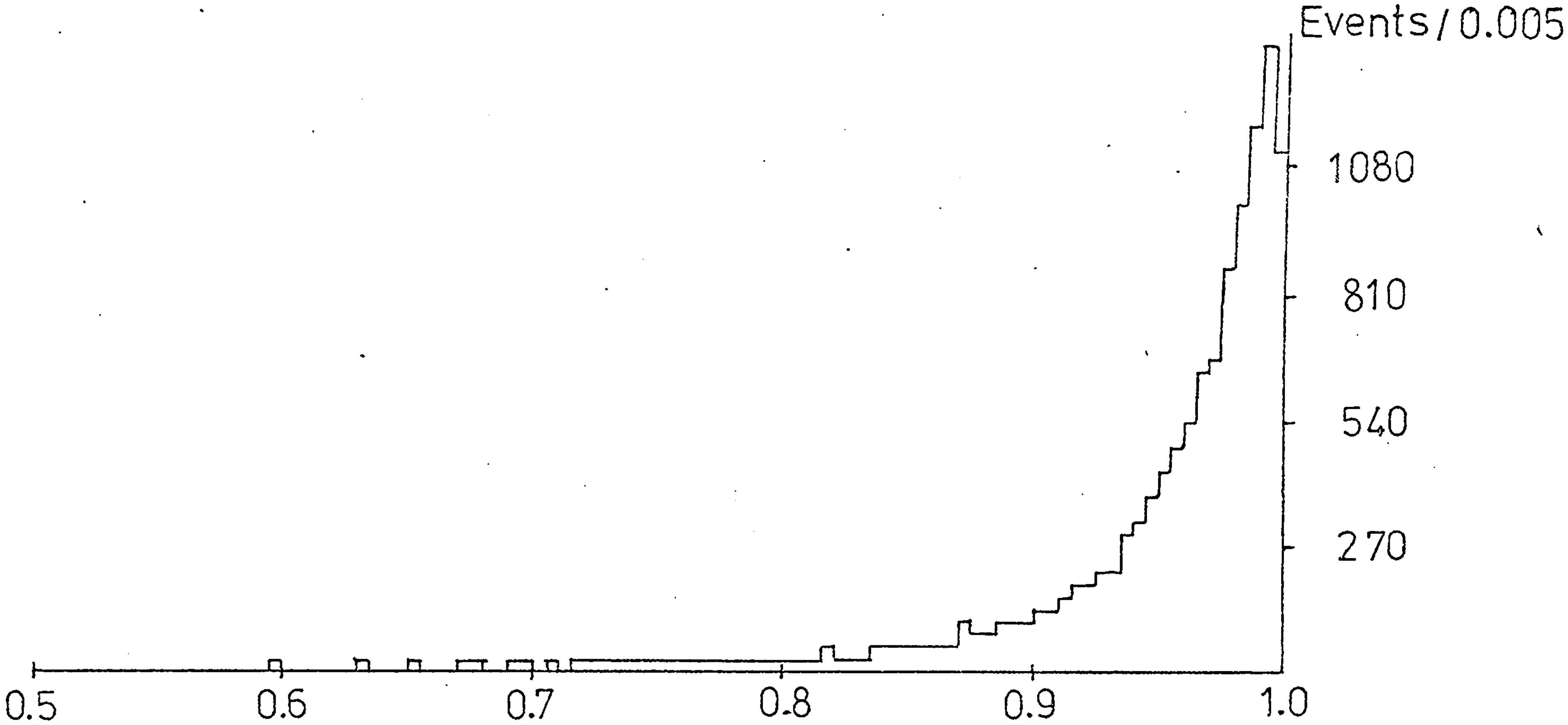

Fig. 3.17 Distribution of cos θ^*

3.6. Background N^* Production.

N^* production, likely to provide the most serious background in the analysis of ρ^0 and f^0 systems, has been studied in some detail at the Rutherford laboratory [Ref. 14.]. As the results are of importance for our analyses we summarise them here.

The possible effects of any incoherent N^* contribution to our ρ^0 and f^0 samples have been studied using a Monte Carlo method, taking values for the cross-section for N^* production in the charge conjugate reaction

$$\pi^- p \longrightarrow N^* (1400)\, \pi^- \qquad (2)$$

from previously reported experiments [Ref. 15].

The experiments of Ref. 15. are at various energies, including some at higher energies, where the separation on the Dalitz Plot between meson bands and N^* bands may be expected to be better than at 4 GeV/c. Since N^* production is a diffractive process, its cross section is expected to be roughly constant with energy, and so these higher energy values of the cross-section for reaction (2) have been used in estimating a cross-section for the process

$$\begin{array}{l} \pi^+ n \longrightarrow N^* (1400)\, \pi^+ \\ \quad\quad\quad\; \lfloor\!\!\rightarrow p\, \pi^- \end{array} \qquad (3)$$

of 0.13 m b.

By generating Monte Carlo events with an assumed momentum transfer distribution from the target to the N^* of e^{7t} (t in $(\mathrm{GeV/c})^2$), and a decay angular distribution in the N^* centre of mass corresponding to a P wave $p\pi^-$ system, an estimate can be made of the overall N^* contamination of the ρ^o sample of 3% and of the f^o of 1%.

Also estimated is the contribution from N^* production to the unnormalised moments of the $\pi\pi$ decay angular distribution. The result of the study was that none of the conclusions drawn from our analyses of the data are changed significantly by including these background effects.

It should be pointed out that this treatment of backgrounds applies only to incoherent N^* production. If a diffractive N^* is produced coherently with resonances in the $\pi\pi$ system, the interpretation of the $\pi\pi$ density matrix becomes more complicated.

CHAPTER 4

Cross Section Measurements in $\pi^+ d \rightarrow pp\,\pi^+\pi^-$

4.1. Introduction.

This chapter describes the experimental determination of the cross section

$$\sigma\,(\pi^+ d \longrightarrow pp\,\pi^+\pi^-) \qquad (1)$$

and the fractional cross sections

$$\sigma\,(\pi^+ d \longrightarrow pp\,\rho^0) \qquad (2)$$

$$\sigma\,(\pi^+ d \longrightarrow pp\,f^0) \qquad (3)$$

These cross sections are compared with measurements at different energies and determinations in the charge-conjugate π^- p mode. A comparison is made between π^+ d and π^- p in the determination of angular distributions and resonance decay matrix elements using data from this experiment and a 4 GeV/c π^- p experiment.

4.2. Experimental Cross Sections.

Six segments scattered throughout Part 2 of the experiment were resubmitted for scanning during the course of measurement so as to provide an estimate of the scanning operators' efficiency.

After both operator scans the film was viewed by physicists and each event found by the operators was checked for correctness. In this way it was possible to find the number of events correctly found by the operators on each of the two scans.

Making the assumption that both operator scans are truly independent and that any loss of events by a particular operator happens in a random way (which is not strictly true as some events are inherently less observable than others) we obtain

$$E_1 = N_1/N \qquad E_2 = N_2/N \qquad N = N_1 N_2/N_c$$

where N_1 and N_2 are the number of events correctly found by the operators on scan 1 and scan 2 respectively, N_c is the number correctly found on both scans, N is the total number of events on the film and E_1 and E_2 are the efficiencies of the operators on scan 1 and scan 2 respectively.

The numbers obtained for the six segments are listed in Table 4.1. divided into four prong and six prong categories. Only those four and six prongs in which we are interested in Part 2 are included. The efficiency of a single scan (taken as E_1) at Birmingham is seen to be 83.6% for four prongs and 84.9% for the six prong category.

During the physicist check scan a count was kept of the beam flux and the total interaction rate through the fiducial region. This count, on 20% of the six segments, was made on frames with frame numbers ending in 'O' or '1' to account for any inconsistency between Expansion 1 and Expansion 2 of the chamber which is double pulsed. The counts, scaled up to the number of frames on each of the six segments, are shown in Table 4.1, and provide an estimate of the total beam pathlength after a subtraction for attenuation of the beam owing to interactions in the chamber. A cross section may now be obtained from

$$\sigma = \frac{N}{\rho L \left(\frac{A}{M} \right)}$$

where ρ is the density of deuterium, M is the molecular weight of deuterium, A is Avagadro's number, and L is the total beam pathlength.

Table 4.1

Segment No.	Beam Track Count	Total No. Interactions	3 and 4 Prongs			5 and 6 Prongs		
			N_c	N_1	N_2	N_c	N_1	N_2
920 D	10270	1497	261	284	316	42	48	47
866 A	6182	882	167	187	183	27	33	28
806 B	9936	1648	295	311	354	40	47	49
888 C	11165	1776	285	305	354	50	51	67
889 A	7823	1270	249	310	295	44	48	51
899 A	9336	1530	314	366	378	61	72	69
Total	54712	8603	1571	1763	1880	264	299	311

$E_1 = N_c/N_2$ $\qquad$ $E_1 = 83.6\%$ $\qquad$ $E_1 = 84.9\%$

Density of Deuterium at 31^{o}K = 0.141 g/c.c.

Path length of Fiducial Region = 88 ± 3 cm

Total Beam Pathlength = $88\,[54712 - \frac{1}{2}\,8603] = 4.44 \times 10^{6}$ cm.

The estimate for the total π^+d cross section obtained from the measured total interaction rate is somewhat lower than that expected from previous experiments (49 mb compared to an expected 57 mb). This is probably owing to the value of N (= 8603) being underestimated (the physicist count was not checkscanned and small angle elastic scattering events are very hard to observe) and implies that the value of the total beam path-length, L, has been overestimated. However, the value of L will not change significantly with this small change in N (L will change by 1.5% at the most) and we have continued to use this original value. A fuller total cross section measurement, including an investigation of small angle elastic scattering, is being made at present.

The four prong cross section has been calculated from $N_1 = 1763$ and $E_1 = 83.6\%$ to be

$$\sigma \text{ four prongs} = 12.0 \pm 0.4 \text{ m b.}$$

after correction for a 6% muon contamination of the beam. This gives for reaction (1)

$$\sigma\ (\pi^+ d \rightarrow pp\ \pi^+\pi^-) = 2.10 \pm 0.17 \text{ mb}$$

after an increase of another 5% to account for those fast proton spectators which are omitted by the Part 2 scanning criteria and taking the ratio

$$\frac{\sigma\ (\pi^+ d \rightarrow pp\ \pi^+\pi^-)}{\sigma \text{ four prongs}} = 0.168 \pm 0.014$$

This ratio comes from looking in detail at four segments from the six at the final D.S.T. stage, the larger relative error in $\sigma(\pi^+ d \rightarrow pp\ \pi^+\pi^-)$ coming mostly from the small number of rolls used in this calculation. The ratio from the four rolls is in fact very similar to that found using the D.S.T. for all the data. However, the four rolls have been investigated in more detail than most of the data and this number obtained should be quite reliable. The error involved in this part of the cross section measurement is therefore slightly overestimated. The numbers in this calculation are shown in Table 4.2. The assumption inherent in this is that the proportion of reaction (1) in the four prong sample at the D.S.T. stage is the same as that originally. We have obtained no evidence to invalidate this assumption.

Having obtained the channel cross section for reaction (1), it is necessary to make a fit to the $\pi\pi$ spectrum in order to obtain the cross sections for the individual resonance production of the ρ^0 and the f^0 mesons. However, considerable care must be taken if Breit-Wigner fitting programs are to be employed.

Eisner [Ref. 16.] has described in detail difficulties which may be encountered in obtaining fractional cross sections, such as for ρ^0 production. Not only is there an overall uncertainty in the cross section of each channel in the experiment (owing to uncertainties in scanning efficiencies, beam contaminations, beam track counts etc.,) but a large error can enter through the form of parameterisation taken for the resonance in question.

Eisner has shown that the cross section for the K* (890) produced in the reaction

$$K^- p \rightarrow K^* (890) p \qquad (4)$$

Table 4.2

Segment No.	No. $\pi^+ d \rightarrow pp\pi^+\pi^-$	No. 4 Prongs
920 D	36	220
866 A	31	153
806 B	37	234
888 C	32	205
Total	136	812

or, Fraction of 4 prongs that are $pp\pi^+\pi^-$

$$= 0.168 \pm 0.014$$

using a standard Breit-Wigner width of the sort

$$\Gamma = \Gamma^{o} \left(\frac{q}{q_o}\right)^{2L+1}$$

(where q is the momentum of each meson in the K^* centre of mass and q_o is the value of q at the resonance centre), can be in error by up to 30% for $P_{beam} \sim$ 10 GeV/c owing to the large high mass tail of the Breit-Wigner.

At 4 GeV/c there is considerably less phase space available at high $\pi\pi$ mass for a similar effect to occur in the tails of the ρ^o and the f^o Breit-Wigner shapes. However, the badly parameterised tails of these resonances can seriously distort the shape of any background present and, in particular, the large tail of the ρ^o meson can greatly effect the fraction of f^o obtained in such a fit. It is evident that the parameterisation needed for the tails of resonances is not as well understood as the Breit-Wigner shapes found at resonance centres. This introduces large errors into mass fitting programs.

In a previous $\pi^+ d$ experiment at 5.1 GeV/c, J. Quinquard [Ref.17] made extensive fits to the $\pi\pi$ spectrum using different parameterisations for the Breit-Wigner shape and width. Quinquard found large variations in the fitted mass and width of the resonances together with a large uncertainty in the fitted cross section for g^o production owing to the tails of the lower mass resonances. In particular the width of the f^o was found to vary from 192 to 308 MeV/c^2 with changes in the Breit-Wigner parameterisation.

As a comparison to the 5.1 GeV/c results, several fits were made to the mass spectrum of Fig. 3.16 with the form

$$d\sigma = [\text{ Breit - Wigners + Background Polynomial}]\, d\phi$$

where $d\phi$ is the differential phase space element. Two quite different Breit-Wigner shapes were tried

$$\text{(a)} \qquad BW = \frac{(m_o \Gamma)^2}{(m^2 - m_o^2)^2 + (m_o \Gamma)^2}$$

the form recommended by Jackson [Ref. 18] for the elastic scattering of two pions via a resonance of a particular spin

$$\text{(b)} \qquad BW = \frac{m_o}{q} \qquad \frac{\Gamma}{(m^2 - m_o^2) + (m_o \Gamma)^2}$$

the form corresponding to the production of a resonance from a single vertex.

In general, the relativistic form of the width was taken as

$$\Gamma = \Gamma^o \left(\frac{q}{q_o}\right)^{2L+1}$$

The fit was tried several times, assuming slightly different spin behaviour for the ρ^o and f^o widths, and different order polynomials for the background and assuming g^o or no g^o production.

Generally speaking, a better fit and a larger width and cross section for f^o production was obtained using Breit-Wigner (b) rather than Breit-Wigner (a). The cross section for ρ^o production was found to be almost independent of the form of parameterisation. Although it is believed that most of the $\pi\pi$ spectrum results from One Pion Exchange and the elastic scattering of a π^+ and a π^- particle, we have no a priori reason to expect

Table 4.3

Fit	Breit-Wigner used	Resonances + Background	Fraction ρ^0	M_{ρ^0}	$\Gamma^0_{\rho^0}$	Fraction f^0	M_{f^0}	$\Gamma^0_{f^0}$	χ^2
1	(a)	spin 1 ρ^0 spin 2 f^0	0.593	0.762	0.134	1.186	1.257	0.116	237
2	(a)	spin 1 ρ^0 spin 2 f^0 spin 3 g^0	0.585	0.762	0.134	0.170	1.258	0.104	265
3	(b)	spin 1 ρ^0 spin 2 f^0	0.540	0.784	0.174	0.223	1.276	0.185	142
4	(b)	spin 1 ρ^0 spin 2 f^0 spin 3 g^0	0.578	0.789	0.188	0.289	1.289	0.264	113

all masses and widths in GeV/c^2

Breit-Wigner (a) to be the best fit, as no off-shell dependence is included in a simple mass fit. It must also be noted that the larger f^o width could well include many background events at the expense of the background polynomial.

The extremes of the fitting procedure are shown for four fits in Table 4.3. The results are similar to those of Quinquard. The addition of a g^o (with mass and width fixed at 1.680 and 0.160 GeV/c^2 respectively) slightly changes the shape of the background polynomial. For our comparison with other experiments we have taken the average fractions for ρ^o and f^o production as .58 and 0.25 respectively. This results in the cross sections for ρ^o and f^o charged dipion decay:-

$$(\pi^+ d \longrightarrow p\, p\, \rho^o) = 1.21 \pm 0.16 \text{ mb}$$

$$(\pi^+ d \longrightarrow p\, p\, f^o) = 0.53 \pm 0.06 \text{ mb}$$

4.3. Comparison with Other Experiments.

A problem in making comparisons between cross section measurements in different deuterium experiments centres around how to obtain the cross section for reactions with a free nucleon. Unfortunately corrections are not handled in a consistent manner by all experimenters. Among the corrections which may be made are those for:-

(a) Pauli Exclusion principle, when there are two identical nucleons in the outgoing channel

(b) Scanning biases resulting in a drop in the differential cross section at low momentum transfer

(c) Effect of selection of slower nucleon as the spectator on momentum transfer distributions.

(d) High momentum tail of the spectator nucleon using as a correction factor the experimental spectator distribution or a wave function model.

(e) Glauber effect; the screening of one nucleon by the other which in effect reduces the effective flux.

We have shown in a previous chapter how effects (a), (b) and (c) can seriously distort the differential cross section. However, their combined reduction of the total cross section is only a few per cent.

Glauber [Ref. 19.] explained how the total deuterium cross section could be reduced below the expected sum of the cross sections on the free nucleons (at our energy the cross section defect is about 2.5% of the total $\pi^+ d$ cross section) using the theoretical expression

$$\sigma_D = \sigma_p + \sigma_n - \sigma_p \cdot \sigma_n / 4\pi \langle r^2 \rangle$$

where r is the distance between the centres of the two nucleons. This expression can be derived by considering the nucleons as black spheres with geometrical cross sections equal to one half the total cross section. The difference between the above simple form and the more complicated form suggested by Wilkin [Ref. 20]. which satisfies charge independence is negligible in our case.

It seems that exactly how, and to what extent corrections should be made is not entirely understood. One method for assessment of the magnitude of the total correction is, of course, the measurement of the same process in both deuterium and hydrogen. Since in this report we are primarily interested in aspects of reaction (1) we shall compare results from this experiment with others at various energies. A compilation of $\pi^+ d$ and $\pi^- p$ experiments are given in the review by Musgrave [Ref. 12.]

The cross sections for

$$\pi^+ d \rightarrow p_s\, p\, \pi^+ \pi^- \qquad (1)$$

and

$$\pi^- p \longrightarrow n\, \pi^+ \pi^- \qquad (5)$$

are equal by charge symmetry. The data are compared in Fig. 4.1 and the π^+ data are seen to fall systematically below the π^- cross sections by 15 to 25%. Usually the $\pi^- p$ reaction is less well constrained than the $\pi^+ d$ reaction, and the $\pi^- p$ cross sections could include some background. However, no corrections are made to the π^+ data for the Pauli effect nor is the high momentum spectator tail included, except in the 5.1 GeV/c case. Also, several of the $\pi^+ d$ experiments only use events where the proton spectator is observed (i.e. only four prong events) and make the large correction for the remainder on the basis of the Hulthen distribution, We can expect these effects to account for a large part of the observed discrepancy.

The cross section measurement from this experiment, which includes high momentum spectator events but not a correction for the Pauli effect, is seen to be consistent with other $\pi^+ d$ experiments and somewhat below the $\pi^- p$ value. The experiment by Eisner et al [Ref.15.] at 4.1 GeV/c gives 2.85 ± 0.07 mb for reaction (5) compared to our 2.10 ± 0.17 mb for reaction (1). The $\pi^- p$ result, however, can be seen

Fig. 4.1. (a) Cross sections for $\pi^+ d \rightarrow \pi^+ \pi^- pp_s$ (b) Comparison of channel cross-sections for $\pi^+ d \rightarrow \pi^+ \pi^- pp_s$ and $\pi^- p \rightarrow \pi^+ \pi^- n$.

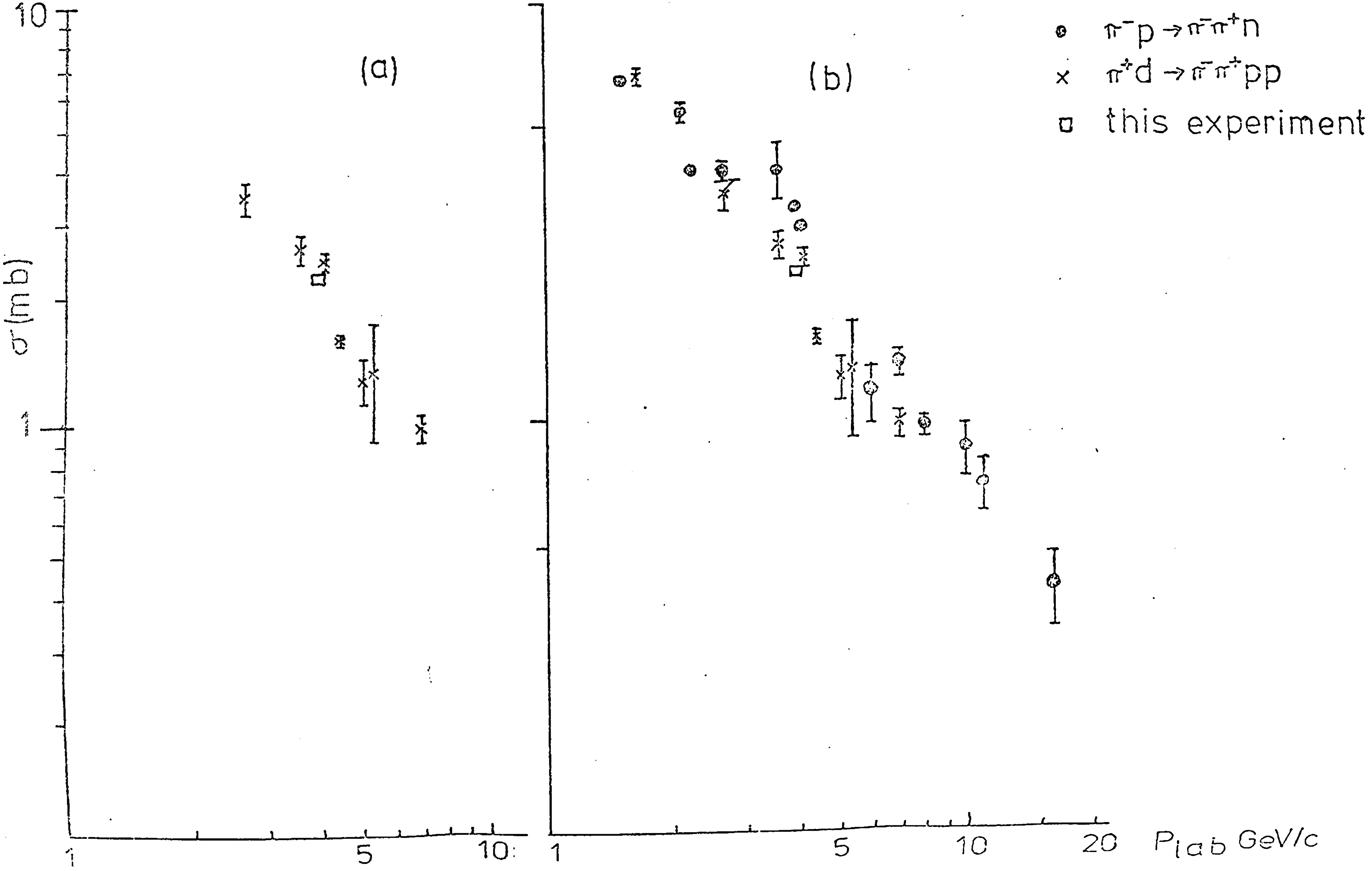
10
1
σ (mb)
(a)
(b)
1
5
10
1
5
10
20
P lab GeV/c
π⁻p → π⁻π⁺n
π⁺d → π⁻π⁺pp
this experiment

to be slightly high when compared to the values at other energies.

The ρ^o production cross sections for reactions (1) and (5) are actually in better agreement, as shown in Fig. 4.2. In this case the Exclusion Principle correction has generally been made in the quoted cross section, otherwise a 4% (pure spin flip) correction has been applied. This much better agreement suggests that a large part of the discrepancy between the channel total cross sections should be attributed to background in the π^-p reaction. Our value for ρ^o production (after the 4% correction) of 1.26 ± 0.16 m b compares well with the π^-p value of 1.15 ± 0.05 m b found by Eisner et al.

The charge symmetric f^o cross sections provide a less stringent check of the deuterium data than is possible for the ρ^o, since the errors are much larger. The agreement in Fig. 4.3. is good, apart from the 4.5. GeV/c π^+d result. Our estimated value for f^o production is 0.53 ± 0.06 mb, equal to the π^-p value (also 0.53 ± 0.06 mb).

A further check involves comparison of the differential cross section and decay density matrix elements for the charge symmetric ρ^o reactions. Again we compare our data with the Eisner et al π^-p experiment. The differential cross sections for the two experiments are shown in Fig. 4.4. and the Jackson frame (t - channel) decay matrix elements for the ρ^o for the π^-p experiment we show in Fig. 4.5. These may be compared with the π^+d matrix elements shown in Fig. 5.4 (b).
We have the result that the physics of the two reactions, apart from the cross sections, are very similar except in the very forward region of

momentum transfer where corrections have to be made.

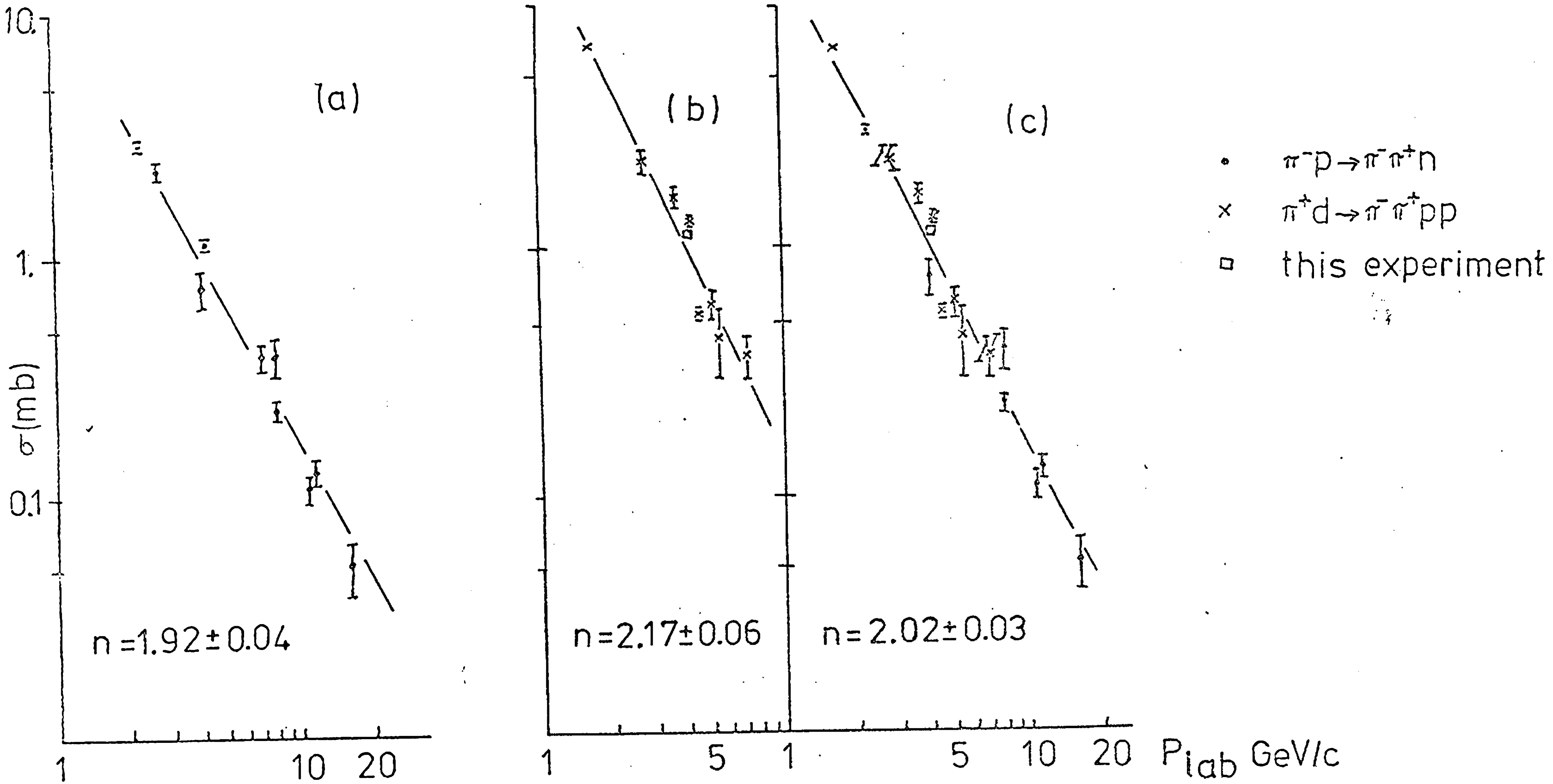

Fig. 4.2. Channel cross sections for $\pi^+ d \rightarrow \rho^0 pp_s$ and $\pi^- p \rightarrow \rho^0 n$. (a) Shows $\pi^- p \rightarrow \rho^0 n$; (b) $\pi^+ n \rightarrow \rho^0 p$ and (c) both of them. The marked values of n are found from fitting the data in each graph to the form Ap^{-n}_{lab}.

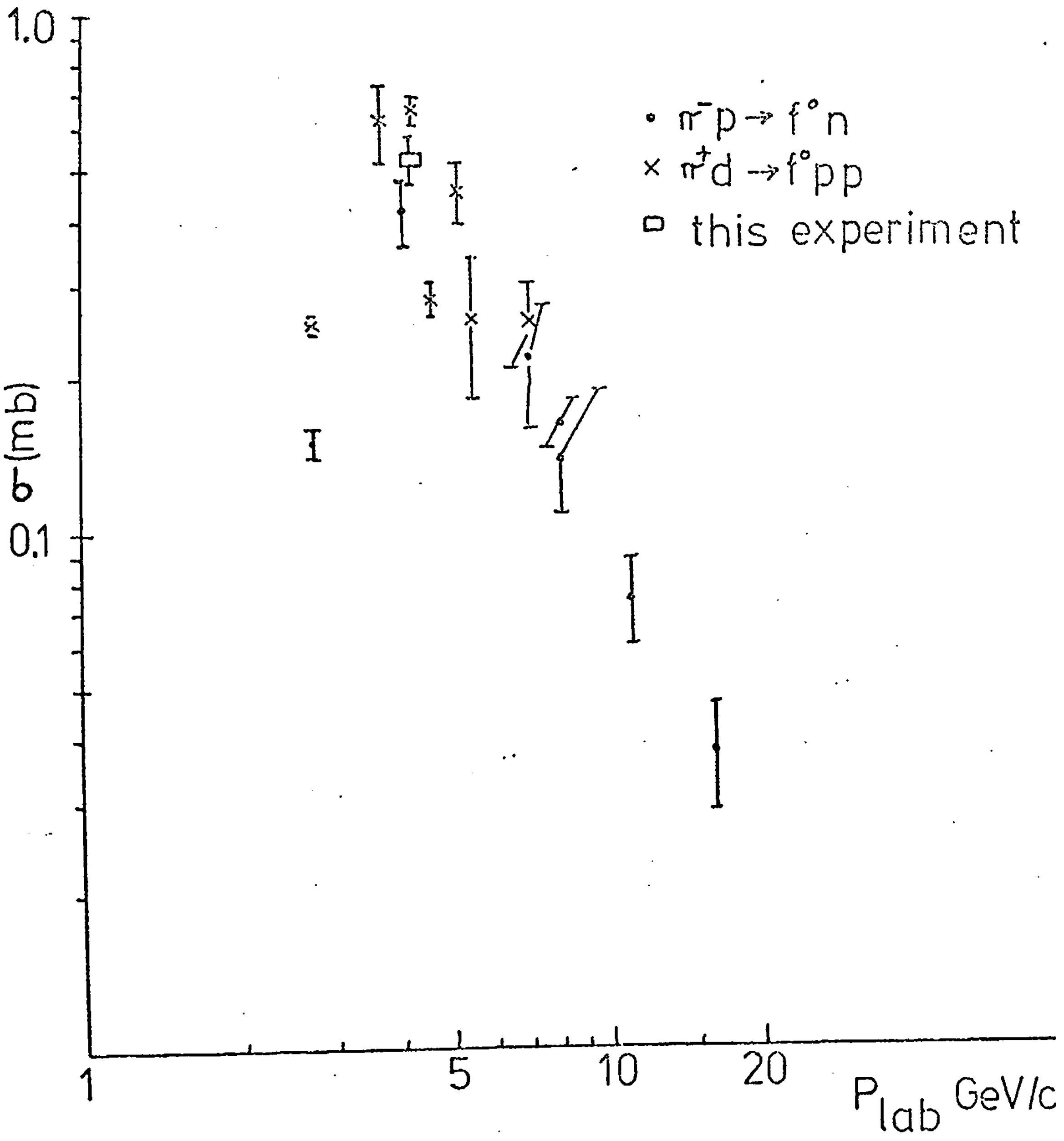

Fig. 4.3. Channel cross sections for $\pi^+ n \rightarrow pf^0$ and $\pi^- p \rightarrow f^0 n$

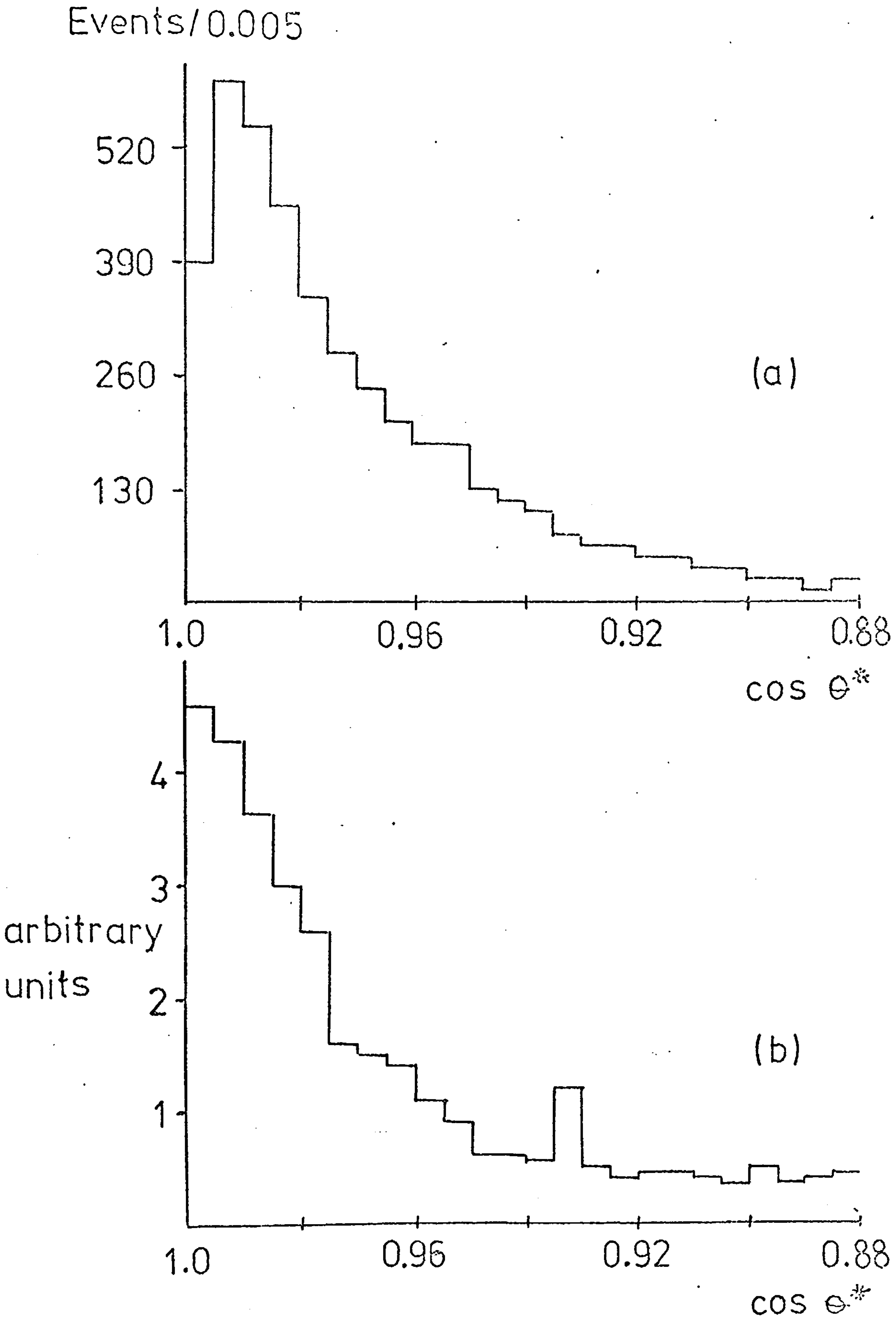

Fig. 4.4. Differential Cross Sections for the ρ^0

(a) This Experiment 4 GeV/c $\pi^+ d$

(b) Eisner et al 4.1 GeV/c $\pi^- p$

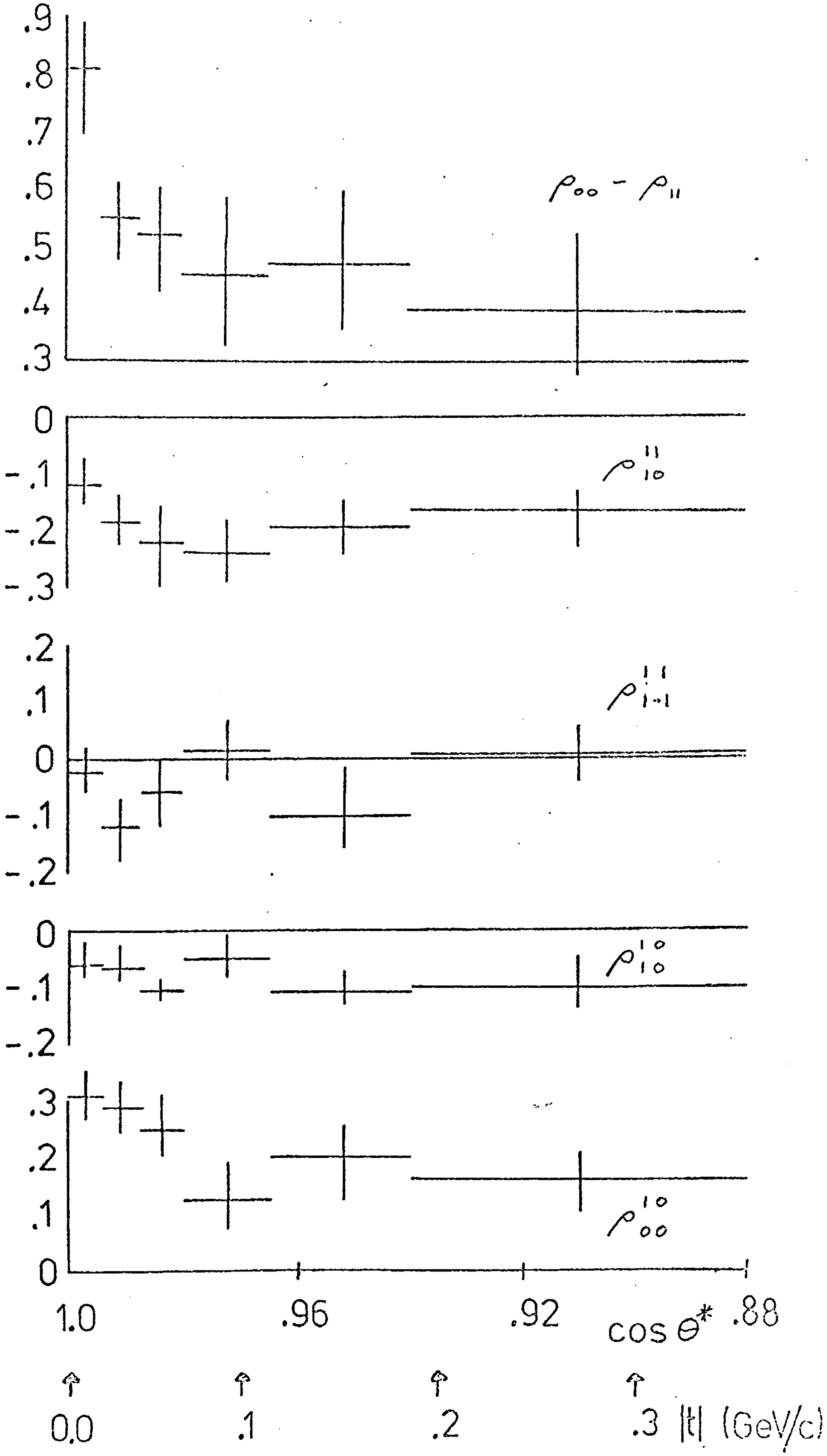

Fig. 4.5. ρ^0 Density Matrix elements for the 4.1 GeV/c $\pi^- p$ Eisner et al Experiment

CHAPTER 5

Analysis of ρ^o Production

The Chew-Low formula [Ref. 21]. was the first attempt to describe the off-shell behaviour of a One Pion Exchange type reaction amplitude in terms of the on-shell pion-pion interaction. By performing extrapolations to the pion pole in various ways, it has since proved possible to extract from the data information on pion-pion phase shifts.

However, with the recent increase in data of the $\pi^- p \rightarrow \pi^- \pi^+ n$ and $\pi^+ n \rightarrow \pi^+ \pi^- p$ channels, we are able to observe other processes which contribute in addition to straightforward One Pion Exchange. From the coefficients of the decay angular distribution of the dipion system in the rho region, it is possible to extract the dominant pion exchange amplitudes and extrapolate them to the pion pole. In addition, the form of the remaining amplitudes, coming from absorption or from other exchange mechanisms, can be investigated. By repeating the analysis at several energies we obtain the energy dependence of these other mechanisms, from which can be deduced the dominant particle exchange or production process involved in each amplitude.

5.1. Classical One Pion Exchange.

As a guide to the Amplitude Analysis which follows, we present here a summary of the characteristics of simple One Pion Exchange. The reader is referred to the several excellent reviews on the subject, notably those of Ref. 22.

Suppose that the reaction

$$\pi^+ n \longrightarrow \pi^+ \pi^- p \qquad (1)$$

were completely dominated by One Pion Exchange [Fig. 5.1], then the differential cross section is given by the Chew-Low formula:-

$$\frac{d^3\sigma}{d\,|t|\,dm\,d\Omega} = A \, \frac{-t}{(t - \mu^2)^2} \, \frac{d\sigma_{\pi\pi}}{d\Omega}$$

where A contains the normalisation together with the flux and any off-shell form factors. The variable 'm' describes the mass of the dipion system, 't' the four momentum transfer squared from the beam to the dipion system, and $d\sigma/d\Omega$ the decay angular distribution of the outgoing π^+ in the dipion system. The on-shell decay angular distribution is given by $d\sigma_{\pi\pi}/d\Omega$. The factor "-t" arises because the pion exchange flips the nucleon spin, leading to the designation "Half Asleep Pion Exchange" [Ref. 22(Fox)].

The $\pi\pi$ partial waves are obtained from the on-shell $\pi\pi$ differential cross section:-

$$\frac{d\sigma_{\pi\pi}}{d\Omega} = \left| \frac{1}{q} \sum_L (2L+1) f_L P_L(\cos\theta) \right|^2$$

with the isospin decomposition

$$f_L = \frac{2}{3} f_L^{I=0} + \frac{1}{3} f_L^{I=2} \qquad \text{for even } L$$

$$f_L = f_L^{I=1} \qquad \text{for odd } L$$

and, in the $\pi\pi$ elastic scattering region

$$f_L^I = \sin\delta_L^I \, \exp(i\,\delta_L^I)$$

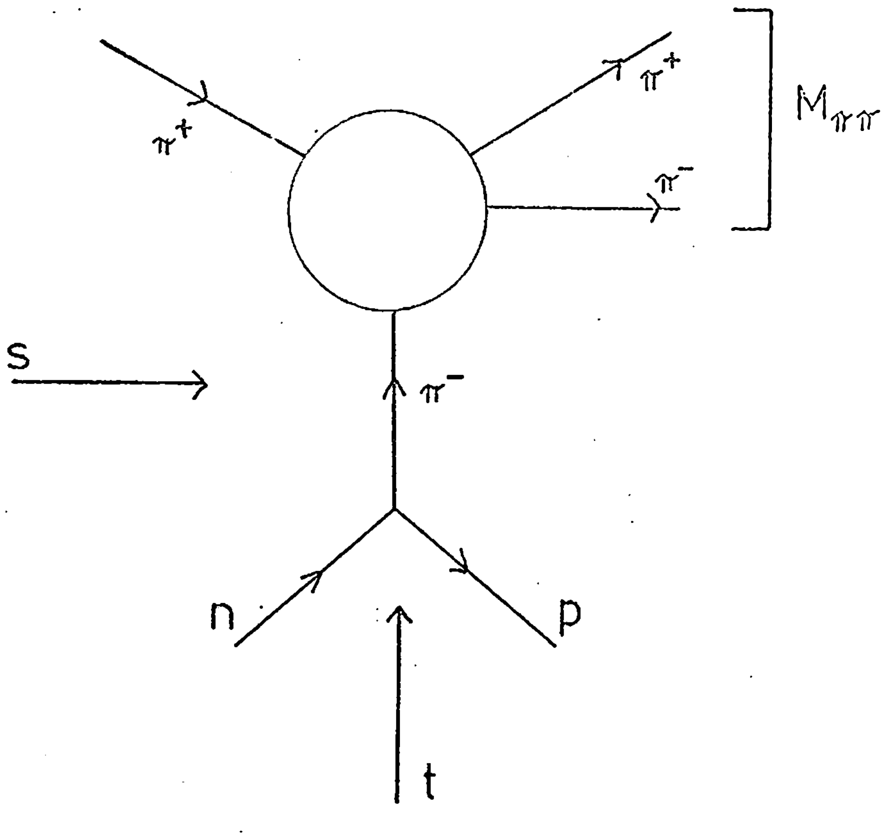

Fig. 5.1. π Exchange in $\pi^+ n \rightarrow \pi^+\pi^- p$

By integrating over the decay angles of the ππ system the double differential cross section, $d^2\sigma/d|t|\,dm$ is obtained with which a fit can be made to the data. Such a fit is described in Appendix 1.

The decay angular distribution of the ππ system is analysed in terms of spherical harmonic moments

$$W(\theta,\phi) = \sum_{L\,m} \langle Y^{L}_{m} \rangle \, Y^{L}_{m}(\theta,\phi)$$

The coordinate system used is defined in the following way for two alternative systems. The suitability of either system for each particular analysis will be described in later sections:-

(a) in the s - channel helicity frame the coordinate system lies in the dipion centre of mass with the z direction the dipion direction in the reaction centre of mass.

(b) in the t - channel helicity frame (the Gottfried-Jackson frame) the coordinate system lies in the dipion centre of mass with the z direction the beam direction in the dipion centre of mass.

(c) the y direction in both frames is defined by the vector (beam) x (dipion) and the decay angle is described in these systems by the outgoing π^+.

π exchange produces only t - channel (i.e. Gottfried-Jackson) helicity zero $\pi^+\pi^-$ systems, and then only the $\langle Y^L_0 \rangle$ moments of the decay angular distribution are non-zero. Expressing these moments in terms of $\pi^+ n \rightarrow \pi^+\pi^- p$ amplitudes for the production of S_0, P_0,..., waves (i.e. spin 0, 1, ...) helicity zero $\pi^+\pi^-$ states, we obtain the following system of equations

$$\sqrt{4\pi}\; N \langle Y_0^0 \rangle = |S_0|^2 + |P_0|^2 + |D_0|^2 \qquad 1(a)$$

$$\sqrt{4\pi}\; N \langle Y_0^1 \rangle = 2\, \mathrm{Re}\,(S_0 P_0^*) + \frac{4}{\sqrt{5}}\, \mathrm{Re}\,(P_0 D_0^*) \qquad 1(b)$$

$$\sqrt{4\pi}\; N \langle Y_0^2 \rangle = \frac{2}{\sqrt{5}}\, |P_0|^2 + 2\, \mathrm{Re}\,(S_0 D_0^*) + \frac{\sqrt{20}}{7}\, |D_0|^2 \qquad 1(c)$$

$$\sqrt{4\pi}\; N \langle Y_0^3 \rangle = \sqrt{\frac{108}{35}}\; \mathrm{Re}\,(P_0 D_0^*) \qquad 1(d)$$

$$\sqrt{4\pi}\; N \langle Y_0^4 \rangle = \frac{6}{7}\, |D_0|^2 \qquad 1(e)$$

With one or two assumptions this system forms a soluble set of equations for the amplitudes S_o, P_o etc..

Combining these amplitudes with the Chew-Low equation we obtain

$$L_o = \frac{\sqrt{-t}}{(t-\mu^2)}\; F(t)\; \frac{M_{\pi\pi}}{\sqrt{q}}\; \sqrt{2L+1}\; f_L$$

for each partial wave L. F (t) is the off-shell form factor at the ππ vertex.

It is important, however, to realise the form of a set of equations linking the observable quantities, the spherical harmonic moments, to (in this case, model dependent) amplitudes of the production process.

This particular set of equations has been given as it describes the most simple such set. In the following analysis we shall describe a similar set of equations. However, this new set will be written in a general way, including helicity non-zero moments and amplitudes, and will not be confined only to the t-channel helicity zero predictions of One Pion Exchange. The next section will confirm that such a procedure is necessary.

5.2. Comparison of Simple One Pion Exchange with data.

In Fig. 5.2. is shown the mass spectrum of the unnormalised t-channel spherical harmonic moments integrated over the interval $0 < t < -0.15$ $(\mathrm{GeV}/c)^2$ obtained in the $\pi^- p \rightarrow \pi^- \pi^+ n$ C.E.R.N - Munich experiment at 17.2 GeV/c [Ref. 23]. From the excellent statistics in this experiment a number of features concerning $\pi^+ \pi^-$ scattering can be observed clearly.

(a) the presence of the $\rho(770)$, f (1260) and g(1700) mesons with spins 1, 2 and 3 respectively. To establish spin 3 for the g requires the additional knowledge that L = 7 and higher moments are small near 1700 MeV/c^2.

(b) a large $\langle Y^1_o \rangle$ moment in the rho region. From small $\langle Y^3_o \rangle$ and $\langle Y^4_o \rangle$ moments in this region it is evident that spin 2 waves are unimportant. The large $\langle Y^1_o \rangle$ moment therefore comes from an S wave interfering with the P wave rho meson.

(c) sharp structure in $\langle Y^1_o \rangle$ near $M_{\pi\pi} = 1\ \mathrm{GeV}/c^2$. This has been

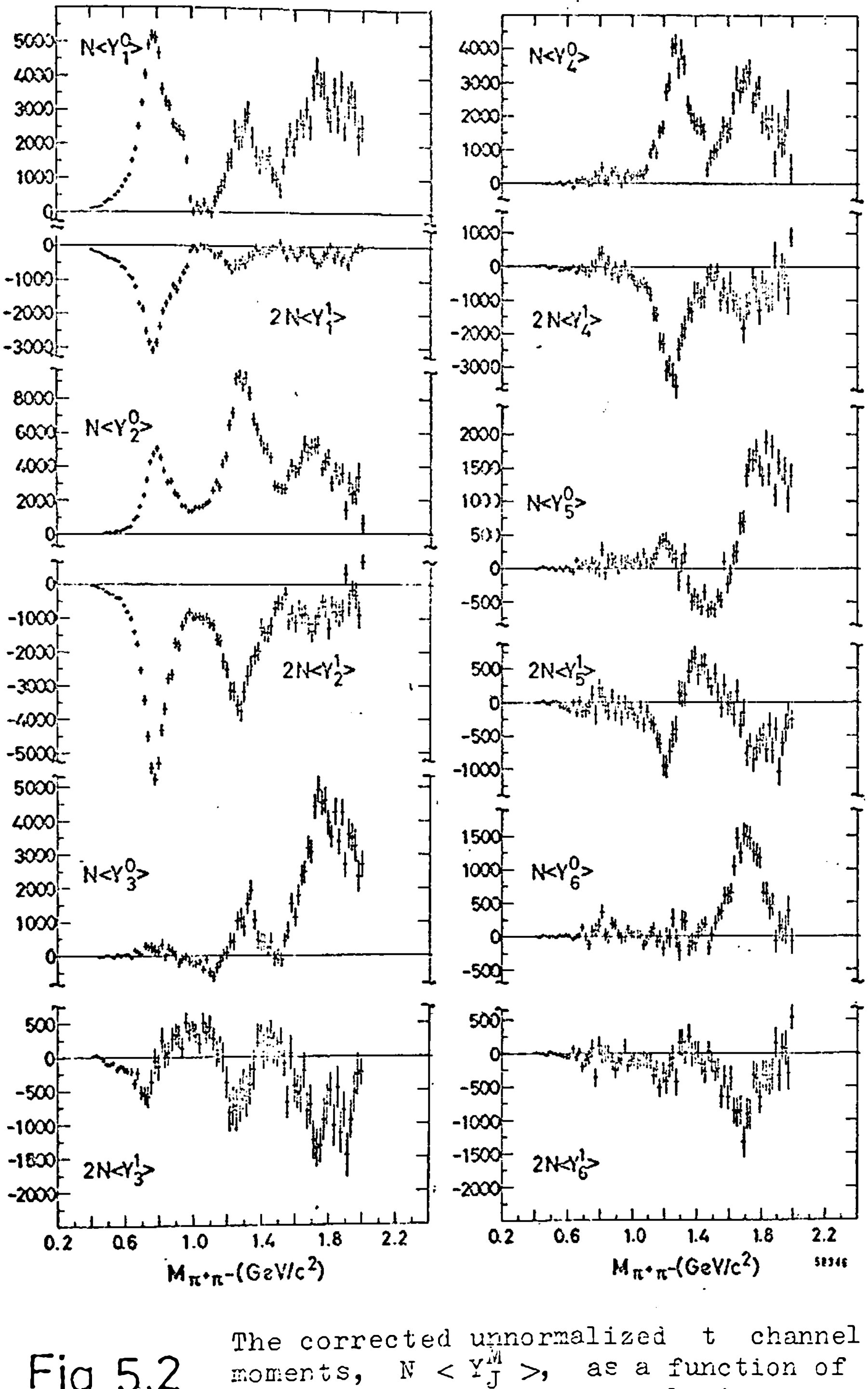

Fig. 5.2

The corrected unnormalized t channel moments, $N < Y_J^M >$, as a function of $\pi^+\pi^-$ mass for the interval $0 < -t <$ < 0.15 GeV^2, taken from Ref. 34. A factor of 2 should be included in the $M \neq 0$ moments shown in Ref. 22.

the subject of much study in recent years. The reader is referred to explanations of this effect in terms of "Odorico Zeroes" [Ref. 24] or, more recently, the existence of a narrow resonance, the S^* [Ref. 25].

(d) large $\langle Y^L_1 \rangle$ moments throughout the entire $\pi\pi$ spectrum. From these we observe the non-negligible presence of helicity one $\pi^+\pi^-$ production.

From these experimentally determined moments we see that the data can not be assumed to be pure π exchange. In particular, the sizeable $\langle Y^L_1 \rangle$ moments of Fig. 5.2. point to other exchange mechanisms being present. These include A_2 exchange or absorptive corrections both of which require different amplitudes being added to equations 1 (a) to (e). In particular, factors which include the dependence of the amplitudes on nucleon spin would almost certainly be required.

To allow for these other exchanges, we perform an amplitude analysis through the rho region as a function of $|t|$. Although an assumption is inherent in this amplitude analysis, the procedure is as near model-independent as is possible at this stage.

5.3. Experimental Description of the Decay Angular Distribution - the Jacob and Wick Notation.

A system containing states of several different spin-parities can be described by a compound density matrix in every way analogous to the simple density matrix of unique spin-parity. The density matrix is written $\rho^{LL'}_{\mu\mu'}$ where the elements with $L \neq L'$ and $\mu \neq \mu'$

describe interference between production of the states $|L\,\mu\rangle$ and $|L'\,\mu'\rangle$, and the diagonal element $\rho^{LL}_{\mu\mu}$ is the probability for production of the state $|L\,\mu\rangle$. The usual properties of hermiticity, positivity and the constraints of parity conservation still apply.

The angular distribution of the decay of the mixed system into two zero spin particles is given by:-

$$W(\theta,\phi) = \sum_{\substack{L L' \\ \mu \mu'}} \rho^{LL'}_{\mu\mu'}\, Y^{L}_{\mu}(\theta,\phi)\, Y^{L'\,*}_{\mu'}(\theta,\phi)$$

We may also expand the decay angular distribution as a series of spherical harmonics:-

$$W(\theta,\phi) = \sum_{L\mu} \langle Y^{L}_{\mu} \rangle\, Y^{L}_{\mu}(\theta,\phi)$$

where the maximum value of L in this expansion equals twice the maximum angular momentum, L_{MAX}, in the two particle system.

As parity is conserved in the decay, only the real parts of the $\langle Y^{L}_{\mu} \rangle$ and the $\rho^{LL'}_{\mu\mu'}$ factors enter into the angular distribution. By writing $\rho^{LL'}_{\mu\mu'}$ we shall infer always the real part.

Consider now a third expansion of the decay angular distribution, in Jacob and Wick notoation:-

$$W(\theta,\phi) = \left| \sum_{L\mu} H^{L\mu}\, Y^{L}_{\mu}(\theta,\phi) \right|^{2}$$

where we now include a possible dependence on the final and initial nucleon helicity states λ and λ'. (Note, a priori we are saying nothing about this dependence)

$$W(\theta,\phi) = \sum_{\lambda\lambda'} \left| \sum_{L\mu} H^{L\mu}_{\lambda\lambda'} \, Y^{L}_{\mu}(\theta,\phi) \right|^2$$

The $H^{L\mu}_{\lambda\lambda'}$ are the Spin Dependent Coefficients of the decay angular distribution and are the amplitudes of Amplitude Analysis.

We note their parity restrictions:-

$$H^{L\,-\mu}_{-\lambda\,-\lambda'} = (-1)^{\mu+\lambda+\lambda'} \, H^{L\mu}_{\lambda\lambda'}$$

and the convenience of combining them into

$$L^{\mu\pm}_{\lambda\lambda'} = \frac{1}{\sqrt{2}} \left(H^{L\mu}_{\lambda\lambda'} \mp (-1)^{\mu} H^{L\,-\mu}_{\lambda\lambda'} \right)$$

where, as $s \to \infty$, $L^{\mu +}_{\lambda\lambda'}$ and $L^{\mu -}_{\lambda\lambda'}$ describe the production of a $\pi\pi$ system of spin L, helicity modulus μ by natural and unnatural parity exchange respectively.

We see that we have three parallel descriptions of the decay angular distribution. The spherical harmonic moment description and the density matrix description are, in fact, equivalent, and each moment may be expanded as a linear sum of density matrix elements. The spherical harmonic moments are also the quantities which are directly observable in the data.

The amplitudes $H^{L\mu}_{\lambda\lambda'}$ are, however, not linearly related to the spherical harmonic moments, and must be solved for by a set of simultaneous equations, similar to equations 1 (a) to (e). The amplitudes are the quantities in which we are interested, and which we believe contain the best physical description of the production process. It is the purpose of further sections to determine these amplitudes.

5.4. Amplitude Analysis in the Rho Region.

The Amplitude Analysis described in this section follows that of Estabrooks and Martin [Ref. 26].

In the following analysis we shall work in the s-channel (i. e. Helicity Frame). The observables in the one frame can be obtained in the other by the transformation.

$$\langle Y_{\mu}^{L} \rangle^{s} = \sum_{\mu'} d_{\mu'\mu}^{L}(\omega) \langle Y_{\mu'}^{L} \rangle^{t}$$

and where the crossing angle'ω' in the high s, low t limit is given by

$$\cos\omega \approx \frac{M_{\pi\pi}^{2} + t}{M_{\pi\pi}^{2} - t} , \qquad \sin\omega \approx \frac{2\sqrt{-t}}{M_{\pi\pi}}$$

If we wish to isolate the One Pion Exchange part of the reaction then we obviously require the amplitudes equivalent to the S_0, P_0... of equations 1(a) to (e), extrapolated to the pion pole. Now this analysis can be done equally well with either s or t - channel moments. However, it is reasonable to assume that any (s-channel) absorption effects will be smoother and simpler in the s-channel itself rather than in the crossed system where the effect of crossing could complicate the absorption effects even more. It must be remembered that absorption is still only a little understood effect.

It is assumed that reaction (1) takes place with the exchange of a virtual particle as described in Fig. 5.1 for virtual π exchange. There are three sets of quantum numbers which can be carried by this exchanged particle, corresponding to the π ($J^P = 0^-$), A_1 (1^+) and A_2 (2^+) mesons.

By considering Parity conservation and G-Parity conservation at the t-channel nucleon and meson vertices, we can make the following observations about the exchanged particle:-

(a) π exchange contributes only to t-channel nucleon helicity non-flip, and therefore contributes mostly to s-channel nucleon helicity flip. The s-channel flip is not total owing to the finite crossing angle between the t and the s-channel.

(b) A_1 exchange contributes only to t-channel nucleon helicity flip and therefore mostly to s-channel helicity non-flip.

(c) A_2 exchange contributes both to flip and non-flip amplitudes.

(d) A_2 (natural parity) exchange contributes only to dipion helicity ± 1 states.

(e) A_2 exchange cannot couple to S wave ($J^P = 0^+$) dipion production.

We make in this analysis the assumption that there is no exchange with the quantum numbers of the A_1. This is the only input model dependence, and is necessary if the number of parameters in the analysis is to remain equal to six, the number of observed density matrix element combinations. Otherwise we have eight parameters in our set of equations; namely the eight amplitudes comprising the three helicity states for spin 1 dipion production and the one helicity state for spin 0 dipion production, all for spin flip and spin non-flip of the reaction nucleon helicity. With a polarised target in the $\pi^- p \rightarrow \pi^- \pi^+ n$ channel, the amount of A_1 exchange can be measured from the size of the π - A_1 interference term in the unnatural parity exchange polarisation data. A start has been made by Sonderegger and Bonamy who reported at the Lund Conference, 1969 [Ref. 27] in the reaction.

$$\pi^- p \quad (\uparrow) \longrightarrow \pi^o \pi^o n$$

a considerable assymmetry indicative of A_1 exchange. However, as yet no reliable information has been obtained for the reaction

$$\pi^- p \quad (\uparrow) \longrightarrow \pi^- \pi^+ n$$

It is to be hoped that such an experiment could be made in the near future.

Quantitatively, the assumption of no A_1 exchange allows us to write

$$H^{00}_{++} = H^{00}_{--} = H^{10}_{++} = H^{10}_{--} = 0$$

and $\left| H^{11}_{++} - H^{11}_{--} \right| = 0$ from the A_1 term L^{1-}_{++} and the Parity condition.

It is now possible to write a set of equations for the remaining amplitudes $H^{L\mu}_{\lambda\lambda'}$ in a similar way to equations 1 (a) to (e). This set of equations is shown below:-

$$\sigma \equiv \frac{d\sigma}{dt} = |M_s|^2 + |M_o|^2 + |M_+|^2 + |M_-|^2 \qquad 2(a)$$

$$(\rho^{11}_{00} - \rho^{11}_{11})\sigma = |M_o|^2 - \frac{1}{2}\left(|M_+|^2 + |M_-|^2\right) \qquad 2(b)$$

$$\rho^{11}_{1-1}\,\sigma = \frac{1}{2}\left(|M_+|^2 - |M_-|^2\right) \qquad 2(c)$$

$$\rho^{11}_{10}\,\sigma = \frac{1}{\sqrt{2}}\,|M_-|\,|M_0|\,\cos\theta^{11}_{10} \tag{2(d)}$$

$$\rho^{10}_{00}\,\sigma = |M_0|\,|M_s|\,\cos\theta^{10}_{00} \tag{2(e)}$$

$$\rho^{10}_{10}\,\sigma = \frac{1}{\sqrt{2}}\,|M_-|\,|M_s|\,\cos\left(\theta^{11}_{10} - \theta^{10}_{00}\right) \tag{2(f)}$$

The following change of notation has been made to simplify further discussion:-

$$M_0 = H^{10}_{+-} \qquad M_s = H^{00}_{+-}$$

$$M_- = \frac{1}{\sqrt{2}}\left(H^{11}_{+-} + H^{11}_{-+}\right)$$

$$|M_+|^2 = \frac{1}{2}\left|H^{11}_{++} + H^{11}_{--}\right|^2 + \frac{1}{2}\left|H^{11}_{+-} - H^{11}_{-+}\right|^2$$

$$\theta^{11}_{10} = \arg M_- - \arg M_0 \quad , \quad \theta^{10}_{00} = \arg M_s - \arg M_0$$

When the centre-of-mass-energy ($\sqrt{s}$) tends to infinity, M - and M + are the $|\mu|$ = 1 unnatural and natural parity exchange amplitudes respectively. It should be noted that the natural parity exchange amplitude only occurs in the form $|M+|^2$. It follows that it is only the phases between unnatural parity exchanges which are in fact measurable.

Equations 2(a) to (f) describe the system of 6 equations with 6 unknown quantities. The system is not a linear one and has to be solved numerically. Owing to the form of the data there are two possible solutions apart from trigonometric ambiguities. Because the angles cannot be found to within a sign, the angle θ^{11}_{10} was determined assuming sin θ^{11}_{10} was positive. The values to be shown for θ^{10}_{00} correspond to this choice. In addition, a small non-flip factor for helicity zero production was included

$$H^{L0}_{++} = r\, H^{L0}_{+-} \qquad r = \sqrt{t_{MIN}/t'}$$

where $t = t_{MIN}$ is the forward direction and $t' = t - t_{MIN}$. This arises because the non-flip t - channel π exchange behaviour does not cross completely into total s-channel flip behaviour if the crossing angle is finite. It is important to realise that the small H^{L0}_{++} comes from π exchange and crossing and not A_1 exchange which we have discarded. The magnitude of this effect may be seen in Appendix 3. This non-flip contribution is usually neglected but for very small $|t|$ can be appreciable, even at 17 GeV/c. As the 4 GeV/c data is presented for about t = -0.02 $(GeV/c)^2$ onwards only, and as t_{MIN} in the rho region is about - 0.005 $(GeV/c)^2$, this correction factor is very small. However, to take account of this contribution we have multiplied $|M_o|$ and $|M_s|$ in equations 2(a) 2(b) and 2(e), by $\sqrt{1 + r^2}$ before solving the set of equations. The numerical solution of these equations is described in Appendix 2.

It is important to realise that all the available information on ρ^o production is contained within the five density matrix elements and the differential cross section, and that this analysis does not per se add anything new. However, it does rearrange the data into a form which is both easier to compare with theoretical models and which shows more clearly the strength of each production process.

5.5. Experimental Data and Analysis.

The data used in this analysis contained 5279 events corresponding to the reaction

$$\pi^+ n \rightarrow \rho^0 \quad p$$

using the mass interval.

$$0.68 < M_{\pi\pi} < 0.88 \quad \text{GeV}/c^2$$

The decay angular distribution in the s-channel frame for events in the ρ^0 region, and the momentum transfer distribution in production are shown in Figs. 5.3.(a) and (b). Analysing the decay angular distribution in terms of spherical harmonic moments.

$$W(\theta, \phi) = \sum_{L\mu} \langle Y^L_\mu \rangle \; Y^L_\mu(\theta, \phi)$$

we find that moments with $L > 2$ can be neglected in the ρ^0 mass region.

The spherical harmonic coefficients $\langle Y^L_\mu \rangle$ for $L \leqslant 2$ are shown as a function of momentum transfer in Tables 5.1 (a) (in the s-channel helicity frame) and (b) (in the t-channel helicity frame). The same data is presented graphically in Figs. 5.4. (a) (s-channel) and (b) (t-channel), where can be seen the variation with momentum transfer of the six independent combinations of the density matrix elements for a mixed J = 0,1 system, which can be determined from the $\langle Y^L_\mu \rangle$ coefficients.

At low momentum transfer, $|t|$, there is in some cases an ambiguity in the choice of reaction proton, if both final state protons have low momentum. We have found that there is a negligible change in the magnitude of the moments for each choice of proton. Despite this, the

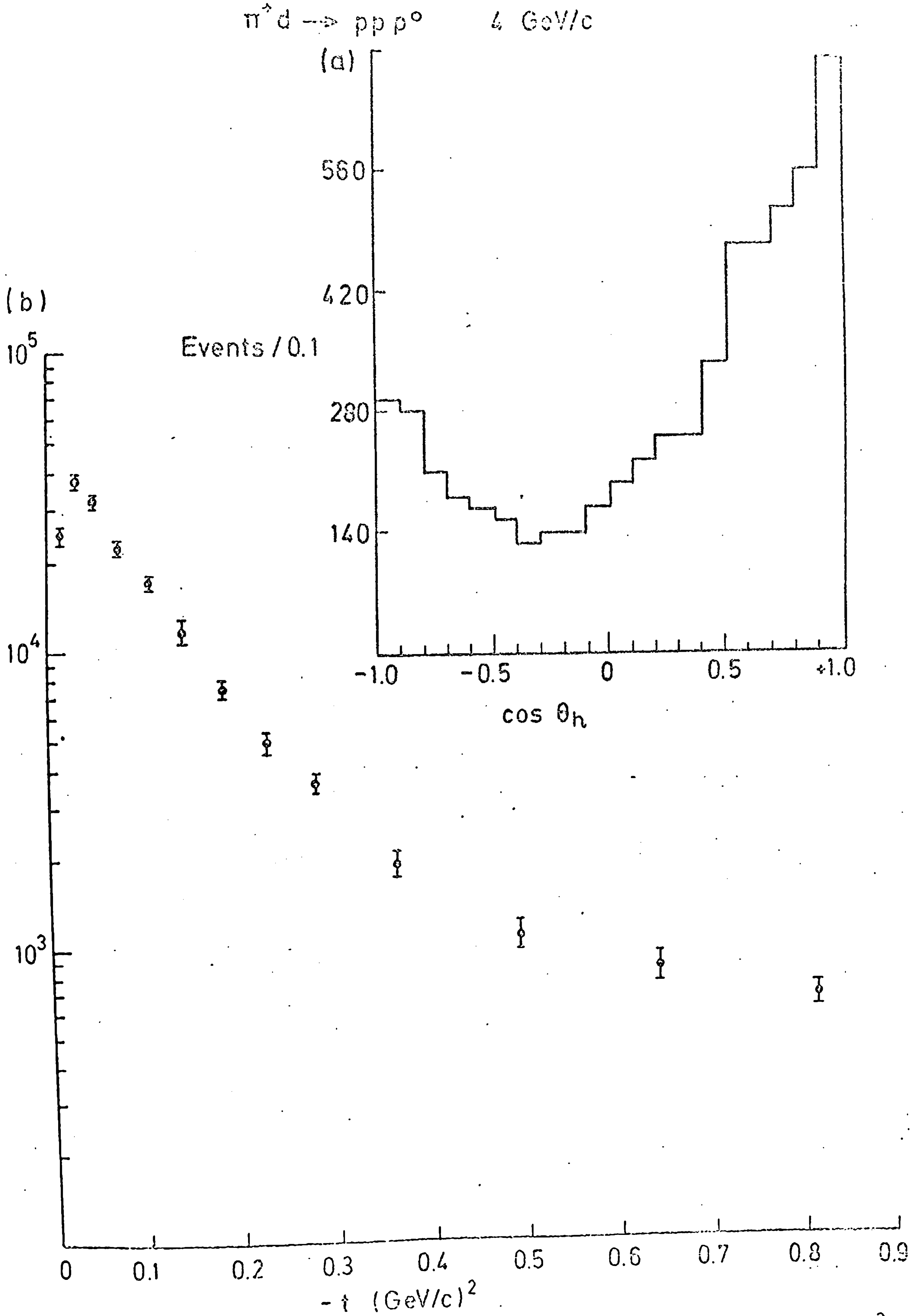

Fig. 5. 3. Differential Cross Section for ρ^0 production in Events / $(\mathrm{GeV}/c)^2$

Table 5.1

Spherical harmonic coefficients $\langle Y^L_\mu \rangle$ for ρ^0 decay as a function of momentum transfer.

a) s-channel moments

-t (GeV/c)^2	Y_0^1	Y_1^1	Y_0^2	Y_1^2	Y_2^2
t_{min}-0.02	0.164 ±0.021	0.008 ±0.010	0.184 ±0.020	0.009 ±0.013	0.009 ±0.009
0.02-0.04	0.151 ±0.013	0.009 ±0.006	0.183 ±0.012	0.021 ±0.008	-0.004 ±0.005
0.04-0.06	0.151 ±0.013	0.021 ±0.006	0.168 ±0.013	0.042 ±0.008	-0.005 ±0.006
0.06-0.08	0.134 ±0.015	0.035 ±0.008	0.150 ±0.014	0.062 ±0.010	0.003 ±0.007
0.08-0.10	0.126 ±0.017	0.042 ±0.009	0.134 ±0.016	0.076 ±0.011	0.009 ±0.008
0.10-0.15	0.134 ±0.012	0.046 ±0.007	0.103 ±0.011	0.104 ±0.008	0.011 ±0.006
0.15-0.20	0.118 ±0.015	0.060 ±0.010	0.069 ±0.014	0.110 ±0.011	0.021 ±0.009
0.20-0.25	0.078 ±0.019	0.059 ±0.013	0.042 ±0.017	0.139 ±0.014	0.059 ±0.012
0.25-0.30	0.060 ±0.021	0.035 ±0.016	0.004 ±0.021	0.097 ±0.016	0.048 ±0.015
0.30-0.40	0.080 ±0.018	0.072 ±0.016	-0.056 ±0.017	0.095 ±0.015	0.057 ±0.015
0.40-0.50	0.056 ±0.031	-0.000 ±0.021	-0.036 ±0.025	0.024 ±0.020	0.040 ±0.019
0.50-0.75	0.041 ±0.020	-0.001 ±0.014	-0.014 ±0.019	-0.009 ±0.013	-0.031 ±0.014
0.75-1.00	0.020 ±0.027	0.049 ±0.015	0.038 ±0.025	-0.002 ±0.018	-0.064 ±0.018

b) t-channel moments

-t (GeV/c)^2	Y_0^1	Y_1^1	Y_0^2	Y_1^2	Y_2^2
t_{min}-0.02	0.162 ±0.020	-0.025 ±0.010	0.170 ±0.019	-0.051 ±0.013	0.014 ±0.009
0.02-0.04	0.140 ±0.012	-0.038 ±0.006	0.146 ±0.012	-0.075 ±0.008	0.010 ±0.006
0.04-0.06	0.140 ±0.013	-0.045 ±0.007	0.129 ±0.012	-0.083 ±0.008	0.011 ±0.006
0.06-0.08	0.131 ±0.015	-0.039 ±0.008	0.122 ±0.014	-0.084 ±0.009	0.014 ±0.007
0.08-0.10	0.129 ±0.017	-0.039 ±0.009	0.119 ±0.016	-0.086 ±0.011	0.015 ±0.009
0.10-0.15	0.128 ±0.012	-0.054 ±0.007	0.119 ±0.012	-0.094 ±0.008	0.005 ±0.006
0.15-0.20	0.125 ±0.016	-0.053 ±0.009	0.101 ±0.015	-0.098 ±0.010	0.007 ±0.009
0.20-0.25	0.104 ±0.021	-0.036 ±0.012	0.137 ±0.020	-0.114 ±0.013	0.021 ±0.010
0.25-0.30	0.057 ±0.024	-0.038 ±0.014	0.099 ±0.023	-0.086 ±0.016	0.010 ±0.013
0.30-0.40	0.104 ±0.023	-0.056 ±0.013	0.106 ±0.022	-0.091 ±0.015	-0.009 ±0.012
0.40-0.50	-0.008 ±0.029	-0.039 ±0.017	0.063 ±0.026	-0.032 ±0.021	0.000 ±0.017
0.50-0.75	-0.015 ±0.019	-0.028 ±0.014	-0.016 ±0.019	0.012 ±0.014	-0.030 ±0.014
0.75-1.00	0.042 ±0.023	-0.040 ±0.018	-0.051 ±0.024	0.055 ±0.017	-0.027 ±0.017

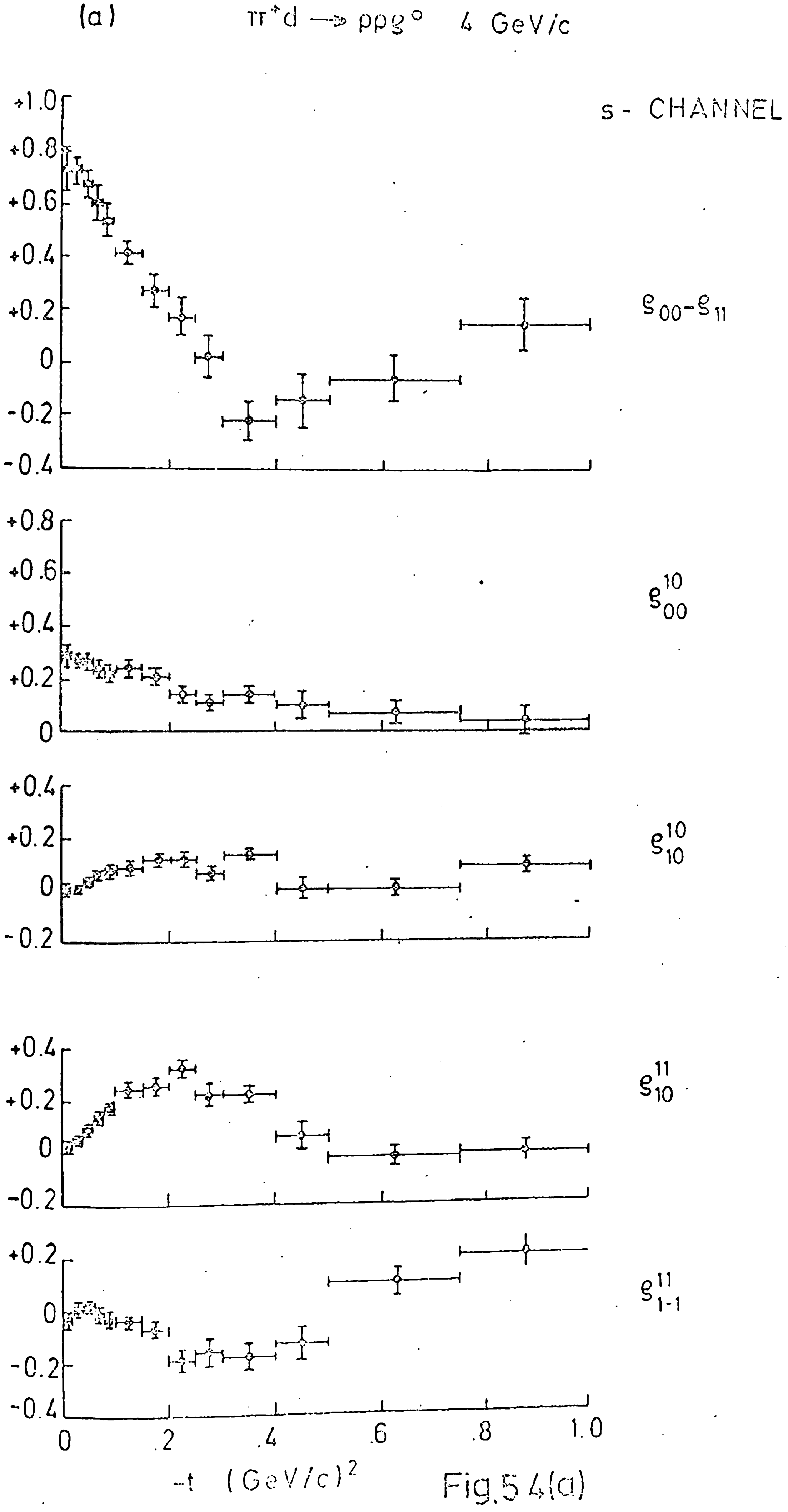
(a)
$\pi^+ d \rightarrow pp\rho^0$ 4 GeV/c
s- CHANNEL
+1.0
+0.8
+0.6
+0.4
+0.2
0
-0.2
-0.4
$\rho_{00}-\rho_{11}$
+0.8
+0.6
+0.4
+0.2
0
ρ_{00}^{10}
+0.4
+0.2
0
-0.2
ρ_{10}^{10}
+0.4
+0.2
0
-0.2
ρ_{10}^{11}
+0.2
0
-0.2
-0.4
ρ_{1-1}^{11}
0
.2
.4
.6
.8
1.0
-t (GeV/c)^2

Fig.5 4(a)

(b) $\pi^+ d \rightarrow pp\rho^0$ 4 GeV/c

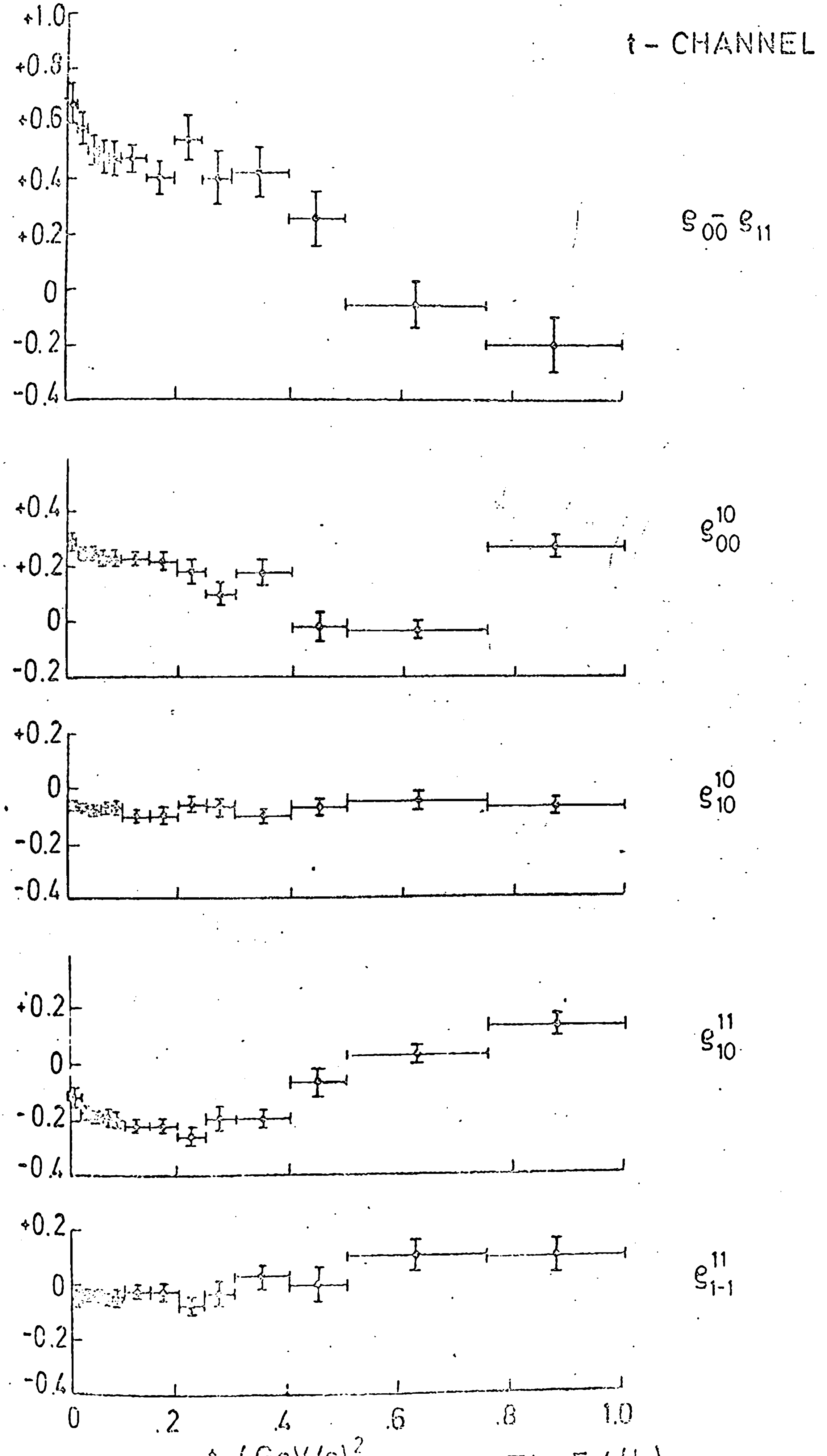

Fig. 5.4(b)

exclusion principle could still affect both the production angular distribution and the decay moments in the region $|t| < 0.03\ (\mathrm{GeV}/c)^2$ (i.e. in the first two t bins of Table 5.1) and the results within this region should be considered with care.

Considerable structure can be seen in the t-dependence of the density matrix elements in Fig. 5.4. In particular, it may be seen that ρ^{11}_{1-1} is negative (in the s-channel) in the range $0.1 \leqslant |t| \leqslant 0.5\ (\mathrm{GeV}/c)^2$, a point to which we shall return later, and also that ρ^{11}_{10} has a zero, both in the s and t - channels, at $t \sim -0.6\ (\mathrm{GeV}/c)^2$. Gutay et al [Ref. 28] have shown that this zero is observed in ρ^0 production over a very wide range of energy, and can be described by an absorption model approach. Gutay shows that s-channel ρ^{10}_{10} and ρ^{10}_{00} can also be expected to be zero at $t \sim -0.6\ (\mathrm{GeV}/c)^2$.

For each interval in t, the polynomial in M_0 was solved as described in Appendix 2. This leads, in general, to two very similar solutions for M_0. The two solutions for the set of equations are called Solutions 1 and 2, the solution with the slightly higher value of M_0 being called Solution 1. Figs. 5.5. and 5.6 show the distributions of $|M_0|^2$ $|M_-|^2$ and $|M_+|^2$ in the s-channel frame for Solutions 1 and 2. The distributions are seen to be very similar in the two cases, with $|M_-|^2$ alone showing a somewhat different $|t|$ dependence towards $t = 0$.

It can be seen that $|M_0|^2$ is dominant at lower $|t|$, as expected in One Pion Exchange models. At higher $|t|$ the dominant contributions are from M_+ and M_- but, in contrast to the C.E.R.N - Munich experiment

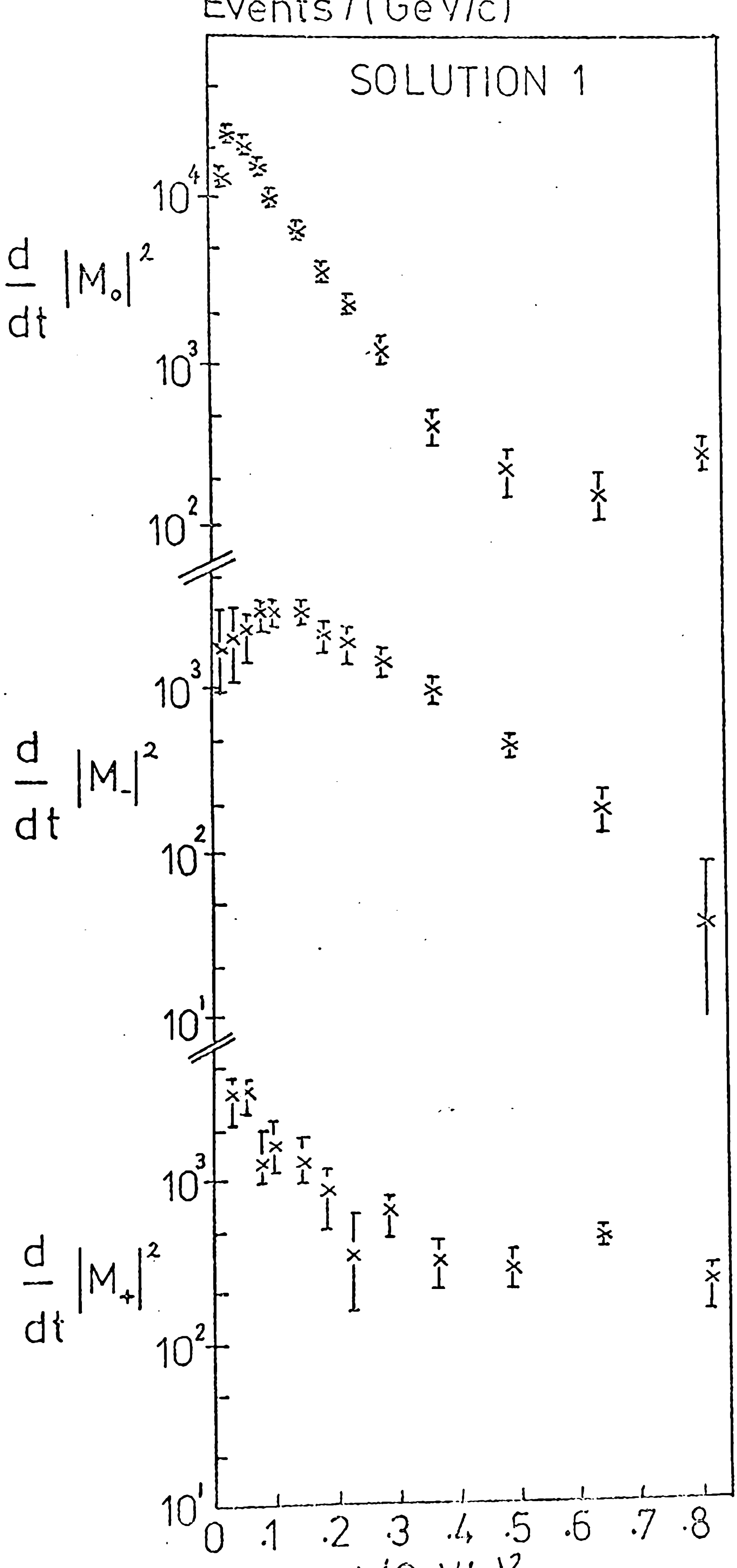
Events / (GeV/c)^2
SOLUTION 1
10^4
10^3
10^2
$\frac{d}{dt}|M_0|^2$
10^3
10^2
10^1
$\frac{d}{dt}|M_-|^2$
10^3
10^2
10^1
$\frac{d}{dt}|M_+|^2$
0
.1
.2
.3
.4
.5
.6
.7
.8
$-t$ (GeV/c)^2

Fig.5.5

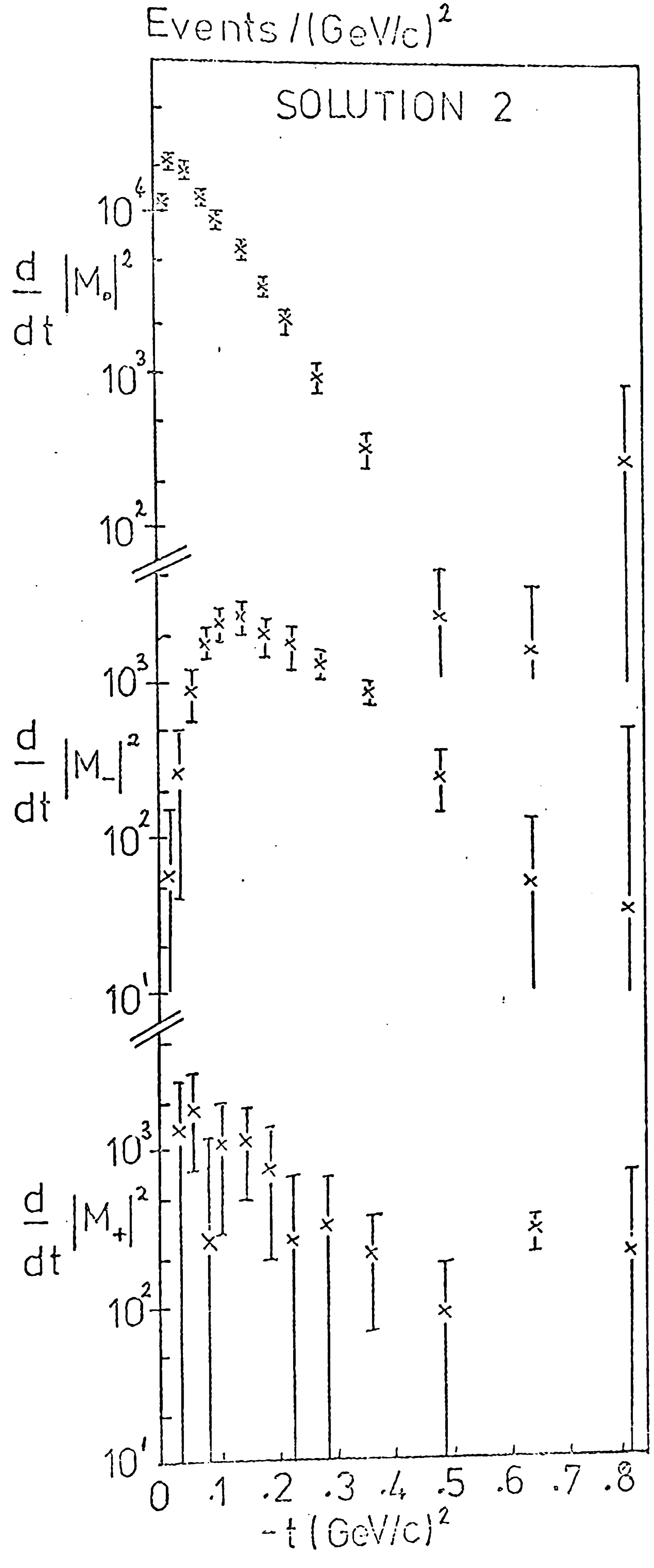
Events /(GeV/c)^2
SOLUTION 2
10^4
$\frac{d}{dt}|M_0|^2$
10^3
10^2
10^3
$\frac{d}{dt}|M_-|^2$
10^2
10^1
10^3
$\frac{d}{dt}|M_+|^2$
10^2
10^1
0
.1
.2
.3
.4
.5
.6
.7
.8
$-t$ (GeV/c)^2

Fig.5.6

results, our M_- is larger than M_+ over most of the $|t|$ range 0.1 to 0.6 $(GeV/c)^2$. This result depends only on the sign of ρ^{11}_{1-1}, a matrix element which can be determined directly from the moments. We compare our value of ρ^{11}_{1-1} with data at 17.2 GeV/c [Refs. 26] and 7 GeV/c [Ref. 29] in Fig. 5.7. There is clearly a tendency for ρ^{11}_{1-1} to be positive over a larger range of $|t|$ at higher energy. This behaviour should be expected from a simple Regge viewpoint, if we assume that most of $|M_+|^2$ comes from A_2 exchange. Then the relative amounts of $|M_+|^2$ to $|M_0|^2$ (and indirectly $|M_-|^2$) will increase with s. The variation of ρ^{11}_{1-1} has this sort of behaviour. It would appear probable therefore that some A_2 exchange is present.

Fig. 5.8. shows the variation up to $|t| = 0.3\ (GeV/c)^2$ of the other s-channel parameters of Estabrooks and Martin : cos θ^{11}_{10} (the phase angle between M_- and M_0), θ^{10}_{00} (the relative S - P wave phase in the helicity zero state), and $\gamma_s = |M_s| / |M_0|$. The differences between Solutions 1 and 2 are more evident in these parameters than in those shown in Figs. 5.5. and 5.6. Qualitatively, the differences correspond to those between the "down-up" and "up-down" solutions [Ref. 30] observed in $\pi\pi$ phase shift analyses. In particular, Solution 1 has a smaller value of γ_s and a phase difference θ^{10}_{00} closer to zero than does Solution 2. The lower γ_s would be expected in comparing the integration of the I = 0 s-wave phase shift across the ρ^0 mass band for the "down-up" and "up-down" solutions.

Another difference between Solutions 1 and 2 can be seen in the

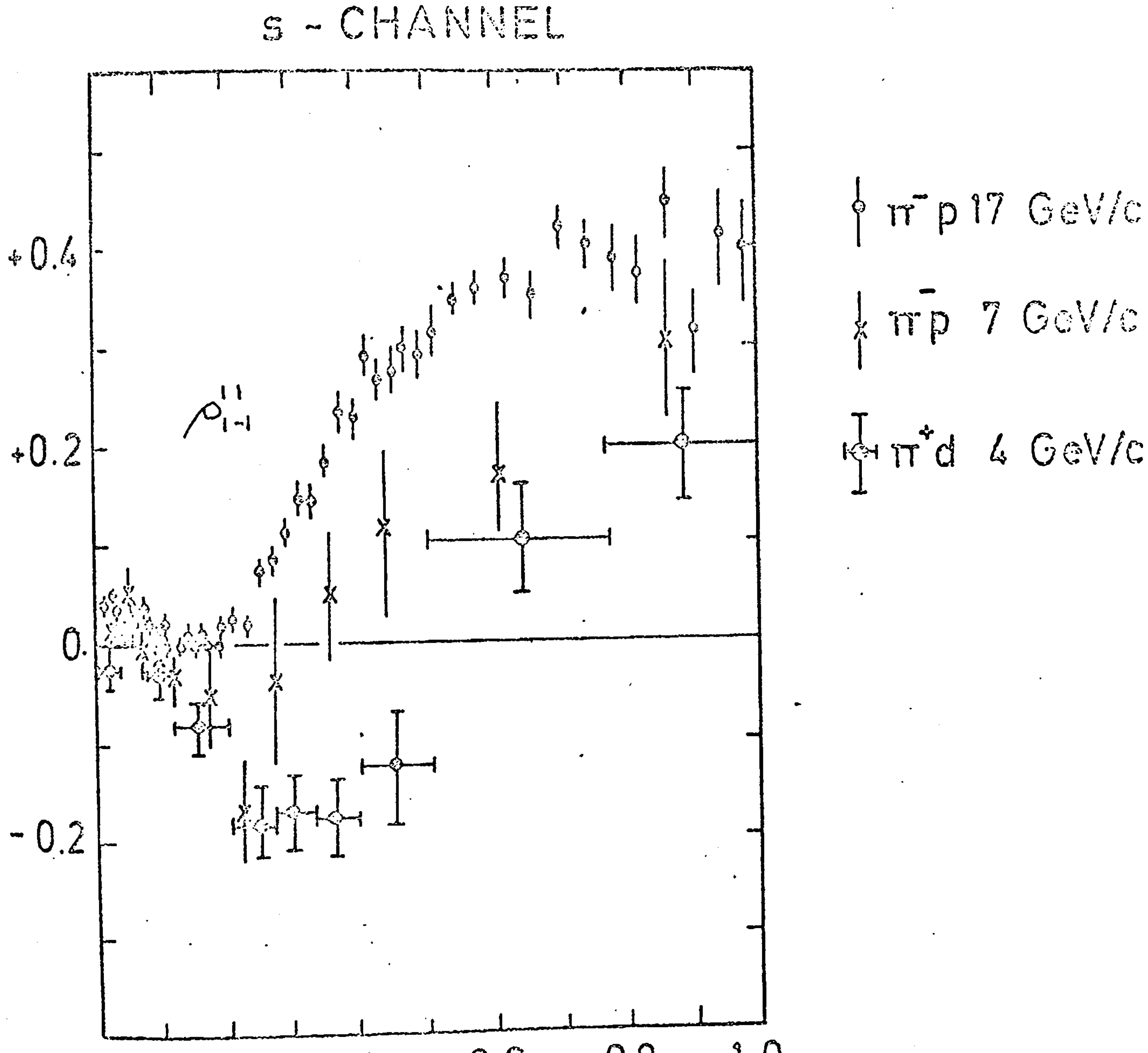
s - CHANNEL
+0.4
+0.2
0.
-0.2
0
0.2
0.4
0.6
0.8
1.0
-t (GeV/c)^2
ρ^{11}_{1-1}
π^-p 17 GeV/c
π^-p 7 GeV/c
π^+d 4 GeV/c

Fig.5.7

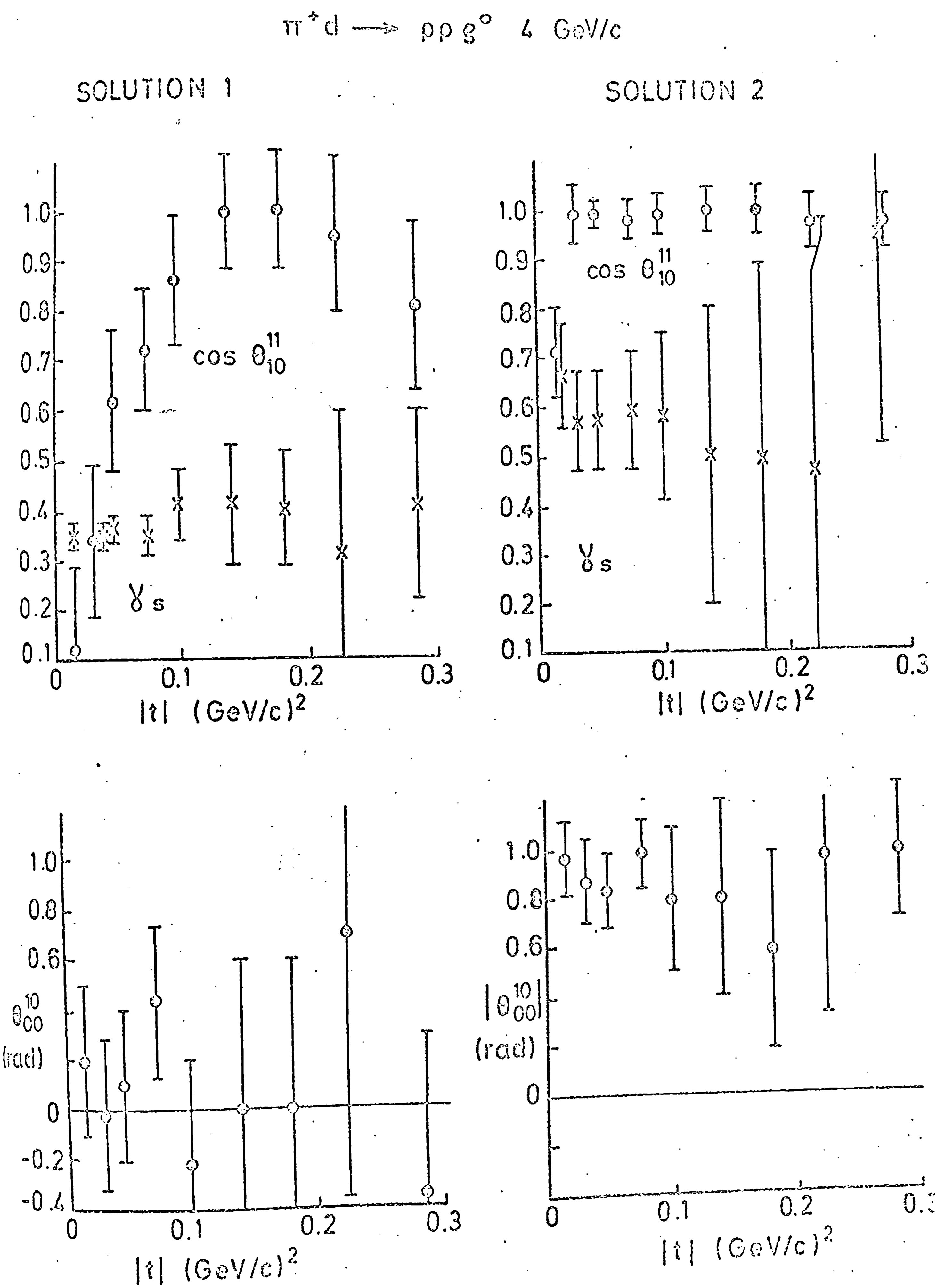

$\pi^+ d \rightarrow p p \rho^0$ 4 GeV/c

SOLUTION 1

SOLUTION 2

Fig. 5.8

behaviour of cos θ_{10}^{11} which, for solution 2, is consistent with being constant at 1.0. As the consequence, the sign of θ_{00}^{10} cannot be unambiguously determined from our system of equations. Therefore the modulus of θ_{00}^{10} has been plotted for Solution 2.

5.6. Conclusions of Amplitude Analysis.

Having decided to neglect the possibility of A_1 exchange, it is interesting to consider where the sizeable M_- contribution comes from. M_s and M_o obviously come from pion exchange itself, and the pure A_2 exchange amplitude will contribute to M_+. The only source of M_- therefore (and extra M_+) is the effect of absorption on these "pure" exchanges.

This can be tested by making a comparison of the results of this analysis with the predictions of an absorption model. We shall use the simple parameterisation due to Williams [Ref. 32] which describes absorbed π exchange and includes no contribution from A_2 exchange. We shall consider Solution 2 values mostly as they are nearest to the form suggested by the model.

Firstly, a comparison has been made of the Solution 2 behaviour of M_- with the form expected in the Williams model:-

$$M_- \sim \frac{t+\mu^2}{t-\mu^2} \phi(t)$$

where $\phi(t)$ is an exponential collimating factor of the form $e^{Bt/2}$. Note that as t approaches $-\mu^2$ we should expect a zero in this amplitude, or at least a dip, and our Solution 2 results for $|M_-|^2$ indeed have this behaviour. In addition, we observe in our Solution 2 values of cos θ''_{10} a constant value of 1.0. This is consistent with the Williams formula for M_- shown above. We should expect, if our data could go even lower, in $|t|$, a cross-over zero at $t = \mu^2$ when cos θ''_{10} would flip to -1.0. This has been observed at 17.2 GeV/c.

Further, we have extracted from the data the values of $|M_o|^2$ which correspond to simple spin 1 dipion production by One Pion Exchange. A good fit to $|M_o|^2$ of a Williams model-type amplitude.

$$|M_o|^2 = A \frac{(t_{MIN} - t)}{(t - \mu^2)^2} e^{Bt}$$

is obtained in the region $|t| \leqslant 0.3$ (GeV/c)^2 with a slope B = (7.2 ± 0.6) (GeV/c)$^{-2}$. This is close to the "typical" One Pion Exchange slope of 8 (GeV/c)$^{-2}$ and implies that the One Pion Exchange part of the reaction is obtainable.

The Solution 2 magnitude of M_- and its phase (θ''_{10}) and the magnitude of M_o can therefore be seen to be described well, at least qualitatively, by the Williams formulae. Quantitatively, however, we find it very difficult to describe the data with the Williams model alone.

The main quantitative predictions of the model are, firstly, that $|M_o|^2$ has the form already commented upon, and, secondly, that in the helicity one state the natural parity exchange component $|M_+|^2$ exceeds the unnatural parity exchange component $|M_-|^2$. This may be checked by comparing equations 13 (b) and 13(c) in Appendix 3. This is contrary to the data as it implies a non-negative ρ''_{1-1} .

In order to check the data more fully we eliminated the arbitrary parameter $\phi(t)$ by comparing ratios of the observed amplitudes with the predictions of the model. The comparison is shown in Fig. 5.9 using Solution 1 values (the conclusions of this comparison do not change for Solution 2.)

Our data do not agree with the predictions of the model. Quantities $(|M_{+}| / |M_{o}|)^2$ tend to lie below the predicted curve, while quantities $(|M_{-}| / |M_{o}|)^2$ are in reasonable agreement for $|t| < 0.1$ $(\mathrm{GeV}/c)^2$ but exceed the predictions at higher $|t|$. Ratios $(|M_{+}|^2 - |M_{-}|^2)/(|M_{+}|^2 + |M_{-}|^2)$ lie below the predictions.

In spite of the qualitative agreement between Solution 2 values of M_{-} and θ''_{10} with the predictions of the model, it can be seen that the magnitudes of each amplitude are not as expected. It is obvious that other effects (for example, A_2 exchange out of phase with the absorbed pion M_{+}) are necessary for there to be agreement with the data.

The Solution 1 set of results are seen to be somewhat different. We observe for $|t| < 0.1$ $(\mathrm{GeV}/c)^2$ values for cos θ''_{10} which depart strongly from + 1.0 and which are very different to the Williams predictions. If Solution 1 is to be considered the correct set, then we see that the Phase Coherence hypothesis (i.e. cos $\theta''_{10} = +1.0$) made in many early phase shift analyses [Ref. 31] is incorrect. This departure from + 1.0 may be described in the "Strong Cut Model" of Kimel and Reya [Ref. 33] where a

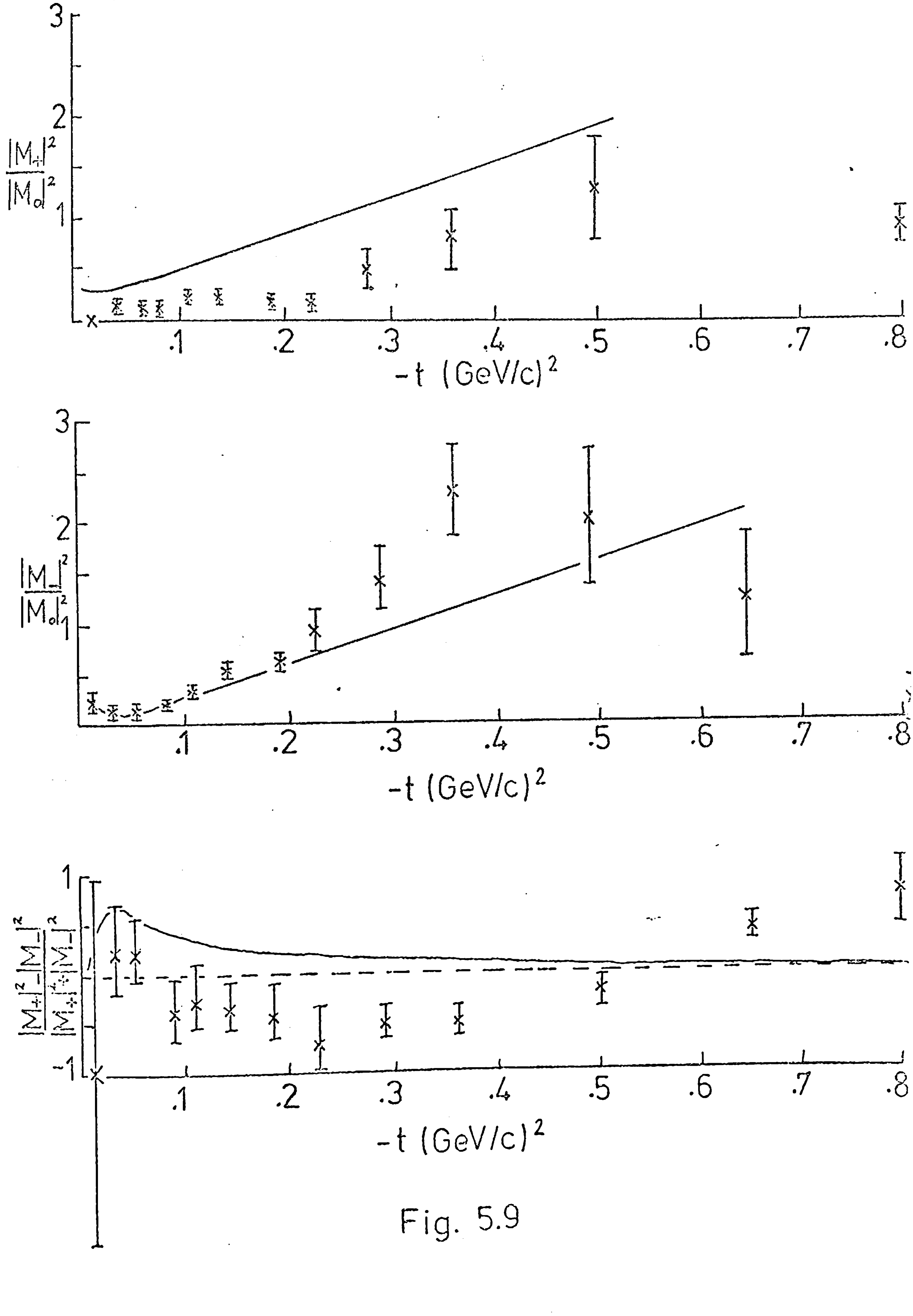
3
2
1
|M+|²/|M0|²
.1
.2
.3
.4
.5
.6
.7
.8
-t (GeV/c)²
3
2
1
|M-|²/|M0|²
.1
.2
.3
.4
.5
.6
.7
.8
-t (GeV/c)²
1
-1
(|M+|² - |M-|²)/(|M+|² + |M-|²)
.1
.2
.3
.4
.5
.6
.7
.8
-t (GeV/c)²

Fig. 5.9

sizeable background coming from other production processes is added to the Williams type M_- amplitude with a phase of $\pi/2$ relative to M_0. The phase of $\pi/2$ is necessary so that the zeroes in ρ^{10}_{10} and ρ^{11}_{10} at $t = -\mu^2$ (observed in 17.2 GeV/c data) are not destroyed. The background also explains the dip rather than a zero in $|M_-|^2$ at $t = -\mu^2$ (also seen at 17.2 GeV/c). It is obvious that any similar strong cut model can reproduce the departure from Phase Coherence. Kimel and Reya state that the data has to be described by a more complicated model of the strong cut type. For $|t| > 0.2$ (Gev/c)^2 they assert that the data is indicative of sizeable A_2 exchange whereas at lower $|t|$ (at least from the Solution 1 point of view) a strong cut approach is necessary without any large A_2 contribution. The Solution 1 set of values could support this view. Apart from this model it should be noted that a moderate A_1 contribution would also disrupt Phase Coherence.

To summarise, we have two sets of solutions, each of which may be described to some extent from the absorption model approach. Solution 2 is seen to be the simpler of the two and to be in agreement with older ideas of Phase Coherence and the simple absorption model.

To make a definite choice between Solutions 1 and 2, it is necessary to introduce more data. The P wave and S wave parts of the reaction can be extrapolated to the pion pole and the pion-pion phase shifts extracted. The S wave phase shifts then give definite predictions on the shape of the $\pi^0 \pi^0$ mass spectrum obtained in the reaction.

$$\pi^- p \rightarrow \pi^0 \pi^0 n$$

Estabrooks and Martin [Ref 34] have compared their results with one $\pi^o \pi^o$ mass spectrum and have chosen the set corresponding to this experiment's Solution 2 as being the physical solution. However, this remains to be confirmed.

5.7. Application to Phase Shift Analysis in the Rho Region.

The usual way of describing real particle two-body scattering is by means of a phase shift analysis as a function of the two-body centre of mass energy. In the case of reaction (1), one of the initial particles is a virtual (off-shell) particle with several other production processes occuring simultaneously. Consequently some analysis is necessary before the two-body scattering part of the reaction amplitude may be extracted. Once such amplitudes are obtained , phase shifts can be used to provide a description of the scattering process. In this way it is possible to use one experiment of fixed beam momentum to provide information on real particle pion-pion scattering across a large energy range.

The amplitude analysis described before may be repeated in intervals of, say, 20 MeV/c^2 in $\pi\pi$ effective mass across the rho region. For each mass interval we may obtain, if the overall normalisation is known, the on-shell $\pi\pi$ phase shift δ_1^1 from a fit to M_o of the form

$$M_o = A \frac{\sqrt{-t'}}{(\mu^2 - t)} e^{b(t - \mu^2)} \sqrt{3}\, f_P$$

where $f_p = \sin \delta_1^1 \; e^{i\, \delta_1^1}$

by obtaining the value of M_o at the pion pole. The ratio $\gamma_s = |M_s| \;/\; |M_o|$

can be obtained on-shell (it is almost constant in t anyway), and θ^{10}_{00} the relative S-P phase, can be obtained on-shell also. Both of these may be obtained by a simple extrapolation method.

Then we have

$$\gamma_s \, e^{i\theta^{10}_{00}} = \frac{\frac{2}{3} f_s^{I=0} + \frac{1}{3} f_s^{I=2}}{\sqrt{3}\, f_p}$$

as outlined in Section 5.1. from which the I = 0 S wave phase shift can be obtained, if the I = 2 S wave phase shift can be assumed from analysis of other channels.

Unfortunately, owing to insufficient statistics we have not made this form of phase shift analysis. Evaluation of the phase shifts by a cruder method is described in the following section.

5.8. $\pi\pi$ Phase Shifts for $M_{\pi\pi}$ below 1 GeV/c^2.

The two t-channel helicity zero spherical harmonic moments which are non-zero in the rho region are $\langle Y_0^1 \rangle$ and $\langle Y_0^2 \rangle$. These indicate the presence of strongly interfering spin 1 and spin 0 states as shown by equation 1 (b) in Section 5.1. The spin 1 part of the scattering amplitude can be assumed to be the rho itself, while the isospin zero S wave phase shift can be determined from the $\langle Y_0^1 \rangle$ interference term, if the isospin 2 S wave phase shift is assumed.

The value of 1 GeV/c^2 as the limit of validity may be defended for various reasons. The channels $\pi^+ n \rightarrow p K \bar{K}$ and $\pi^+ n \rightarrow p \pi^+ \pi^+ \pi^- \pi^-$

can be seen to have a negligible cross section below 1 GeV/c^2 (see Chapter 6), and it is reasonable to assume that other (mostly neutral) final states of this kind also have a negligible cross section in this region. This allows us to write all phase shifts with elasticity 1. Above 1 GeV/c^2 spin 2 waves become of increasing importance and the elasticity assumption becomes incorrect. Also at the K $\bar{K}$ threshold (0.98 GeV/c^2) the spherical harmonic moments depart from the smooth variation they possess throughout the rho region [Fig. 5.2] indicating some very different background behaviour.

We expand the expression for the decay angular distribution from the three spin states of pure One Pion Exchange:-

$$\frac{d\sigma}{d\cos\theta} = ƛ^2 \left[A_1 + B_1 \cos\theta + C \cos^2\theta\right]$$

where $A_1 = \frac{4}{9}\sin^2\delta^0_0 + \frac{1}{9}\sin^2\delta^2_0 + \frac{4}{9}\cos(\delta^0_0 - \delta^2_0)\sin\delta^0_0 \sin\delta^2_0$

$$B_1 = 4\cos(\delta^0_0 - \delta^1_1)\sin\delta^0_0 \sin\delta^1_1 + 2\cos(\delta^2_0 - \delta^1_1)\sin\delta^2_0 \sin\delta^1_1$$

$$C_1 = 9\sin^2\delta^1_1$$

where δ^I_L denotes a phase shift of spin L, isospin I.

[For $\pi^+\pi^o$ scattering in the channel $\pi^+ p \rightarrow \pi^+\pi^o p$ we have a similar expression with

$A_2 = \sin^2\delta^2_0$ $\quad B_2 = 6\cos(\delta^2_0 - \delta^1_1)\sin\delta^2_0 \sin\delta^1_1$

$C_2 = C_1$

There is naturally no isospin 0 component in the $\pi^+\pi^o$ state. We shall use these trigonometric functions].

We may now state the following identities:-

$$\tan \delta_1^1 = \frac{\sin(2\,\delta_0^2)}{3(B_2/C_2) - 2\sin^2 \delta_0^2} = \frac{2\sin(2\,\delta_0^0)}{9\left[(B_1/C_1) - \frac{1}{3}(B_2/C_2)\right] - 4\sin^2 \delta_0^0}$$

allowing us to write

$$\tan \delta_1^1 = \sin(2\,\delta_0^0) \;/\; (3\,a\,N/D - 2\sin^2 \delta_0^0) \qquad (3)$$

where $N = (C_1 + 3A_1)/C_1$ and $D = 3B_1/(3B_1 - B_2)$

and 'a' is the assyrnmetry parameter in the decay angular distribution, defined as:-

$$a = \frac{\text{Forward} - \text{Backward}}{\text{Forward} + \text{Backward}} = \frac{B_1}{\left[2A_1 + \frac{2C_1}{3}\right]} = \sqrt{3}\,\rho_{00}^{10}$$

We are now able to obtain the isospin zero S wave phase shift, using the very small t dependence of the anisotropy 'a' [Ref 35]. The method consist of obtaining the S-wave phase shift by extrapolating $\langle Y_0^1 \rangle$ to the pion pole, and obtaining the on-shell anisotropy 'a' with which equation (3) may be solved numerically for δ_0^0. We note that the validity of this procedure has been the subject of some discussion in the literature [Ref. 26, 35, 36].

It is difficult to know which quantity (or combinations of quantities) can be extrapolated reliably through the physical region to the pion pole. Martin and Estabrooks [Ref. 26] stress that $|M_0|$, $|M_s|/|M_0|$ and θ_{00}^{10} are the quantities which should be extrapolated rather than the experimentally determined spherical harmonic moments. In this analysis we assume that $\langle Y_0^1 \rangle$ is capable of being extrapolated to the pion pole and that the effects of absorption on the extrapolated value are small. Certainly, if s-channel 'α' was used, we may expect absorption to distort the smooth variation of 'α' with t in the vicinity of t = 0. [Comparison may be made with the Williams model [Ref. 32]]. However, even in the s-channel, it is reasonable to assume that the absorption effect is narrow about t = 0 enabling an extrapolation to be made through it [see Fig. 11 of Ref. 36(Kane).] Williams considers the on-shell anisotropy determined in the s-channel to be within 20% of the true on-shell value; a deviation comparable with the statistical error in this experiment.

In our t-channel data we observe a very smooth variation of the $\langle Y^1_0 \rangle$ moment in each $\pi\pi$ mass bin in the region from $|t| = \mu^2$ to $|t| = 12\ \mu^2$. The region $|t| < \mu^2$ has been neglected because of possible Pauli exclusion effects. We have assumed that absorption has a small effect in these t-channel moments and that the value of the extrapolated moment obtained in this way is very similar to the true on-shell value.

The phase shifts obtained in this experiment are similar to those of Ref. 35. Consequently, any departure of our phase shift results from those of Estabrooks and Martin [Ref. 34.] can probably be ascribed to inaccuracies in the assumptions made here.

A typical extrapolation is given in Fig. 5.10(a), showing the variation of 'α' with momentum transfer up to $|t| = 12\ \mu^2$. We have found a linear extrapolation to be adequate. The on-shell values of 'α' obtained in this way are shown in Fig. 5.10 (b).

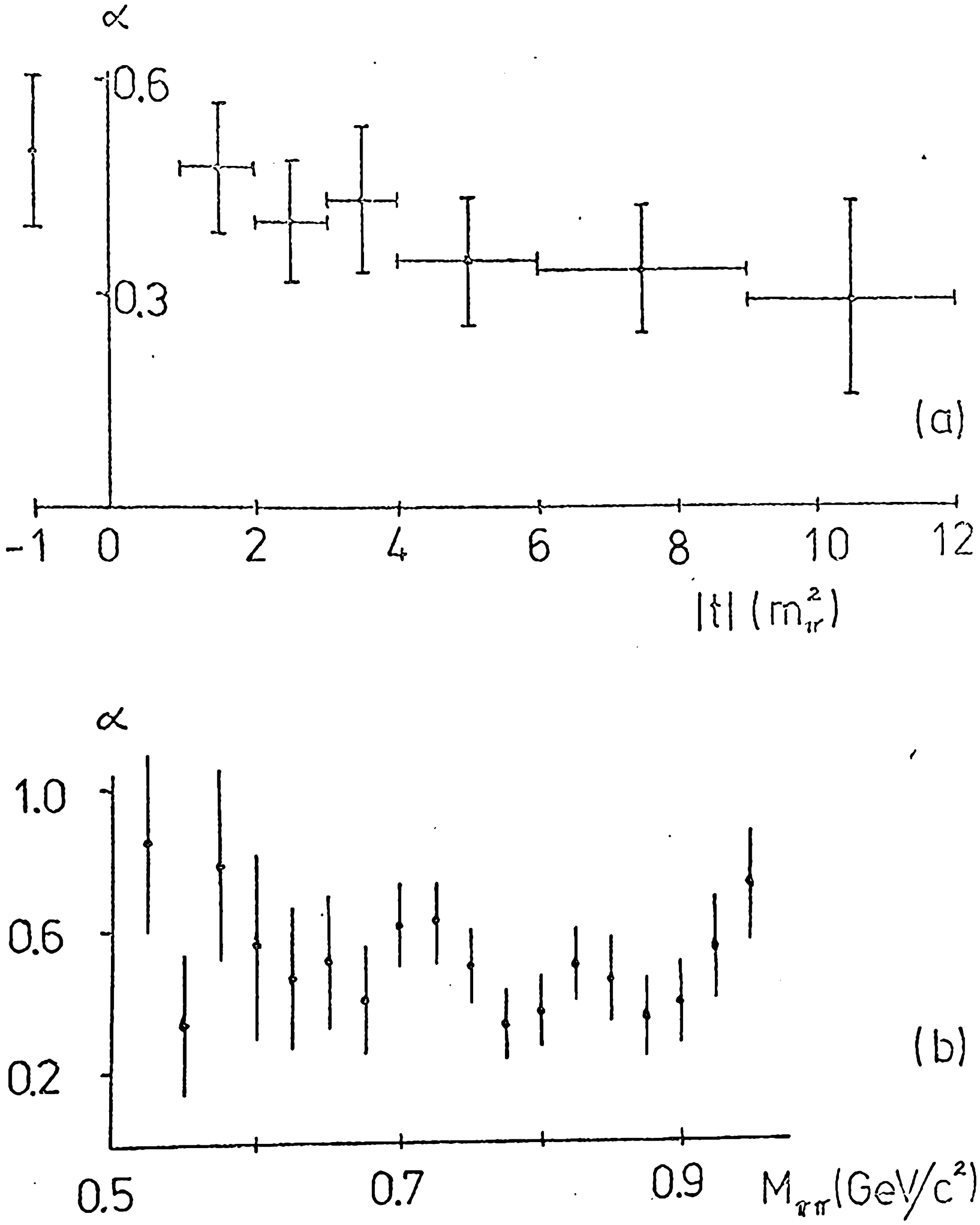

Fig. 5.10 Assymmetry Parameter 'a'

(a) at $M_{\pi\pi} = 0.75$ GeV/c^2, versus $|t|$

(b) extrapolated values versus $M_{\pi\pi}$

The δ_1^1 phase shift was supplied by a relativistic Breit-Wigner

$$\tan \delta_1^1 = \frac{M_R}{(M_R^2 - m^2)} \frac{2(q/q_R)^3}{[1 + (q/q_R)^2]} \Gamma_R^0$$

almost identical to the form used in Appendix 1 with M_R = 0.765 GeV/c^2 and Γ_R^0 = 0.125 GeV/c^2. There is very little change in the δ_0^0 phase shifts obtained in this way if Γ_R^0 is varied from 0.150 to 0.110 GeV/c^2. The δ_0^2 phase shifts were taken from Baton et al [Ref. 37.]

The resulting phase shifts across the rho region are shown in Fig. 5.11. There are, in general, two ambiguous solutions for each $\pi\pi$ mass interval, forming the DOWN-DOWN, UP-DOWN, DOWN-UP or UP-UP branches. We see that the DOWN-UP solution would appear to be of Breit-Wigner shape leading to a narrow (~ 100 MeV) mass enhancement reminiscent of a narrow S wave σ meson. However, we recall that an (UP or DOWN) -DOWN solution would be more compatible with the fit obtained in Appendix 1. where a much wider effect is required. These alternatives will be discussed further.

It can be seen that our solutions, obtained in this simple way, are quite compatible with the larger phase-shift analyses of this region undertaken in the last two years. Current opinion would favour a phase shift rising slowly through the rho region reaching 90° at about 900 MeV/c^2 [the UP-DOWN branch] followed by a sharp jump to 270° at about 1 GeV/c^2. For a summary of the status of $\pi\pi$ scattering the reader is referred to the review by Morgan [Ref. 30].

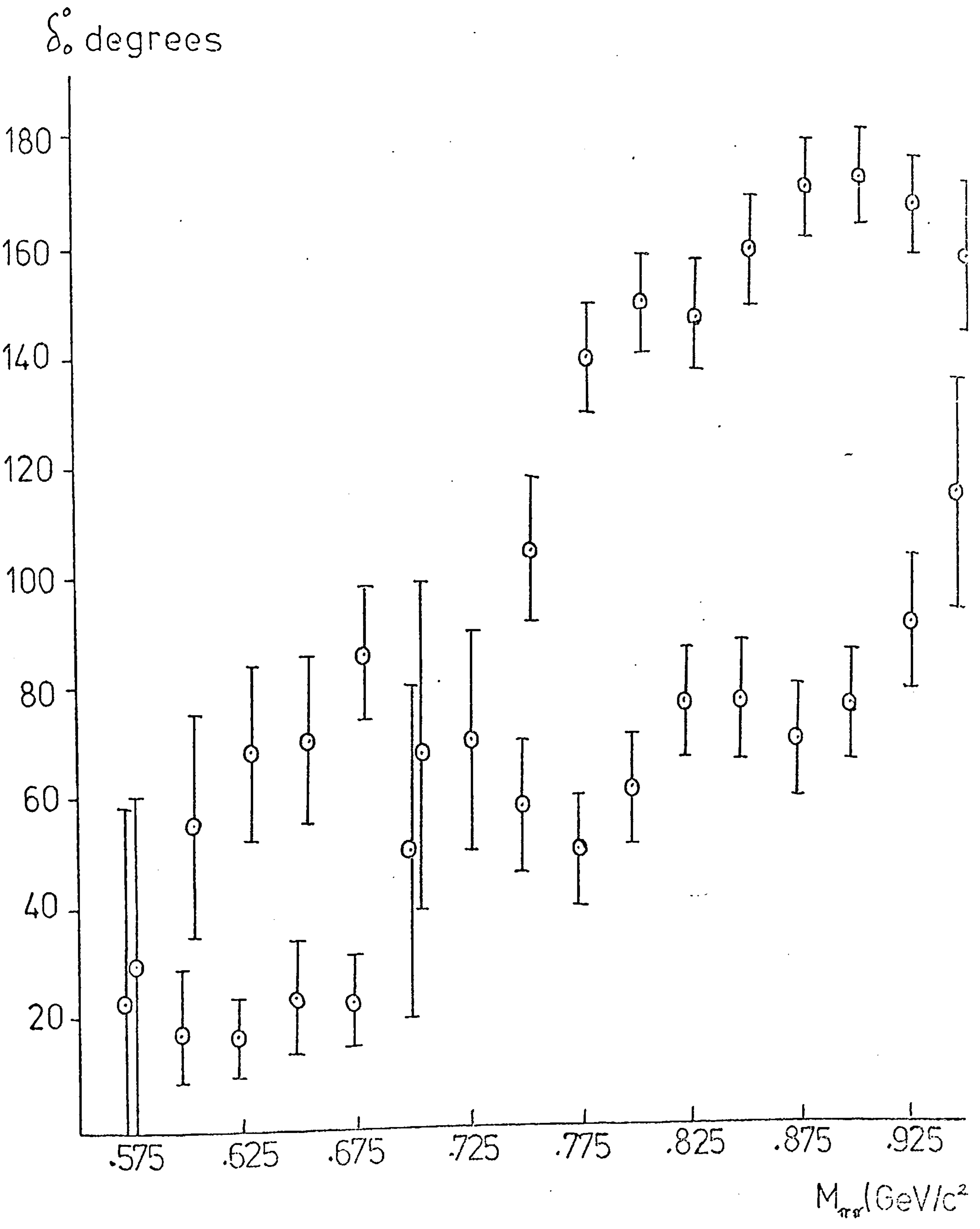

Fig. 5.11. Isospin zero S wave Phase Shifts.

The values of δ_0^0 obtained in this experiment can be compared to the results of various other phase shift analyses as shown in Fig. 5.12 (with a reference list in Table 5.2.) . A somewhat different method for obtaining the phase shifts has been used in each analysis. The results are seen to be qualitatively the same for the UP-DOWN solutions (only the one favoured UP-DOWN solution of Protopopescu et al is shown) although quite large disagreements (~ 15°) remain at certain masses.

The UP results obtained in this experiment around 0.8 GeV/c^2 in $\pi\pi$ mass are compatible with several phase shift analyses made before 1971 [Ref. 30]. However, the UP solutions obtained recently by Estabrooks and Martin and Grayer et al in the C.E.R.N. - Munich experiment are about 30° lower. The UP solution at higher $\pi\pi$ mass would appear to be the unphysical solution anyway. It is the purpose of the next reaction to rule out our very large δ_0^0 UP values, and the C.E.R.N. -Munich people have done the same.

A comparison of the Estabrooks and Martin δ_0^0 values has been made to the shape found for the $\pi^0\pi^0$ mass spectrum obtained in the reaction

$$\pi^- p \longrightarrow \pi^0 \pi^0 n$$

for which no P wave (I = 1) can contribute. The $\pi^0\pi^0$ mass spectrum from the experiment by Apel et al [Ref. 38] can be seen to be almost perfectly fitted by the Estabrooks and Martin Solution 1 [Ref. 34] (which corresponds to Solution 2 in this experiment) up to 1.0 GeV/c^2 in $\pi^0\pi^0$ mass. However, the recent experiment by Skuja et al [Ref. 39], while confirming the Estabrooks and Martin Solution 1 above the phase shift cross-over point of 0.77 GeV/c^2 in $\pi\pi$ mass prefers below 0.77 GeV/c^2 a set of DOWN

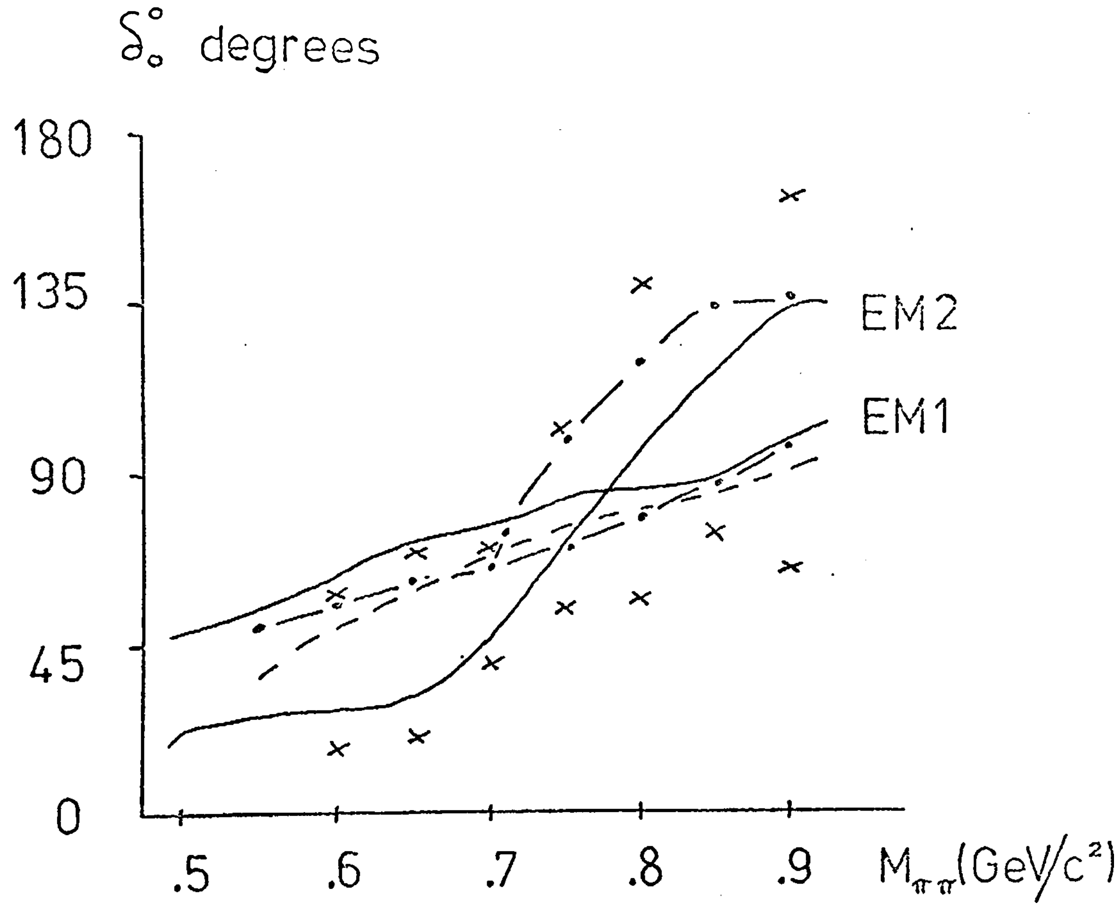

Fig. 5.12 Interpolated Variation of δ_0^0 with $\pi\pi$ mass for three recent phase shift analyses

Table 5.2. [See Fig. 5.12]

Symbol	Reference
• —— •	Grayer et al, Proc. Philadelphia Conference April 1972.
— — — —	S. D. Protopopescu et al, Berkeley Preprint, LBL-970
———— EM 1 ———— EM 2	Solutions 1 and 2, P. Estabrooks and A. D. Martin, CERN TH-1661.
x x	This experiment

phase shifts even smaller than the Estabrooks and Martin Solution 2 and more like the low $\pi\pi$ mass DOWN values from this experiment. Further data on this channel is awaited with interest.

5.9. Solution of the UP-DOWN Ambiguity.

The ambiguity between the phase shift alternatives can be partially solved in a crude way by considering the different contributions from the various UP-DOWN combinations to the number of events on the mass plot. Using the fitting program described in Appendix 1. the $\pi\pi$ mass and $|t|$ spectra were fitted between 0.560 and 0.960 GeV/c^2 in $\pi\pi$ mass and less than 0.3 $(\mathrm{GeV}/c)^2$ in $|t|$, assuming only spin 1 rho and spin 2 f contributions, and normalising to the number of events in the data. Not surprisingly, a bad fit is obtained.

Using this normalisation, we can find the number of events which contribute to the mass plot for each δ_0^0 branch and the Baton values of δ_0^2. This S wave effect can now be added to the previous spin 1 and 2 contributions and the fit re-normalised. We may now compare two distributions:-

1. the re-normalised S wave contribution alone
2. the experimental data less the re-normalised spin 1 and spin 2 contributions.

If the choice of S wave shape has been a good one then the shape of these two distributions will be very similar. Such a subtraction should be valid as the S wave contribution is almost unaffected by going off-shell.

However, as we are subtracting from the data (with a $\sqrt{N}$ type error) a number comparable in size, we may only compare the general shape of the distributions. The two distributions for each of the four branches of the δ_0^0 phase shifts are shown in Figs. 5.13. (a) to (d). The two lines on the plots are not fits to the data, but serve to indicate the trend. The spread in the subtraction points at the high mass end is a consequence of irregular behaviour of the data (this may be compared to the mass plot in Fig. A1.1 (b)).

From the sets of distributions, two statements can be made. Firstly, the DOWN-UP solution can be definitely excluded, there simply is not enough room for it on the mass plot. Secondly, the UP-DOWN solution would appear to be the most preferred set in agreement with Martin and Estabrooks. For comparison, we show in Fig. 5.13.(e) the Morgan and Shaw UP-DOWN prediction from dispersion relation calculations [Ref. 40].

Various possible causes for the discrepancy in the two UP-DOWN curves have been investigated. N^* contamination could qualitatively explain the difference, although its cross section is much too low. Similarly, different parameters for the rho meson could improve the distributions slightly. Inherent in this method is the assumption that at low $|t|$, spin 1 and spin 0 have the same differential cross section (which is a reasonable deduction from the amplitude analysis of a previous section), and which may also be not exactly correct. Far more likely an effect is a slight distortion of the δ_0^0 phase shifts by the assumptions made in the extrapolation. This would lead to a different S wave contribution and a change in the overall normalisation and shape.

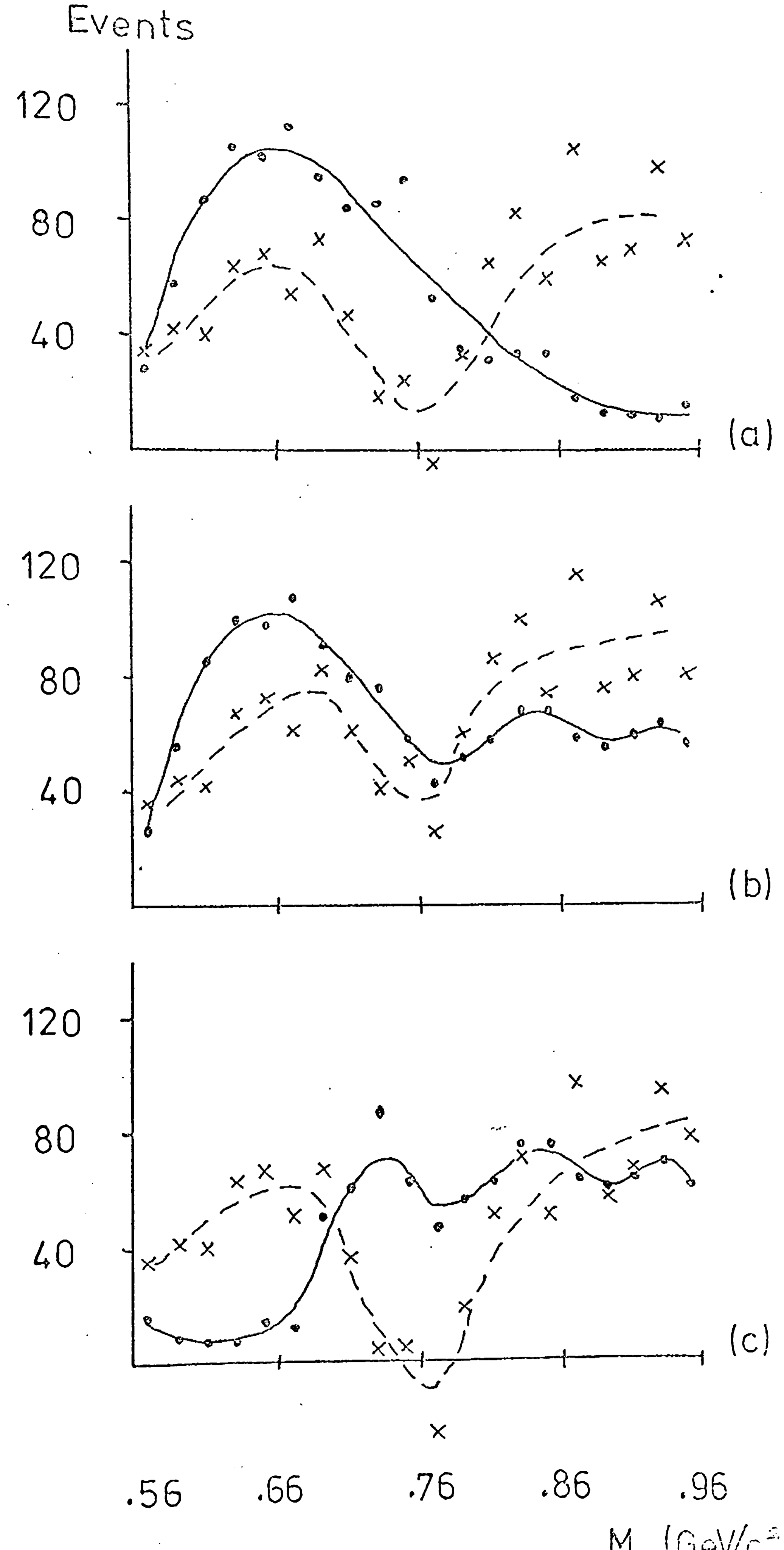
Events
120
80
40
(a)
120
80
40
(b)
120
80
40
(c)
.56
.66
.76
.86
.96
Mππ(GeV/c²

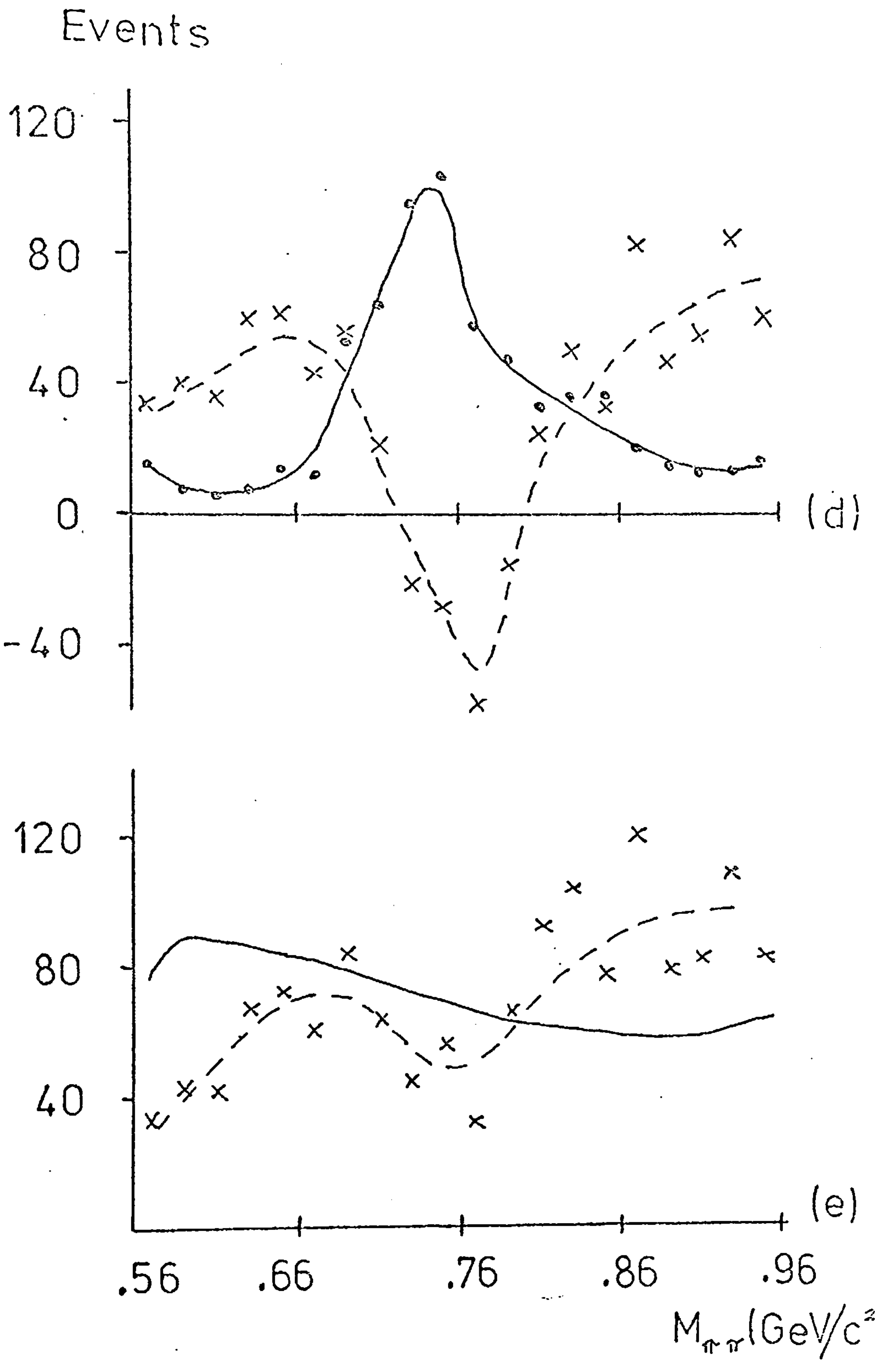

Fig. 5.13 S Wave Subtraction Plots

S wave shape (a) UP-UP (b) UP-DOWN
(c) DOWN-DOWN (d) DOWN-UP (e) MORGAN-SHAW

Points . and line —— = S wave cross section

Points x and line --- = Data minus P and D wave cross sections.

There is little doubt, however, that the UP-DOWN solution appears to be the most favoured, if not the only, possibility from this experiment. This predicts a δ_0^0 phase shift gradually rising through the rho region to be about 90° at 900 MeV/c^2. We note that this method would not be very useful in distinguishing between intermediate sets of phase shifts (such as the C.E.R.N. - Munich UP values) where the UP phase shift is somewhat lower than that obtained in this experiment. The shapes of the subtracted mass spectra for each set of δ_0^0 would be very similar. The only remaining method of distinguishing between solutions is direct comparison with $\pi^0\pi^0$ spectra.

CHAPTER 6

Branching Ratios of the f^o Meson

6.1. Introduction.

In a full investigation of $\pi\,\pi$ scattering it is necessary to consider the existence of channels other than the elastic one. Unfortunately, not all the inelastic channels may be studied in this experiment; in particular with regard to isospin zero S wave determination in the rho region, the reaction $\pi^+ \pi^- \longrightarrow \pi^o \pi^o$ is unmeasurable. However, preliminary to an analysis involving most of the inelastic channels produced by One Pion Exchange which are available to us, we give below a measurement of the decay rates of two other f^o decay modes. The f^o mass region shows a large enhancement in the $\pi^+ \pi^-$ spectrum with large, but not total, spin 2 behaviour [Ref. 14.]. In the other decay modes we have observed it is probable that spin 2 is again the dominant spin; although this is difficult to establish conclusively because of the size of backgrounds, and we have proceeded to measure the total effect.

6.2. Previous Experiments.

Previous estimates [Ref. 3.] of the branching ratios $\Gamma\,(f^o \rightarrow \pi^+ \pi^+ \pi^- \pi^-) \;/\; \Gamma\,(f^o \rightarrow \pi^+ \pi^+)$ and $\Gamma\,(f^o \longrightarrow K\,\bar{K}) \;/\; \Gamma(f^o \longrightarrow \pi\,\pi)$ are few and are of low statistics.

Experiments by Ascoli et al [Ref. 41] and, more recently, by Anderson et al [Ref. 42] are the only ones in which the decay of the f^o to four charged pions has been clearly observed and in which an estimate of the branching ratio $\Gamma\,(f^o \rightarrow \pi^+ \pi^+ \pi^- \pi^-) \;/\; \Gamma\,(f^o \rightarrow \pi^+ \pi^-)$

has been possible. Anderson estimates the value of this branching ratio to be $(5.5 \pm 1.0) \times 10^{-2}$. Other experiments have determined upper limits.

The $f^o \rightarrow K \bar{K}$ branching ratio is a difficult quantity to measure because of the proximity of the A_2^o meson, also decaying into $K\bar{K}$. As both mesons have the same $J^P(2^+)$ and have masses differing by less than the width of either of them, possible interference effects should be considered in the $K\bar{K}$ mass spectrum. The effects of such $f^o - A_2^o$ interference have been described in papers by Biswas [Ref. 43]. and by Bernstein and Feinberg [Ref. 44.]. In the literature, there are several upper limits and measurements of the branching ratio $\Gamma (f^o \rightarrow K\bar{K}) / \Gamma (f^o \rightarrow \pi\pi)$; all of which, except for the Biswas paper, neglect interference effects. Fortunately the $A_2 \rightarrow K\bar{K}$ branching ratio can be determined independently and without interference by looking at the $A_2^{\pm} \rightarrow K^{\pm} K^o$ decay modes since the A_2 has isospin one. The channel $f^o \rightarrow K\bar{K}$ has been seen to exist with a branching ratio $\Gamma (f^o \rightarrow K \bar{K}) / \Gamma (f^o \rightarrow \pi\pi)$ less than about 10%.

6.3. Cross Section $f^o \rightarrow \pi^+ \pi^-$.

In a recent paper [Ref. 14] the Birmingham - Durham - Rutherford Collaboration reported the production of the f^o meson into the neutral $\pi \pi$ system using data from the first exposure of the experiment in the reaction

$$\pi^+ d \rightarrow p_s \, p \, \pi^+ \pi^- \qquad (1)$$

where p_s denotes a spectator proton.

From this data the cross section for f^o ($\rightarrow \pi^+ \pi^-$) production for events below 0.3 $(GeV/c)^2$ in four momentum transfer squared to the $\pi\pi$ system was estimated. This estimate, made with similar fits to those described in Chapter 4, was 0.248 ± 0.030 m b. The $\pi^+ \pi^-$ mass spectrum for events below $|t|$ of 0.3 $(GeV/c)^2$ is described in Appendix 1.

6.4. $f^o \rightarrow \pi^+ \pi^+ \pi^- \pi^-$.

The same exposure yielded 4341 fits to the reaction

$$\pi^+ d \rightarrow p_s \, p \, \pi^+ \pi^+ \pi^- \pi^- \qquad (2)$$

after events incompatible with ionisation measurements had been removed and the following cuts had been made to the data

1. Fit Probability, $P_{\chi^2} > 0.001$
2. Missing Mass Squared, MM^2, in the range
   $-0.03 < MM^2 < 0.008 \quad (GeV/c^2)^2$
3. Spectator Momentum, $p_s < 0.3$ GeV/c

A preliminary estimate of the total cross section for reaction (2) was made assuming a muon contamination of 6%. We found

$$\sigma \; (\pi^+ d \rightarrow p \, p \, 2\pi^+ 2\pi^-) = 0.5 \pm 0.1 \text{ m b}$$

Fig. 6.1 shows the four pion mass spectrum for reaction (2) before any cuts in four momentum transfer squared to the four pion system, t, have been made. Fig. 6.2. shows the spectrum for events with $|t| < 0.3$ $(GeV/c)^2$. By taking only peripheral events for our analysis we

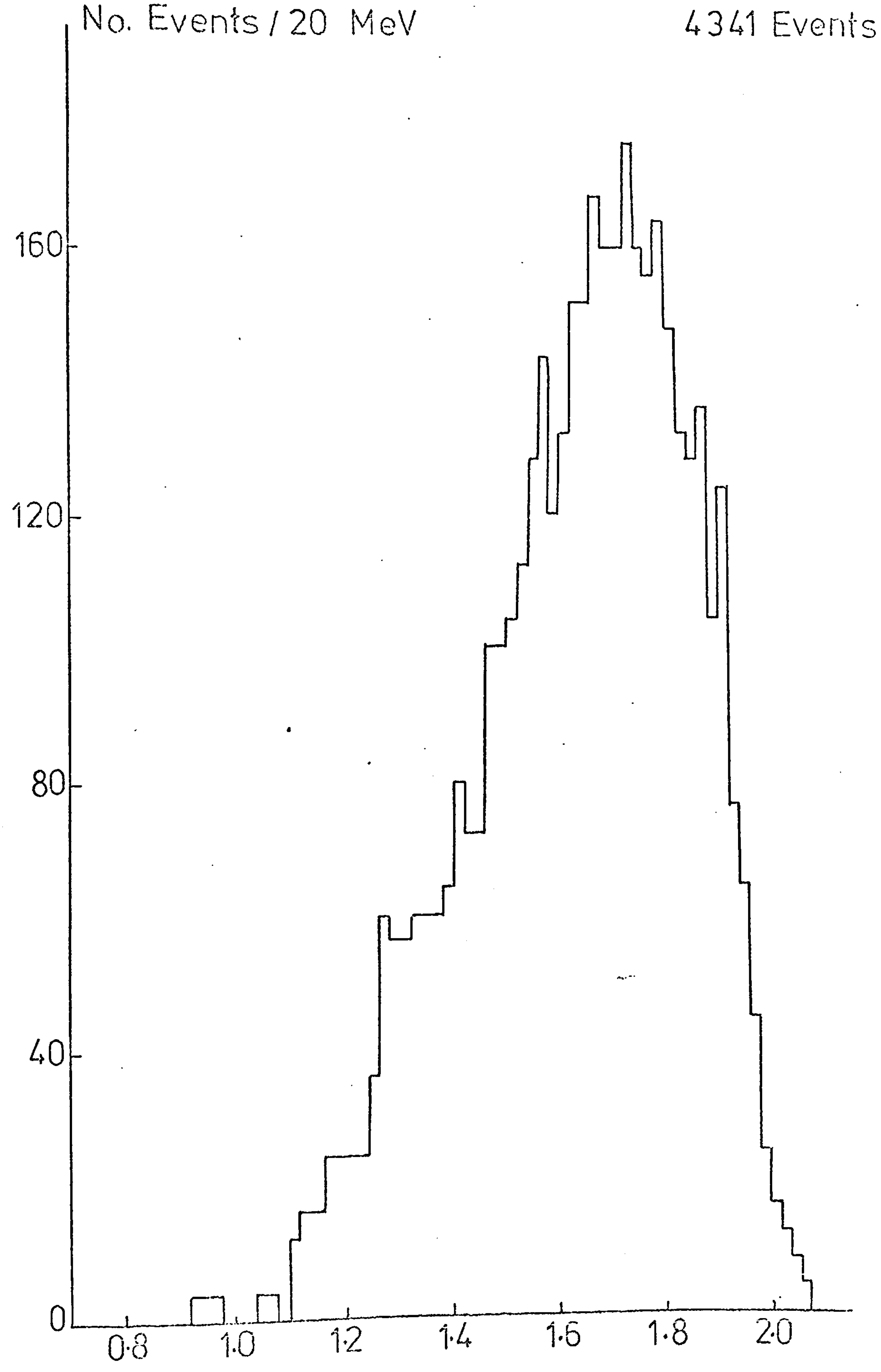
No. Events / 20 MeV
4341 Events
0
40
80
120
160
0·8
1·0
1·2
1·4
1·6
1·8
2·0
$M_{4\pi}$ GeV/c²

Fig. 6.1

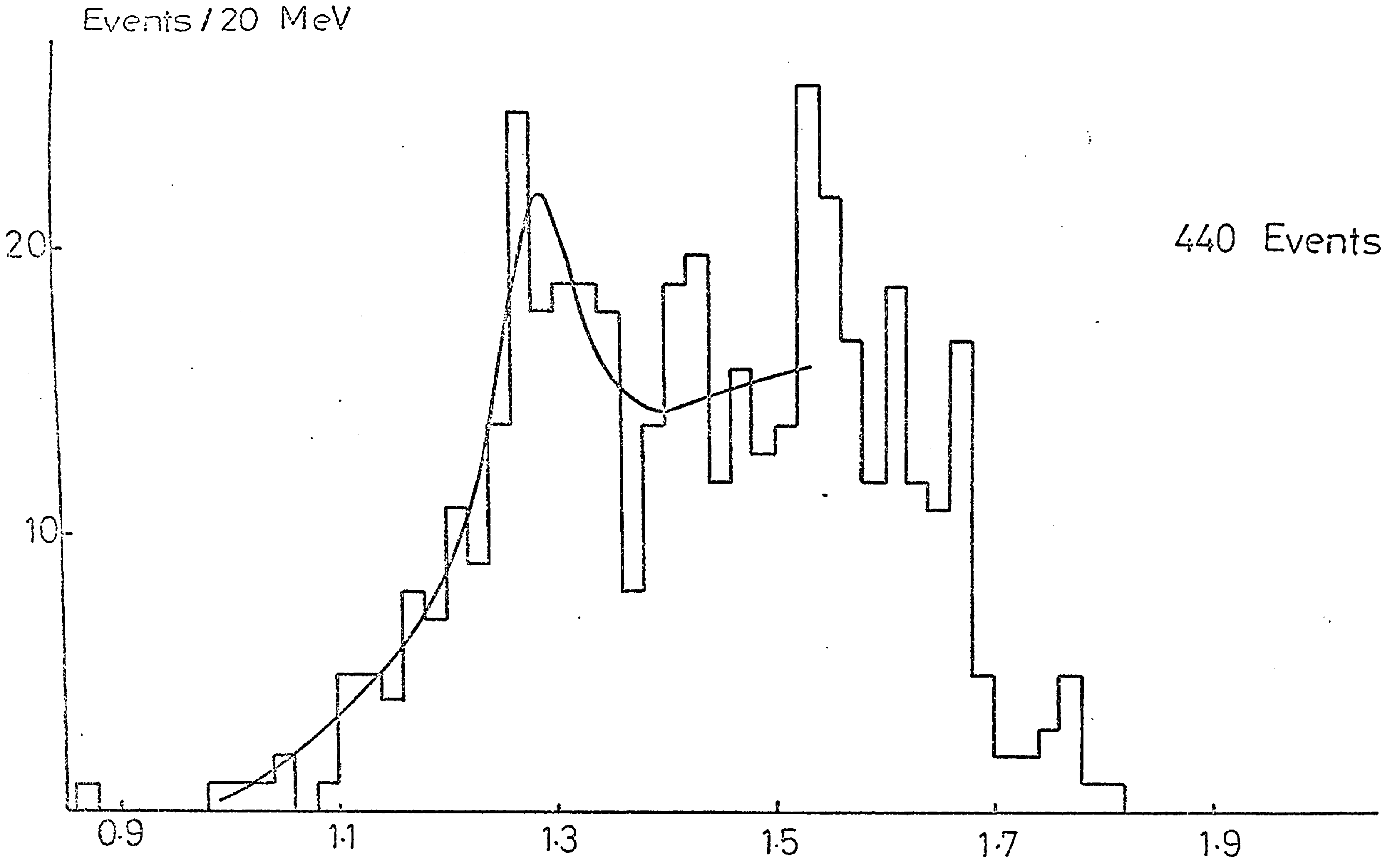

Fig. 6.2

reduce the non-resonant background in the f^o mass region. We have found it difficult to describe this spectrum by a simple polynomial shape and have consequently made a fit using a non-relativistic Breit-Wigner for the f^o together with a polynomial background. Fitted values for the f^o of $M = 1.285 \pm 0.012$ GeV/c^2 and $\Gamma = 0.089 \pm 0.031$ GeV/c^2 are obtained. These compare well with fitted values of the f^o in the two pion spectrum from this experiment and Particle Data Book values [Ref. 3.]

From the four pion fit, 80 ± 15 events are estimated above background corresponding to a cross section of $9.2. \pm 1.8$ μb and an f^o branching ratio of

$$\frac{\Gamma(f^o \to \pi^+\pi^+\pi^-\pi^-)}{\Gamma(f^o \to \pi^+\pi^-)} = (3.7 \pm 0.9) \times 10^{-2}$$

We note that the results of the fit are insensitive to the form of the Breit-Wigner used.

We have compared the differential cross sections of the f^o seen in reactions (1) and (2) and also verified that the four pion resonance is compatible with spin 2. Defining the f^o enhancement region to be

$$1.2 < M_{4\pi} < 1.34 \qquad \text{GeV}/c^2$$

for $|t| < 0.3$ (GeV/c)^2, we consider the 115 events (of which about 60 are background) within this region.

The differential cross section in the f^o region has been fitted to a curve of the form $A\,e^{bt}$ in the interval $0.06 < |t| < 0.35$ (GeV/c)^2 giving $b = 8.28 \pm 0.14$ (GeV/c)$^{-2}$ for reaction (1) and $b = 9.0 \pm 1.3$ (GeV/c)$^{-2}$

for reaction (2). The exponents are in good agreement.

For comparison we have studied the higher mass region.

$1.34 < M_{4\pi} < 1.5 \quad \mathrm{GeV}/c^2$

This is significantly less peripheral with the fit in the interval $0.18 < |t| < 0.42\ (\mathrm{GeV}/c)^2$ giving $b = 4.3 \pm 1.1\ (\mathrm{GeV}/c)^{-2}$. Unfortunately, the mass region below the enhancement contains too few events with which to make a comparison.

In Fig. 6.3. is shown the distribution in cos θ_{++} defined as the cosine of the angle between the incoming π^+ and the outgoing $\pi^+\pi^+$ system calculated in the four pion rest frame. The $\pi^+\pi^+$ direction is taken as an approximate analyser of the angular momentum states of the f^0 region. As we have a four object state it is not clear what sort of analyser should be used to determine the angular momentum composition. However, the $\pi^+\pi^+$ system contains no known definite spin behaviour. Therefore, by taking the $\pi^+\pi^+$ direction as analyser we are essentially measuring the relative angular momentum between the $\pi^+\pi^+$ and $\pi^-\pi^-$ systems which, if of higher spin, is an indication that the total four pion state is of high spin also.

Expanding the distribution in cos θ_{++} in the form

$$W(\theta_{++}) = \sum_L \langle Y_0^L \rangle \, Y_0^L(\theta_{++})$$

we observe that the only significant moments, $\langle Y_0^L \rangle$, are those with $L \leqslant 4$. The normalised spherical harmonic moments for this distribution are

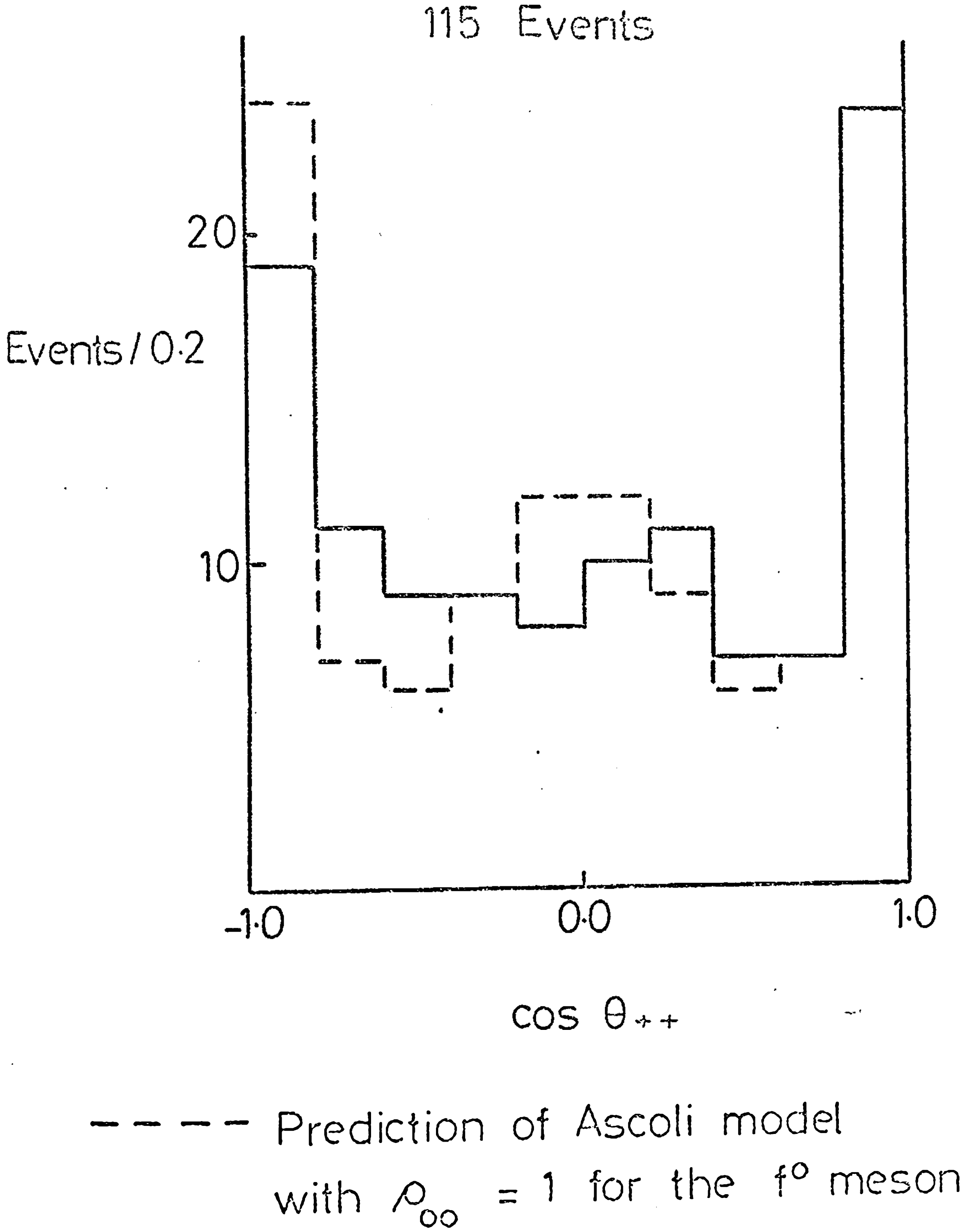
115 Events
Events / 0·2
20
10
-1·0
0·0
1·0
cos θ₊₊
- - - - Prediction of Ascoli model
with ρ₀₀ = 1 for the f° meson

Fig. 6.3

$\langle Y^2_0 \rangle = 0.098 \pm 0.032$, $\langle Y^4_0 \rangle = 0.077 \pm 0.028$

implying the existence of an object with $L \geqslant 2$.

Almost identical spherical harmonic moments are obtained in the higher mass region

$$1.34 < M_{4\pi} < 1.5 \quad \mathrm{GeV}/c^2$$

This could be owing to several things. It is possible that the $\pi^+\pi^+$ direction is a poor analyser of the four pion system and the method is insensitive to changes in angular momentum behaviour. Alternatively it is possible that the background is composed in a similar way to the enhancement, or that more spin 2 enters the background as we increase in four pion mass. It is somewhat difficult to distinguish between these possible effects.

In Figs 6.4 a, b and c we show the mass distributions in (a) the highest $\pi^+\pi^-$ combination, (b) the $\pi^+\pi^+$ plus $\pi^-\pi^-$ combinations, and (c) the three pion combinations. Superimposed on each graph are the predictions of the simple $f^o \rightarrow \rho\rho$ model proposed by Ascoli et al and the model by Banyai and Rittenberg [Ref. 45] based on chiral dynamics. Our data would appear to be consistent with the $\rho\rho$ model rather than the model of Banyai and Rittenberg.

To summarise therefore, we find in reaction (2) evidence for the four charged pion decay mode of the f^o meson with a branching ratio

$$\frac{\Gamma(f^o \rightarrow \pi^+\pi^+\pi^-\pi^-)}{\Gamma(f^o \rightarrow \pi^+\pi^-)} = (3.7 \pm 0.9) \times 10^{-2}$$

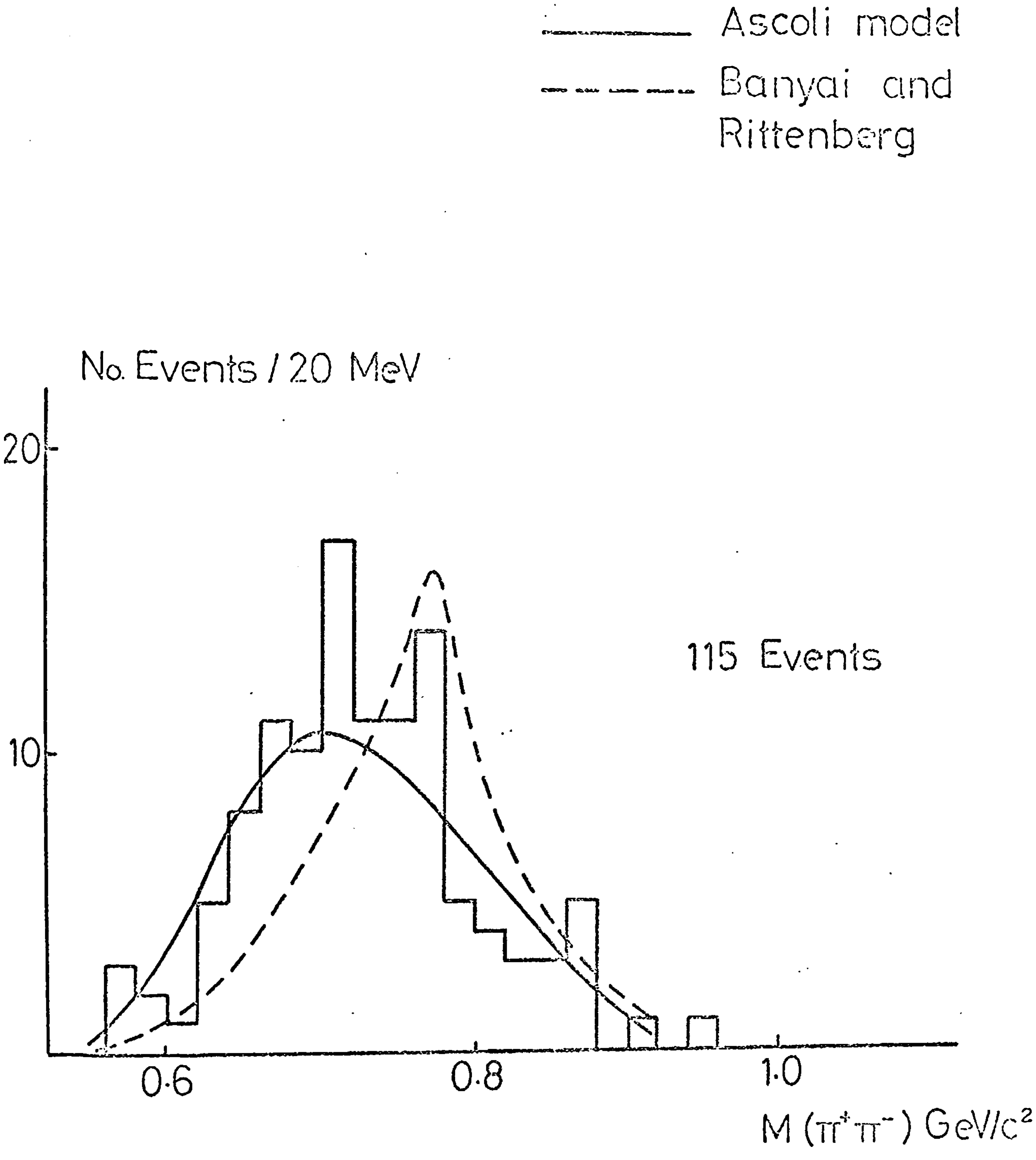
Ascoli model
Banyai and Rittenberg
No. Events / 20 MeV
20
10
115 Events
0·6
0·8
1·0
M ($\pi^+\pi^-$) GeV/c^2

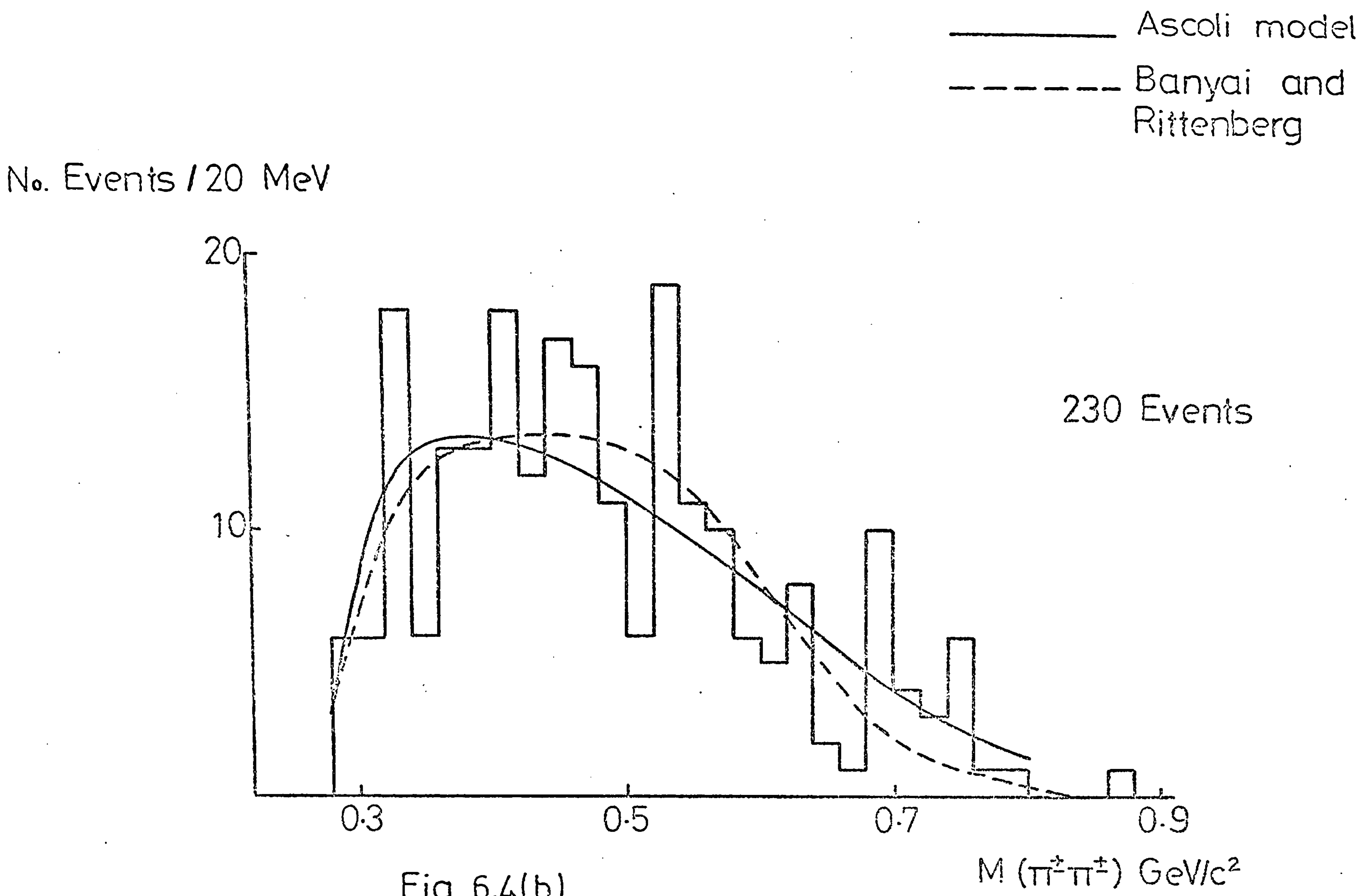
Ascoli model
Banyai and Rittenberg
No. Events / 20 MeV
20
10
230 Events
0·3
0·5
0·7
0·9
$M(\pi^{\pm}\pi^{\pm})$ GeV/c²

Fig. 6.4(b)

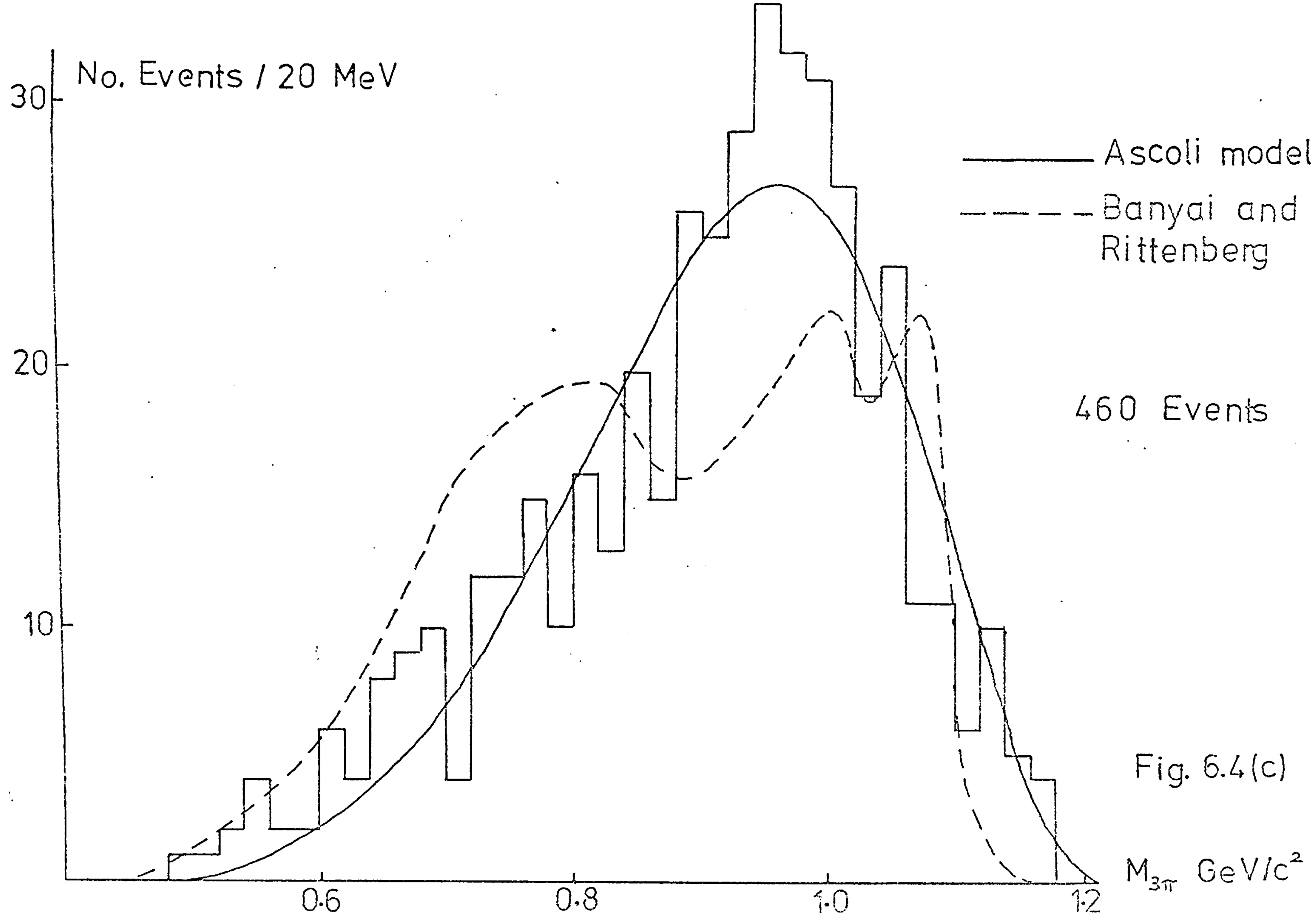

No. Events / 20 MeV
30
20
10
0.6
0.8
1.0
1.2
$M_{3\pi}$ GeV/c^2
Ascoli model
Banyai and Rittenberg
460 Events

Fig. 6.4(c)

6.5. $f^o \rightarrow K^+K^-$

To measure the $K\bar{K}$ rate of the f^o meson we have isolated the reaction

$$\pi^+ d \longrightarrow p_s\, p\, K^+ K^- \qquad (3)$$

To determine the cross section for this reaction we have used the unfitted energy-momentum technique of Ehrlich et al [Ref. 46]. For each four prong in the experiment a figure of merit, γ , was defined

$$\gamma = \frac{1}{2}\left[\left(\frac{\Delta P_x}{\Gamma_x}\right)^2 + \left(\frac{\Delta P_Y}{\Gamma_Y}\right)^2 + \left(\frac{\Delta P_z}{\Gamma_z}\right)^2\right]^{1/2}$$

where $\Gamma x, \Gamma y, \Gamma z$ are the full-width-at-half maximum of the peaks in the distributions of the missing momentum components. A plot of γ is shown in Fig. 6.5. The large peak at low γ is owing to events with no missing momentum i.e. probable 4-c events.

We use this technique to consider events of the generic type

$$\pi^+ d \rightarrow p_s p\, X^+ X^- \qquad (4)$$

Taking all four prong events and using unfitted quantities, the value of the beam momentum is adjusted to conserve momentum exactly and energy conservation is applied to calculate M_x^2 where M_x is the mass of particle X. This distribution, shown in Fig. 6.6. for events with $\gamma < 0.5$, clearly indicates the presence of a peak at M^2_K as well as a larger peak at M_π^2.

The cross section for reaction (2) can be determined by estimating the relative number of events in the K peak with respect to the number in

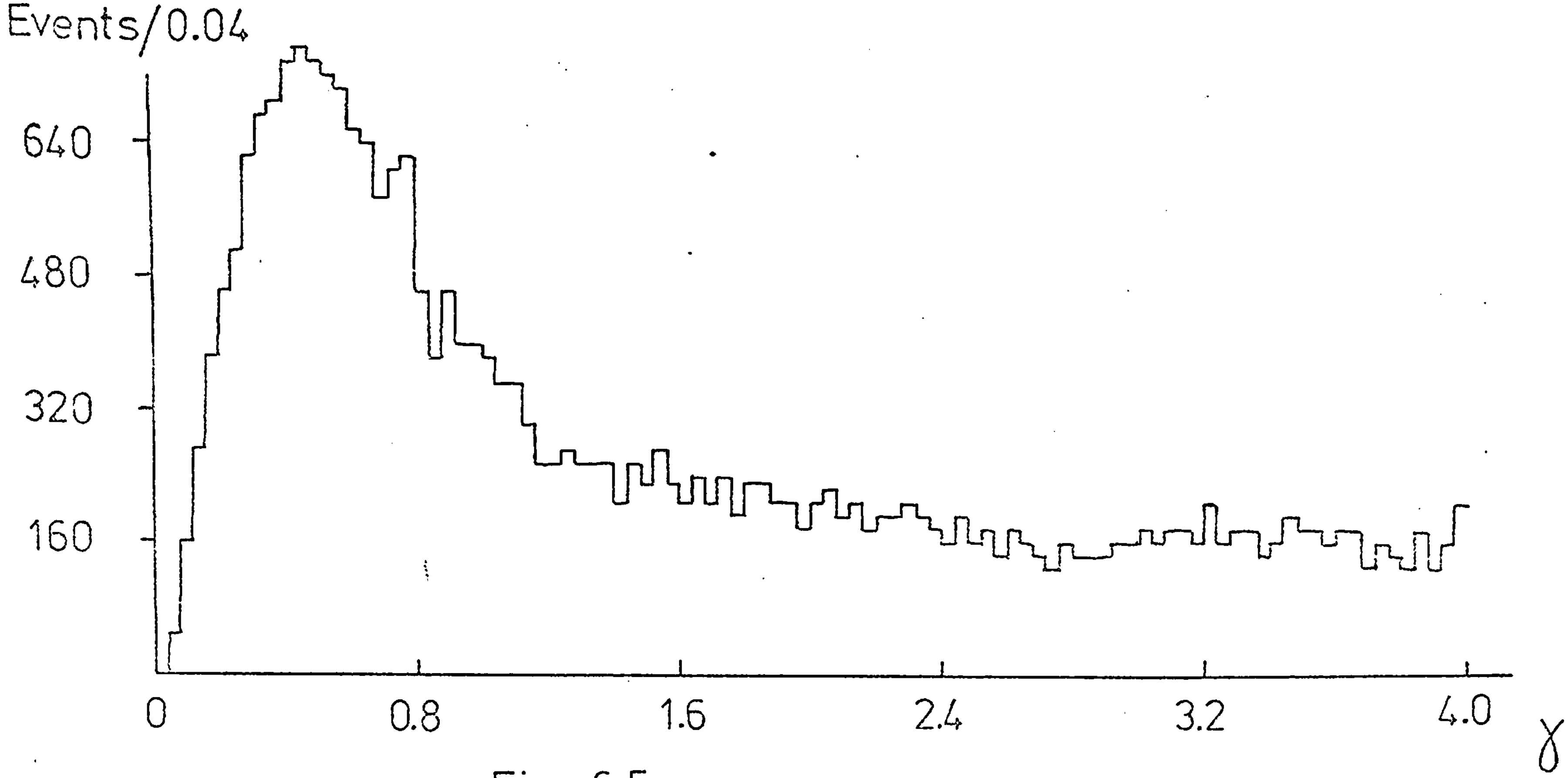

Fig. 6.5

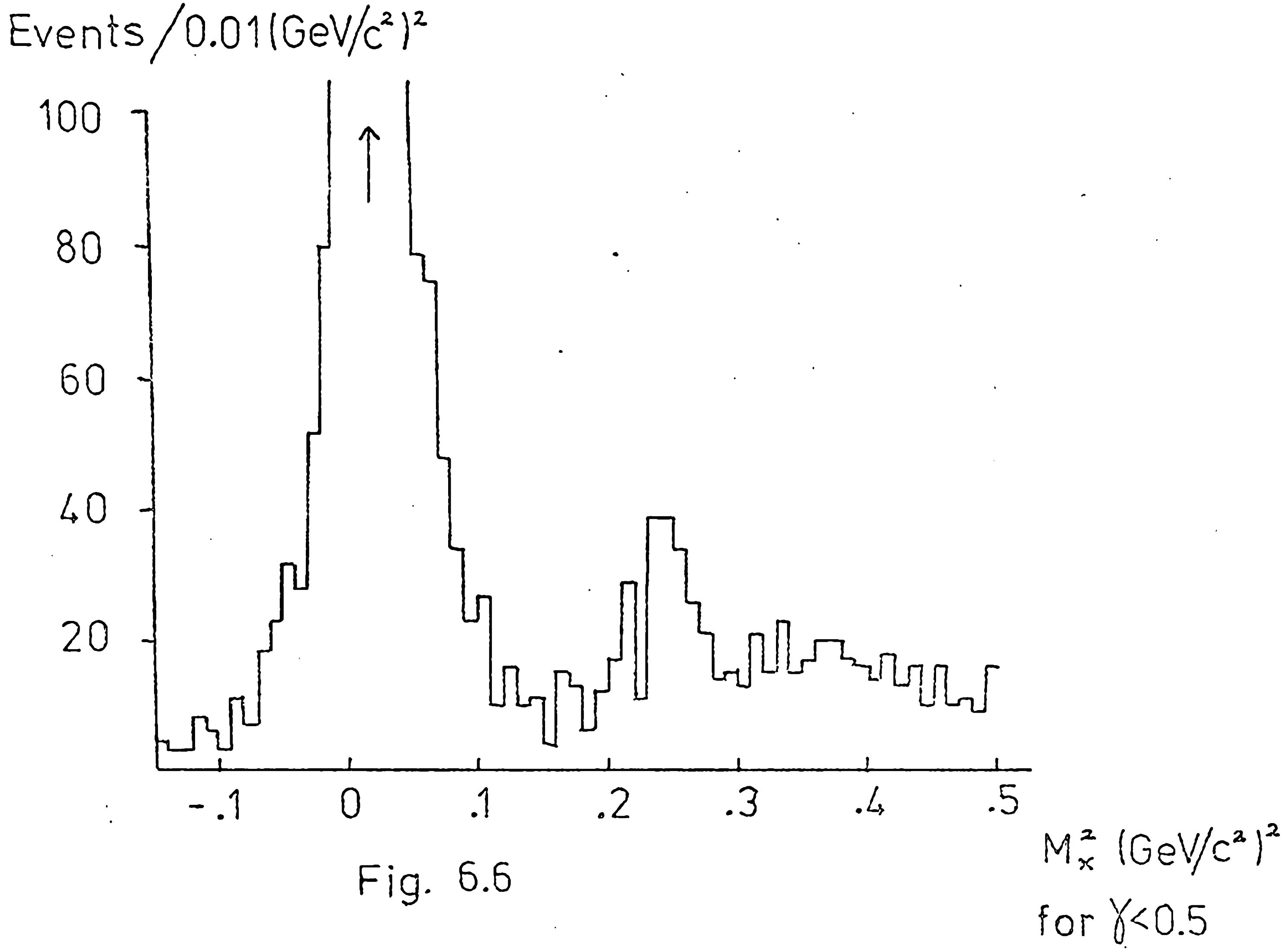

Fig. 6.6

the π peak using an eye-ball fit to the M_x^2 distribution. This relative number was found to be insensitive to the γ cut used. We then obtain

$\sigma\ K^+K^- = 0.155 \pm 0.017$ mb

For our analysis we have used 1050 fits to reaction (3). A fit to reaction (3) was considered acceptable for our analysis if it satisfied cuts identical to those for reaction (2) together with the following:-

(4) the fit to reaction (3) had a confidence level at least ten times the confidence level of the next most probable 4- constraint fit.

The 1050 events obtained in this way are about 80% of the cross section obtained from the Ehrlich technique. We have checked that these cuts do not bias the analysis of this channel.

Fig. 6.7. shows the $K^+ K^-$ mass spectrum for reaction (3). A clear signal may be seen in the f^o - A^o_2 region which is emphasised in Fig. 6.8. by taking only events with $t < 0.3\ (GeV/c)^2$. The peak corresponds to a 5 standard deviation effect. Superimposed upon Fig. 6.8. is a fit to the K^+K^- mass spectrum assuming one resonance with a spin 2 relativisitc Breit-Wigner shape together with a polynomial background. Fitted values for this peak are $M = 1.311 \pm 0.010\ GeV/c^2$ and $\Gamma = 0.102 \pm 0.030\ GeV/c^2$, giving 82 ± 15 events above background. Taking a non-relativistic Breit-Wigner gives a larger width (0.160 GeV/c^2) and a worse fit.

If we can assume that this peak is all f^o then we obtain a branching ratio

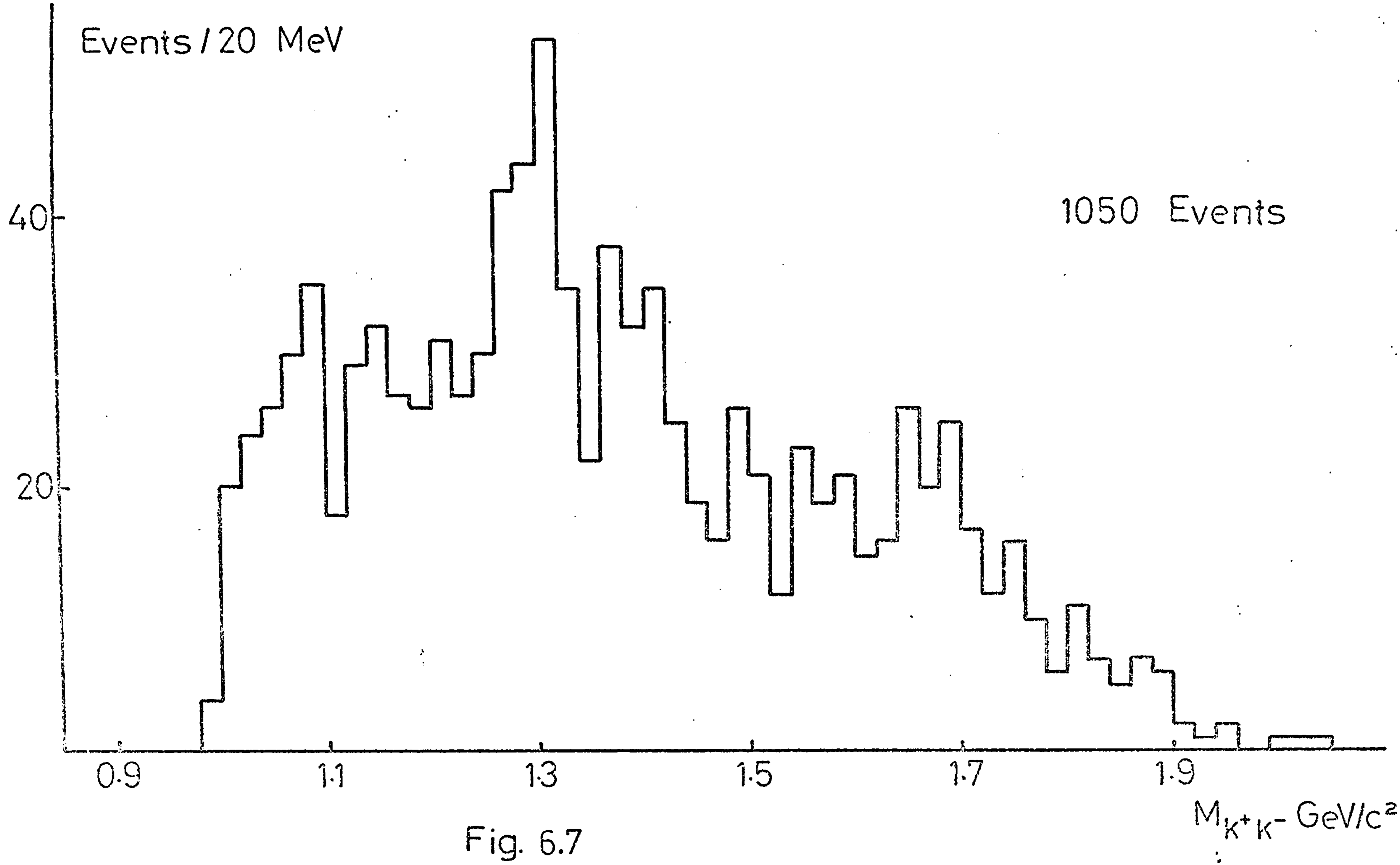

Fig. 6.7

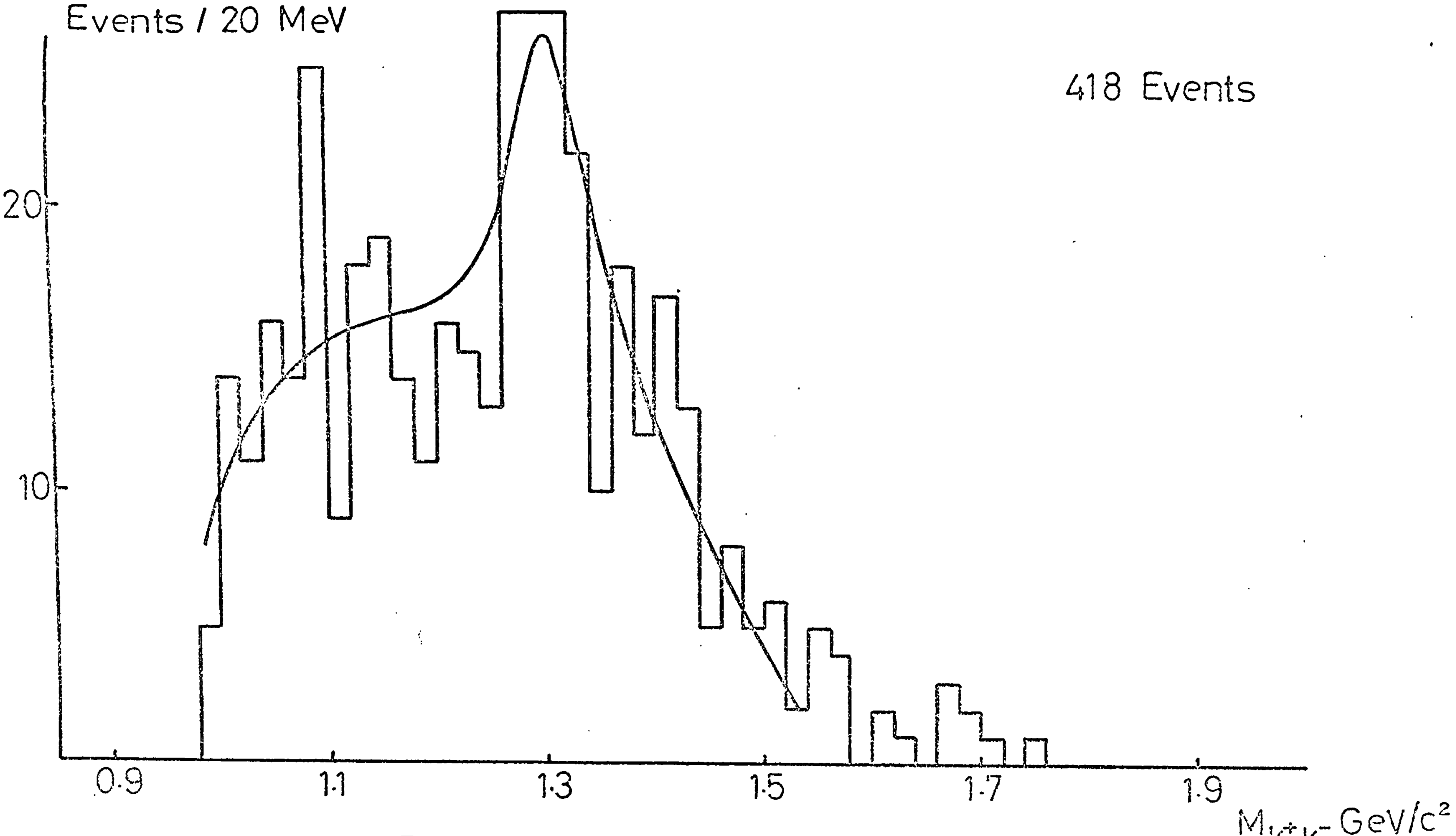

Fig. 6.8

$$\frac{\Gamma(f^o \to K\bar{K})}{\Gamma(f^o \to \pi\pi)} = \frac{4}{3} \qquad \frac{\Gamma(f^o \to K^+K^-)}{\Gamma(f^o \to \pi^+\pi^-)} = (6.5 \pm 1.5) \times 10^{-2}$$

No other resonance production is observed within the $K^+ K^-$ spectrum.

The K^+K^- differential cross section and decay angular distribution may be investigated within the f^o - $A_2{}^o$ region.

$$1.2 < M_{K^+K^-} < 1.34 \quad \text{GeV}/c^2$$

This region contains 147 events of which about 100 are background. The differential cross section in this region has been fitted to a curve of the form $A e^{bt}$ for the interval $0.06 < |t| < 0.35$ $(\text{GeV}/c)^2$ giving a value $b = 8.3 \pm 1.0$ $(\text{GeV}/c)^{-2}$ consistent with the shape of the differential cross section for the two and four pion decay modes of the f^o.

It is interesting, however, to observe that the peripherality of the data decreases across the K^+K^- mass spectrum. Apart from a reduction of events at low $|t|$ with increasing mass (as one would expect since t_{min} increases with increasing mass) the slope of the differential cross section decreases also. We observe:-

$b = 11.4 \pm 1.9$ $(\text{GeV}/c)^{-2}$ for $1.05 < M_{K^+K^-} < 1.2$ GeV/c^2

$b = 8.3 \pm 1.0$ $(\text{GeV}/c)^{-2}$ for $1.2 < M_{K^+K^-} < 1.34$ GeV/c^2

$b = 6.6 \pm 1.6$ $(\text{GeV}/c)^{-2}$ for $1.34 < M_{K^+K^-} < 1.5$ GeV/c^2

which implies that the background in the enhancement region has a slope very similar to that of the effect itself.

The t-channel spherical harmonic moments for the $K^+ K^-$ decay defined by

$$W(\theta, \phi) = \sum_{LM} \langle Y^L_M \rangle \, Y^L_M (\theta, \phi)$$

to the f^o meson in the total $K\bar{K}$ mass spectrum. Noting that the terms in (c) correspond to $I = 0$ and 1 production of a neutral $K\bar{K}$ system, we can write the intensity for K^+K^- using Clebsch-Gordon coefficients as

$$\frac{dN}{dm}(K^+K^-) = \frac{A^2\pi^{-1}}{4}\Big[(c_1^2+d_1^2) + r^2(c_2^2+d_2^2) + 2r\alpha(c_1c_2+d_1d_2)\cos\phi - 2r\alpha(c_1d_2-c_2d_1)\sin\phi\Big]$$

where c_i and d_i are the real and imaginary parts of the expressions $\Gamma_i^{\frac{1}{2}} b_i$ and we have the coherence factor a, where $0 \leqslant a \leqslant 1$. The $K^o\bar{K}^o$ spectrum is obtained by changing ϕ into $\phi + \pi$. By inserting various values of ϕ, a and r^2 into (d) it is possible to observe the variation of the mass at which the K^+K^- distribution peaks. A high mass peak at 1.310 GeV/c^2 is possible with the parameters $\phi = -\pi$, $a = 1$ and $r^2 = 10\%$, although we must wait until $K_s^o\bar{K}_s^o$ data becomes available before these parameters can be confirmed.

However, it is also possible to determine the A^o_2 contribution to reaction (3) by estimating the amount of A_2^o produced in the reaction

$$\pi^+ d \rightarrow p_s\, p\, \pi^+\pi^-\pi^o \qquad (6)$$

and by independently measuring the $A_2 \rightarrow K\bar{K}$ branching ratio in the charged decay mode ($A^{\pm}_2 \rightarrow K^{\pm}K^o$). [Ref. 3.] We estimate by this method that only about 7 events in the K^+K^- mass spectrum for $|t| < 0.3$ $(\mathrm{GeV}/c)^2$ can come from A^o_2 production, implying, if we may assume no $f^o - A^o_2$ interference, overwhelming f^o production in the observed peak and a branching ratio for the f^o very similar to that for the whole $f^o - A^o_2$ effect. However, as the peak centres at a higher K^+K^- mass, it would appear that some interference is present, and a study of this awaits investigation when data from reaction (5) becomes available.

This determination of the branching ratio is seen to be not incompatible with the S.U.(3) prediction of about 5%. The experimental value would have to be lowered once interference is considered if the Biswas result of near maximum interference is repeated here.

The other mass distributions from reation (3) are also of interest. The p K^+ mass spectrum is shown in Fig. 6.9 (a). Since this is an "exotic" channel ($I = 3/2$, $S = +1$) we do not expect to observe strong resonance production and this appears to be the case.

The p K^- mass spectrum is shown in Fig. 6.9. (b) . Near threshold we observe an enhancement of about 45 events above background with approximate mass and width 1520 MeV/c^2 and 20 MeV/c^2. This corresponds to the Λ(1520) (nominal mass 1518 MeV/c^2 and width 16 MeV/c^2 observed in the experiment of Garfinckel et al at 2.7 GeV/c [Ref. 47]. If we assume that the cross section for the quasi-two-body reaction.

$$\pi^+ n \rightarrow \Lambda(1520)\ K^+ \qquad (7)$$

falls as p^{-2} (the so-called Morrison's Rule for reactions involving strange particle exchange) where p is the incident laboratory momentum, and that the Λ (1520) branching fraction to $\bar{K}$ N is 0.45 [Ref. 3.], the 45 events (or 28 μb) agree exactly with the number predicted at our energy. The two low mass enhancements observed (the f^o - A^o_2 peak and the Λ (1520))are well separated on a Dalitz plot and are therefore uncorrelated. However, the background in the K^+K^- mass spectrum can be slightly reduced for study of the f^o - A^o_2 effect by subtracting the Λ(1520) events from the data.

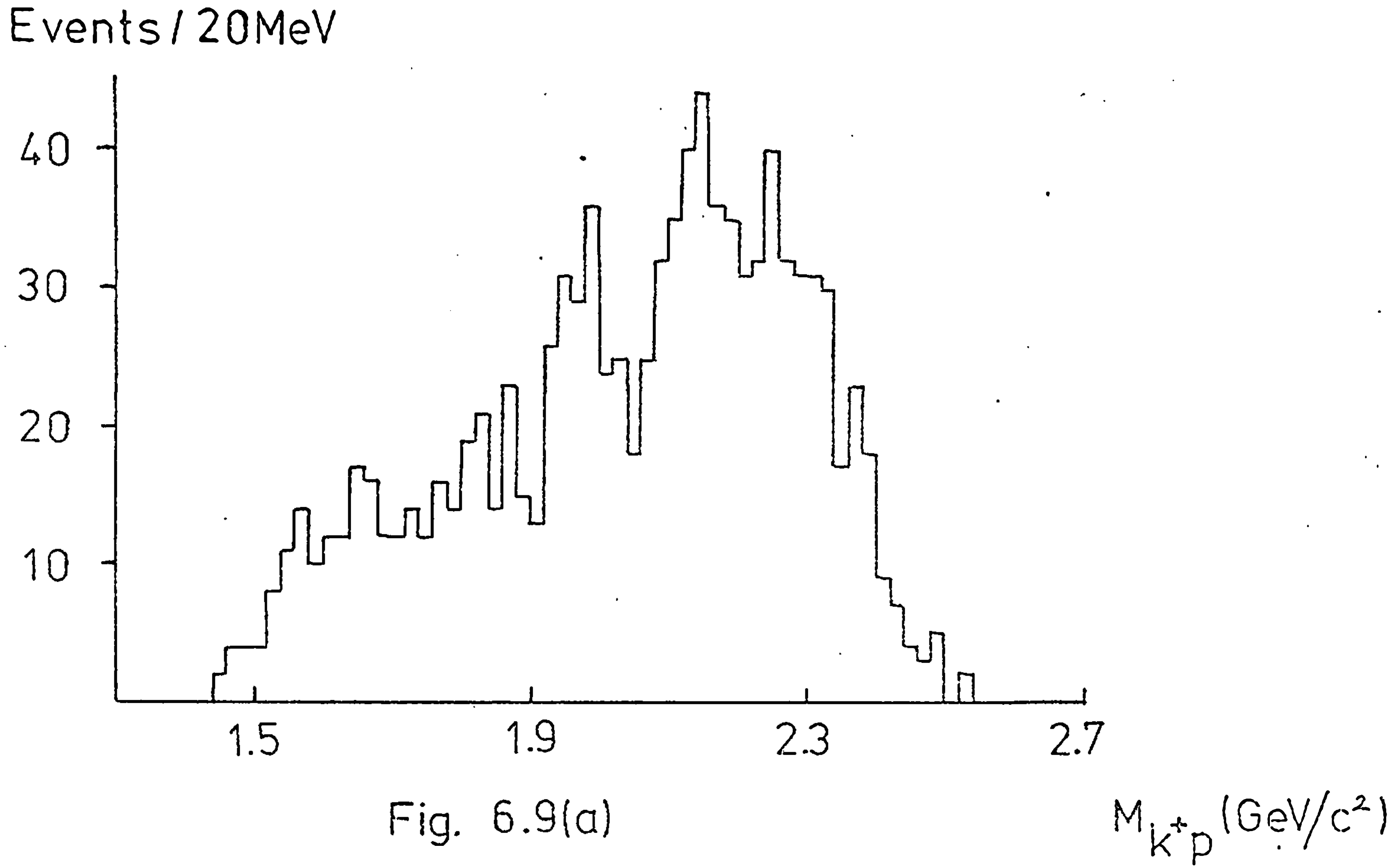

Fig. 6.9(a)

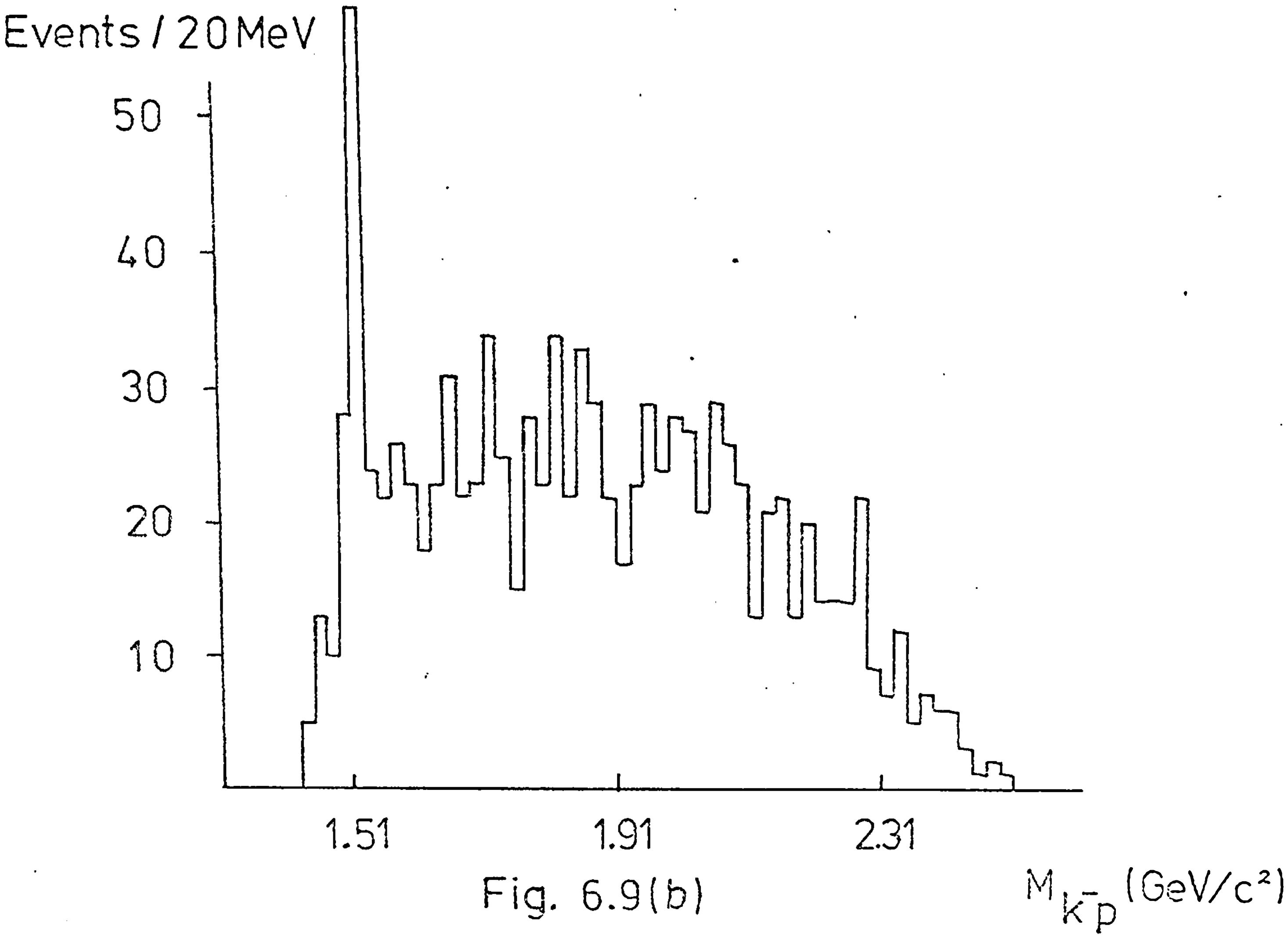

Fig. 6.9(b)

6.6. Other Possible f^o Decay Modes.

An investigation has been made of the decay of the f^o into one 1-c and several multi-neutral channels.

Fig. 6.10 shows the five pion mass spectrum from the reaction.

$$\pi^+ d \rightarrow p_s\, p\, \pi^+ \pi^+ \pi^- \pi^- \pi^o \qquad (8)$$

for events below $|t| = 0.3\ (GeV/c)^2$ in four momentum transfer squared to the five pion system. This system will include any decay

$$f^o \rightarrow \eta^o\ \pi^+ \pi^- \qquad (9)$$

and all the events in Fig. 6.10 have at least one neutral three pion combination consistent with the mass of an η^o (i.e. $M_{3\pi} < 0.6\ GeV/c)^2$. Any fit ambiguous with the 4-c fit of reaction (2) has been removed. We observe a clear $\eta^{\prime}$ (960) signal but no f^o signal. This yields an upper (two standard deviation) limit for the branching ratio $\Gamma(f^o \rightarrow \eta^o\ \pi^+\pi^-)/\Gamma(f^o \rightarrow \pi^+\pi^-)$ of 2.5% after correction for other η^o decay modes.

The reaction $\pi^+ n \rightarrow p\ \ f^o$ can possibly be observed in the multi-neutral channels

$$\pi^+ d \rightarrow p_s\, p\, M M \qquad (10)$$

$$\pi^+ d \rightarrow p_s\, p\ \pi^+ \pi^-\ M M \qquad (11)$$

$$\pi^+ d \rightarrow p_s\, p\ \pi^+ \pi^+ \pi^- \pi^-\ M M \qquad (12)$$

where the missing mass (MM) is consistent with being two (or more) π^o's. The f^o contribution to reaction (10) is predictable from the $\pi^+\pi^-$ signal observed in reaction (1). Figs. 6.11, 6.12, and 6.13 show the MM spectra for reaction (10), and the (charged pion + MM) effective mass spectra for

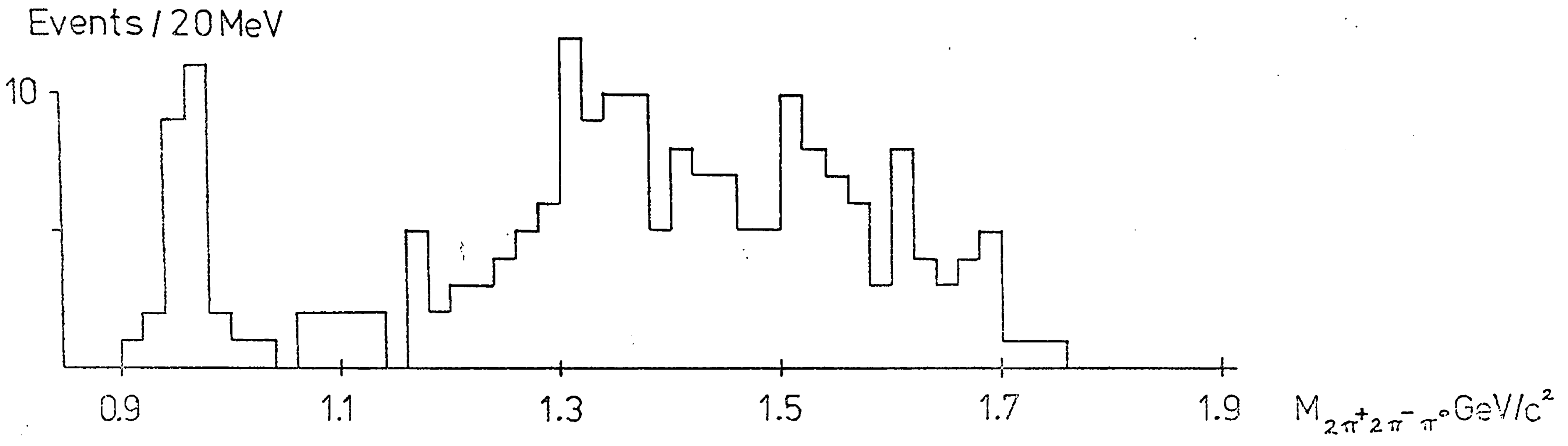

Fig. 6.10

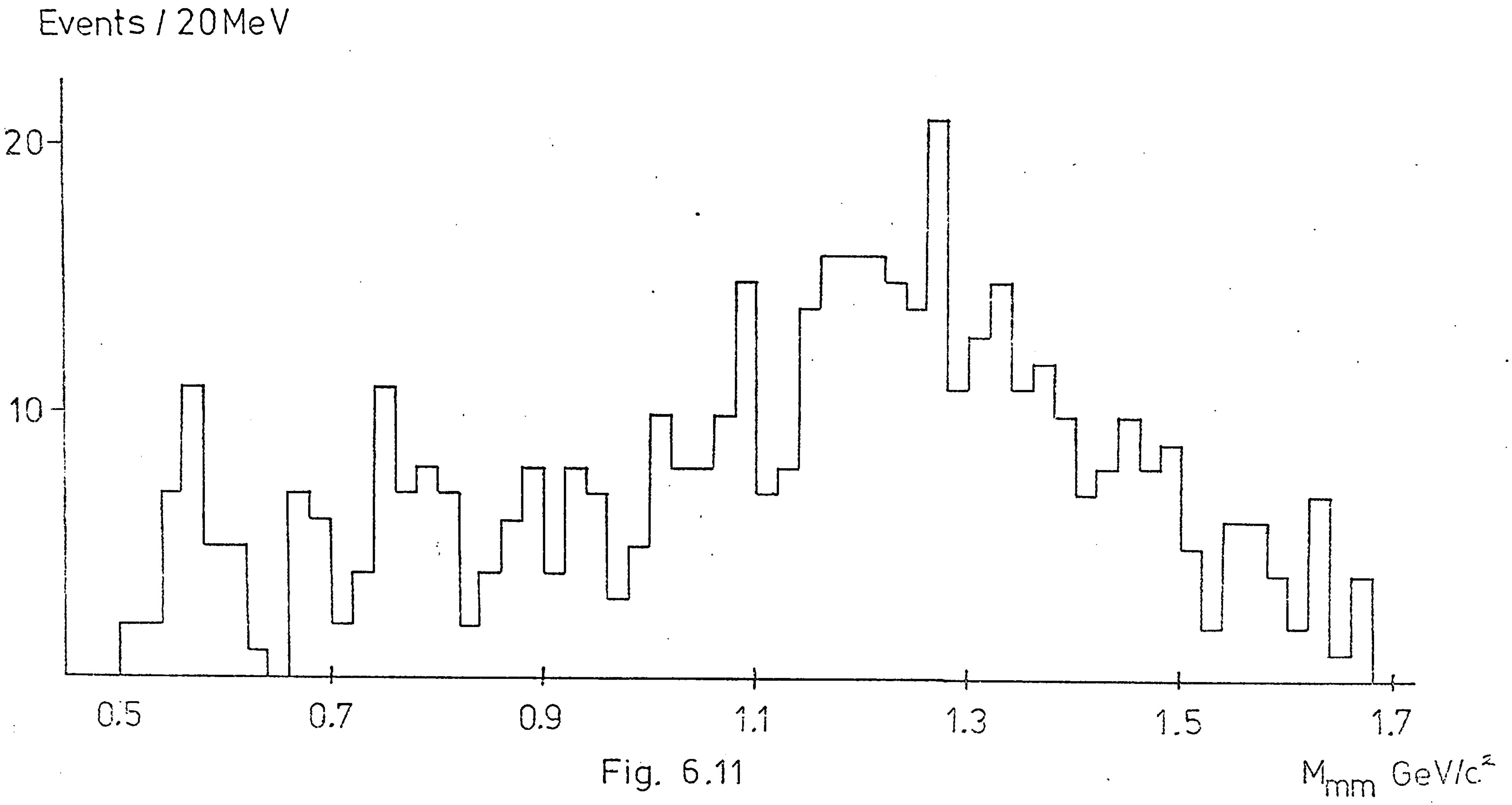

Fig. 6.11

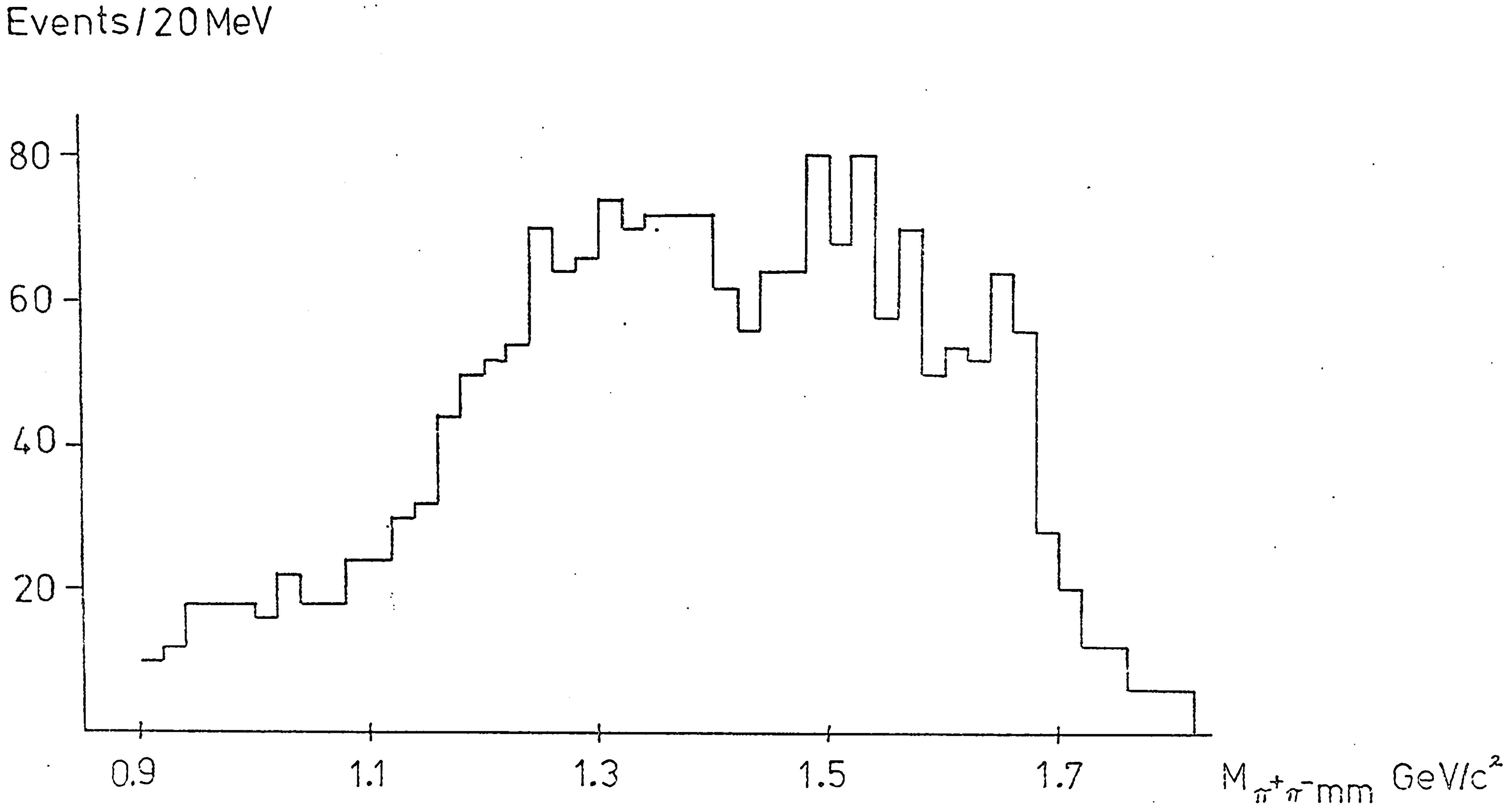

Fig. 6.12

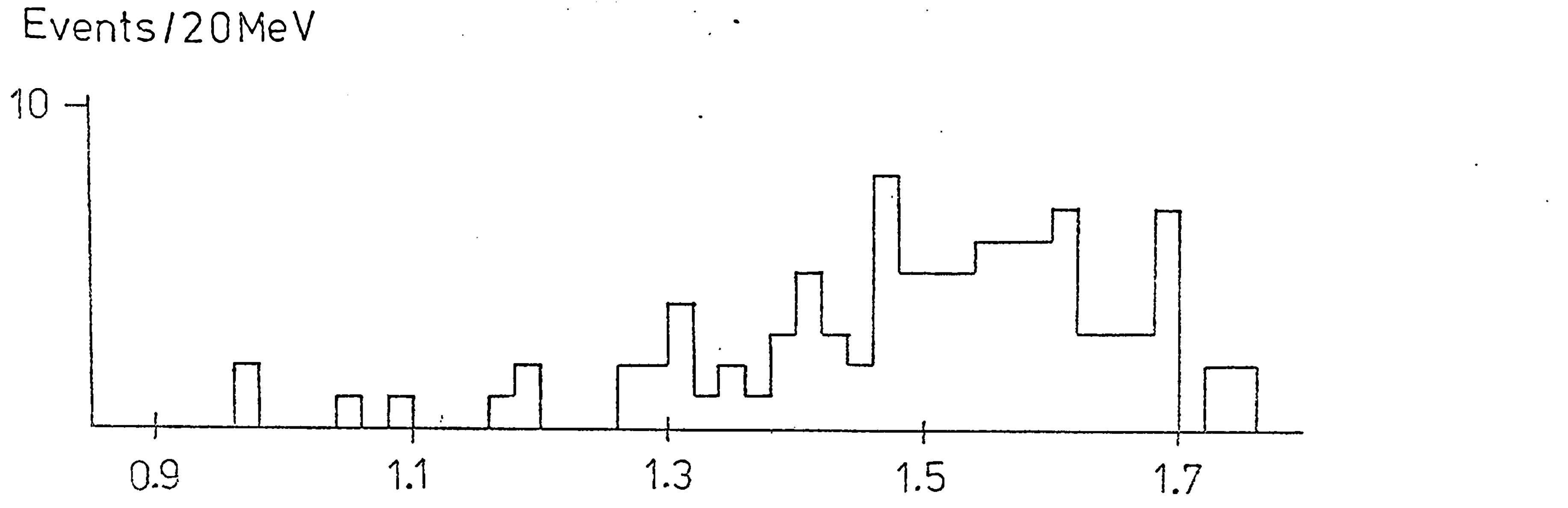

Fig. 6.13

reactions (11) and (12) respectively. Only events with $|t| < 0.3$ $(\mathrm{GeV}/c)^2$ in four momentum transfer squared to the pionic system are presented in these spectra.

Fig. 6.11 contains events from the Birmingham share of the data only. The number of events peaking at approximately the f^o mass is consistent with the number required by isospin conservation for the $I = 0$ f^o meson. It is of additional interest that no large excess of events is observed in the rho region. This implies that any strongly resonant S wave in this region is unlikely. However, any interpretation of a missing mass spectrum should be made with care. The one and two prongs which comprise reaction (10) are subject to severe scanning biases and the shape of this spectrum awaits confirmation when Rutherford Laboratory data becomes available.

The number of events in reaction (12) also show no real f^o signal and an upper limit has again been determined for the branching ratio $\Gamma(f^o \rightarrow 2\pi^+ 2\pi^- 2\pi^o) / \Gamma(f^o \rightarrow \pi^+ \pi^-)$ of 1/4%. Fig. 6.13 contains fits which are not ambiguous with either a 4-c fit or a 1-c fit with a kinematic probability larger than 1%. This channel, which corresponds to decays of the type $\eta^o \bar{\eta}^o$ etc. is seen to have a very low cross section.

The only mass spectrum among the multi-neutral channels which shows a possible enhancement in the f^o region is the $\pi^+\pi^-$ MM distribution of Fig. 6.12. Again a multi-neutral fit was considered for plotting only if there was no ambiguous 4-c fit and no ambiguous 1-c fit with kinematic probability larger than 1%. If the f^o decays to four pions completely via rho-rho then we should expect 160 ± 30 events to be observed in this enhancement. Clearly this is quite possible with a suitable choice of background. However, the enhancement of Fig. 6.12. is almost twice as wide as one would expect for f^0 decay and overlaps into the A^0_2 region. A^0_2 contribution to this spectrum is possible if there is a decay $A^0_2 \rightarrow \pi^+\pi^- \; 3\,\pi^0$. Consequently this enhancement cannot really be used as proof of the Ascoli $f^0 \rightarrow \rho\rho$ model.

APPENDIX 1

Form Factor Fit to the $\pi\pi$ Spectrum

To try to understand the main features of the $\pi\pi$ spectrum, fits were made to the $\pi\pi$ mass spectrum and t distributions. Among the methods used, an attempt was made to fit the $\pi\pi$ mass and t distributions simultaneously, using the Chew-Low formula [Ref 21.] to relate the experimental mass and t distributions to the $\pi\pi$ scattering cross section. To convert this cross section from its on-shell (assumed Breit-Wigner) form to its off-shell shape, Benecke-Durr [Ref. 48] form factors were employed using the parameters found by Wolf [Ref. 49] in $\pi^- p$ and $\pi^+ p$ experiments.

The $\pi\pi$ mass and t distributions are related to the off-shell $\pi\pi$ cross section, $\sigma(m,t)$, via the Chew-Low formula:-

$$\frac{d^2\sigma}{d\,|t|\,dm} = \frac{1}{4\pi^3 p^2 s}\; m^2 q_t\; \sigma(m,t)\; \frac{G^2(t)}{(t-\mu^2)^2}\; F^2_{NN\pi}(t)$$

where p is the centre of mass momentum in the initial state, $F_{NN\pi}$ is the scattering amplitude at the $NN\pi$ vertex, G (t) is a correction to the pion propagator and q_t is the momentum of the exchanged pion in the $\pi\pi$ rest frame. Benecke-Durr form factors, to be employed in this fit, are sufficiently adequate that the factor G(t), which slightly reduces the differential cross section at high $|t|$ may be neglected.

Previous models which attempted to describe these distributions have been unsuccessful. In the Pole Approximation, the off-shell cross section, $\sigma(m,t)$, is made equal to its on-shell value, $\sigma(m)$, and in the Born

Approximation for the decay of a state of spin L we obtain the relation:-

$$q_t \quad \sigma^L(m,t) = \left[\frac{q_t}{q}\right]^{2L} q \quad \sigma^L \ (m)$$

where q is the momentum of the final state pions in the $\pi\pi$ rest frame. However, neither of these models leads to an adequate description of the differential cross section, the data being much more peripheral.

Benecke and Durr assumed that the elastic scattering of particles 'a' and 'b' via

$$a + b \longrightarrow a' + b'$$

can be described by the exchange of a scalar particle 'x' with mass m_x. Then, in going off-shell with one of the particles, say particle 'a', the relation between the off-shell and the on-shell scattering amplitude as a function of the off-shell mass of 'a' is obtained. As a result, the factor $\left(\frac{qt}{q}\right)^{2L}$ in the Born Approximation is replaced by the functions

$$\frac{U_{L}(q_t R)}{U_L \ (q\,R)}$$

where $1/m_x$ has been put equal to R and U_L (r) is defined by:-

$$U_L \ (r) = \frac{1}{2r^2} \quad Q_L \left[1 + \frac{1}{2\,r^2} \right]$$

where the $Q_L(z)$ are Legendre Functions of the Second Kind. The functions U_L (r) have the following general properties:-

$$U_L \ (r) \sim r^{2L} \qquad \text{for } r \ll 1$$

$$U_L \ (r) \sim \frac{1}{r^2} \quad \ln\,(4\,r^2) \ \text{ for } r \gg 1$$

Hence, for small values of $|t|$ the off-shell cross sections have the behaviour given by the Born Approximation. For larger $|t|$ values they behave like $1/t^2$ in contrast to the Born Approximation.

For each partial wave L we require a separate parameter R_L to describe the differential cross section behaviour. The factor $|F_{NN\pi}(t)|^2$ is given, after Durr-Pilkuhn [Ref. 50] by:-

$$|F_{NN\pi}(t)|^2 = (-t) \frac{1 + R_N^2 Q^2}{1 + R_N^2 Q_t^2} \pi^2 g^2$$

where g^2, the $NN\pi$ coupling constant, equals 29.2 for $\pi^\pm$ and R_N is another parameter, with

$$Q^2 = - \frac{\mu^2 (4 M_N^2 - \mu^2)}{4 M_N^2} \quad \text{and} \quad Q_t^2 = \frac{-t\,(4 M_N^2 - t)}{4 M_N^2}$$

with M_N the nucleon mass. A list of the Wolf constants is given in Table Al.1.

About 10,000 events of the total data were used for the fit between 0.5 and 1.5 GeV/c^2 in $\pi\pi$ mass, and for $|t|$ less than 0.3 $(\mathrm{GeV}/c)^2$. We considered the data to be composed of three resonances with different J^P; namely, the rho (1^-), the f (2^+) and an I = 0 S wave. No I = 2 S or D wave was included. We then obtain:-

$$\sigma(m, t) = \sum_L \frac{q}{q_t} \frac{U_L(q_t R_L)}{U_L(q R_L)} \sigma^L(m)$$

where for the $\sigma^L(m)$ we use the relativistic Breit-Wigner shape

$$\sigma^L(m) = 4\pi ƛ^2 C^I_L (2L + 1) \frac{(m_L \Gamma_L)^2}{(m_L^2 - m^2) + (m_L \Gamma_L)^2}$$

Table A1.1

Wolf (Ref 49) Parameters for Benecke-Durr Fit

	Vertex	R (GeV^{-1})
R_ρ	$\rho\pi\pi$	2.31 ± 0.19
R_f	$f\pi\pi$	3.23 ± 1.46
R_{oo}	$(\pi\pi)^{I=0}(\pi\pi)$	0.01
R_N	$NN\pi$	2.86 ± 0.08

where $\Gamma_L = \Gamma^o{}_L \left(\frac{q}{q_L}\right)^{2L+1} \frac{m}{m_L}$

and q_L (m_L) is the value of q (m) at the resonance centre, and $C^I{}_L$ the relevant Clebsch-Gordon coefficient for each partial wave. A good fit was obtained using the Particle Data Group [Ref. 3.] values of:-

$m_1 = 0.765$ $\Gamma^o{}_1 = 0,125$

$m_2 = 1.269$ $\Gamma^o{}_2 = 0.154$ GeV/c^2

The S and P waves were assumed elastic throughout the whole spectrum while the D wave was assumed to have the elasticity found by Ch [Ref. 51] in his phase shift analysis of the $\pi\pi$ spectrum.

The parameters of the S wave were allowed to vary during the fit and were found to best fit the data with mass and width 790 and 510 MeV/c^2 respectively. The broad shape of the S wave was found to be not too dependent on the P and D wave parameters. The resulting fit is shown in Figs. Al. 1 (a) and (b). The differential cross section at low $|t|$ was reduced in accordance with the Pauli Principle and a scanning bias, discussed in Chapter 3.

This result, similar to that found by Bartsch et at [Ref. 52] can be attributed to the S wave ε meson or to a general background effect. Bartsch preferred the former conclusion. As the assumptions involved in this fit are somewhat crude, and omit several known effects (e. g. I spin 2 waves, S^* resonance etc.) , any specific interpretation is unwise. However, it is useful to underline the three dominant effects. Namely, spin 1 rho and spin 2 f production, together with a large (presumably S wave) background effect.

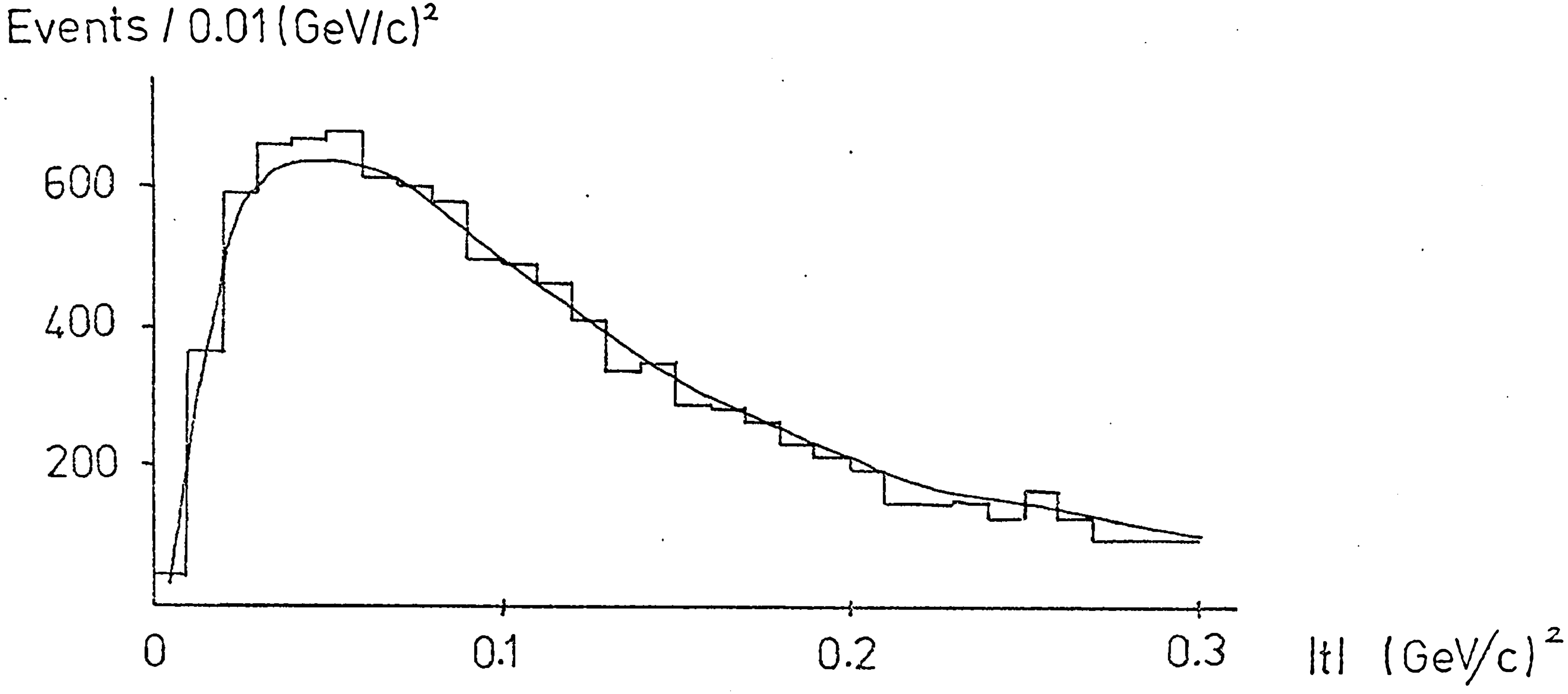

Fig. A1.1 (a) |t| Distribution for Chew-Low fit.

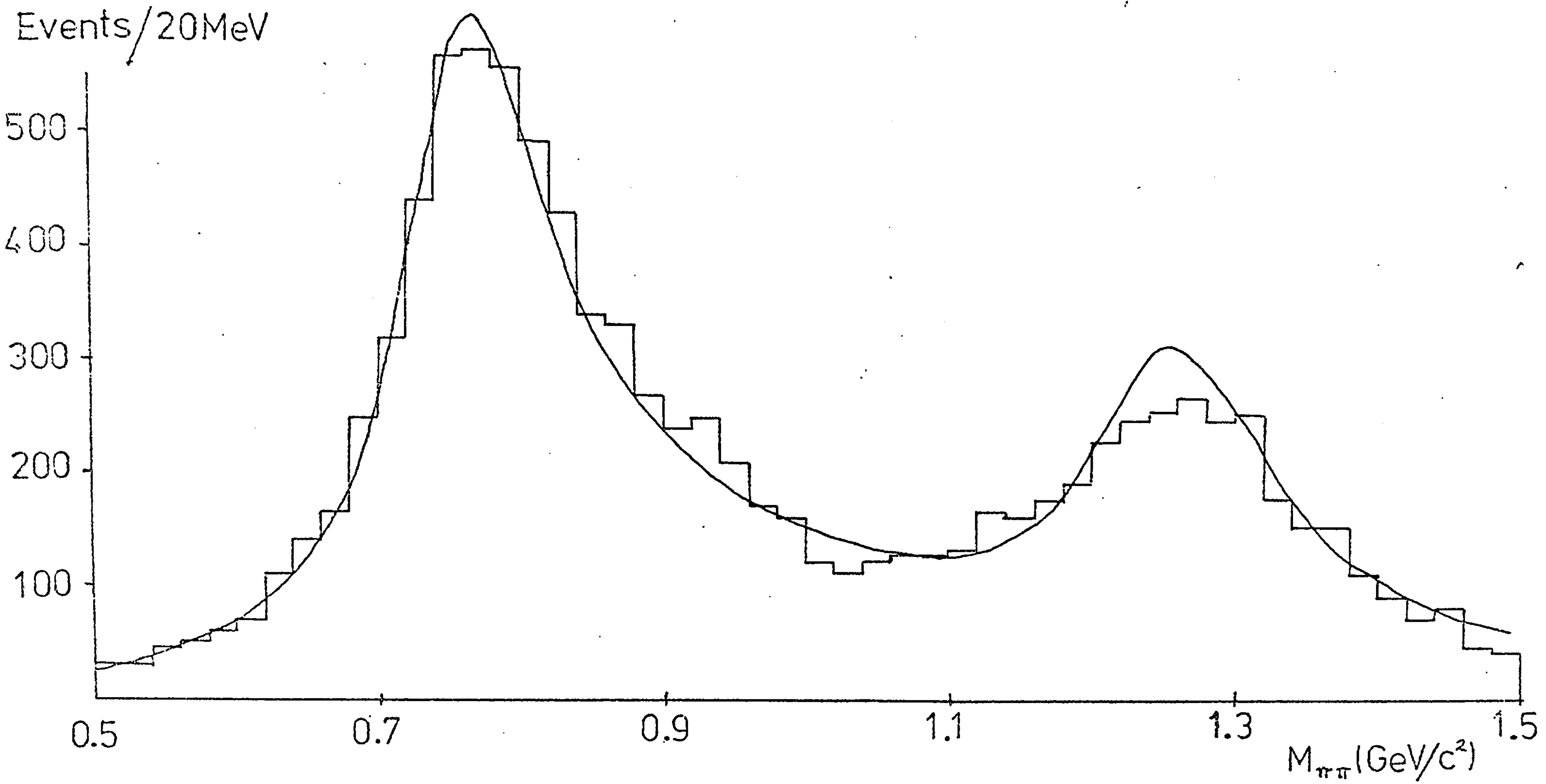

Fig. Al.1. (b) M ππ Distributon for Chew-Low fit.

APPENDIX 2

Solution of Amplitude Analysis Equations

The system of equations described in Chapter 5 by equations 2(a) to (f) may be re-written generally:-

$$A_1 = x_1^2 + x_2^2 + (1 + r^2)\, x_3^2 + (1 + r^2)\, x_4^2 \tag{1}$$

$$A_2 = (1 + r^2)\, x_3^2 - \tfrac{1}{2} x_1^2 - \tfrac{1}{2} x_2^2 \tag{2}$$

$$A_3 = \tfrac{1}{2} x_1^2 - \tfrac{1}{2} x_2^2 \tag{3}$$

$$A_4 = \frac{1}{\sqrt{2}}\, x_2 x_3 \cos x_5 \tag{4}$$

$$A_5 = (1 + r^2)\, x_3 x_4 \cos x_6 \tag{5}$$

$$A_6 = \frac{1}{\sqrt{2}}\, x_2 x_4 \cos (x_5 - x_6) \tag{6}$$

where the A_i for i = 1 to 6 are known constants (density matrix elements) and the x_i for i = 1 to 6 are parameters. The system of 6 equations is exactly constrained. The following identities have been made:-

$x_1 = |M_+|$

$x_2 = |M_-|$

$x_3 = |M_o|$

$x_4 = |M_s|$

$x_5 = \theta_{10}^{11}$

$x_6 = \theta_{00}^{10}$

and $r = 0$ if the analysis is performed in the t-channel and $\dfrac{t_{min}}{t - t_{min}}$ in the s-channel.

Combining (2) and (3) we obtain

$$x_2^2 = (1 + r^2)\, x_3^2 - A_2 - A_3 \tag{7}$$

Combining (2) , (3) and (4) we obtain

$$\cos x_5 = \frac{\sqrt{2}\, A_4}{[(1 + r^2)\, x_3^2 - A_2 - A_3]^{\frac{1}{2}}\, x_3} \tag{8}$$

Combining (1) and (2) we obtain

$$x_4^2 = \frac{1}{(1 + r^2)^2} \left[A_1 + 2\, A_2 - 3\,(1 + r^2)\, x_3^2 \right] \tag{9}$$

Combining (1), (2) and (5) we obtain

$$\cos x_6 = \frac{A_5}{(1 + r^2)^{\frac{1}{2}} [A_1 + 2A_2 - 3\,(1 + r^2)\, x_3^2]^{\frac{1}{2}} x_3} \tag{10}$$

The cosine term in equation (6) is expanded

$$\cos(x_5 - x_6) = \cos x_5 \cos x_6 \pm \sqrt{1 - \cos^2 x_5}\,\sqrt{1 - \cos^2 x_6} \tag{11}$$

where the square root sign refers to the positive root of the sine of the angle. The ± depends on the sign of sin x_5 and sin x_6. As this system cannot determine the signs of all the angles we take sin x_5 positive.

Substituting into equation (6) we obtain a polynomial in the variable x_3 and the constants A_i (the density matrix elements). By writing equation (6) as

$$A_6 - \text{Right Hand Side} = 0$$

it is possible to find the values of x_3 such that the function

$$F = A_6 - \text{Right Hand Side} = 0$$

The polynomial contains, in general, two solutions for which x_3 is real and positive. The general structure of the function F is shown in Fig. A2.1 (a). By making a computer search along x_3 these roots may be found; the two roots are called Solution 1 and Solution 2, the root with the slightly larger value of x_3 being Solution 1. The two solutions correspond to the classic up-down ambiguity for $\pi - \pi$ phase shifts, described figuratively in Fig. A2.2, related to the phase shift interchange

$$\delta_s' = \frac{\pi}{2} - \delta_s + \delta_p$$

Occasionally the data takes the function F above the x_3 abcissa as shown in Fig. A2.1 (b). In this case the minimum of F has to be taken as the best possible solution of the system of equations. This did not happen in this analysis for $|t| < 0.3\ (\text{GeV}/c)^2$.

Once x_3 has been found the other parameters may be determined using equations (7) to (10). A similar method of solving these equations has been given by Estabrooks and Martin [Refs. 53, 54].

The errors on the parameters x_i were determined from the error matrix relation (to first order):-

$$\underline{M} \cdot \underline{\Delta x} = \underline{\Delta A}$$

or

$$\begin{pmatrix} \frac{\partial A_1}{\partial x_1} & \frac{\partial A_1}{\partial x_2} & \cdots \\ \frac{\partial A_2}{\partial x_1} & & \\ \vdots & & \end{pmatrix} \begin{pmatrix} \Delta x_1 \\ \Delta x_2 \\ \vdots \end{pmatrix} = \begin{pmatrix} \Delta A_1 \\ \Delta A_2 \\ \vdots \end{pmatrix}$$

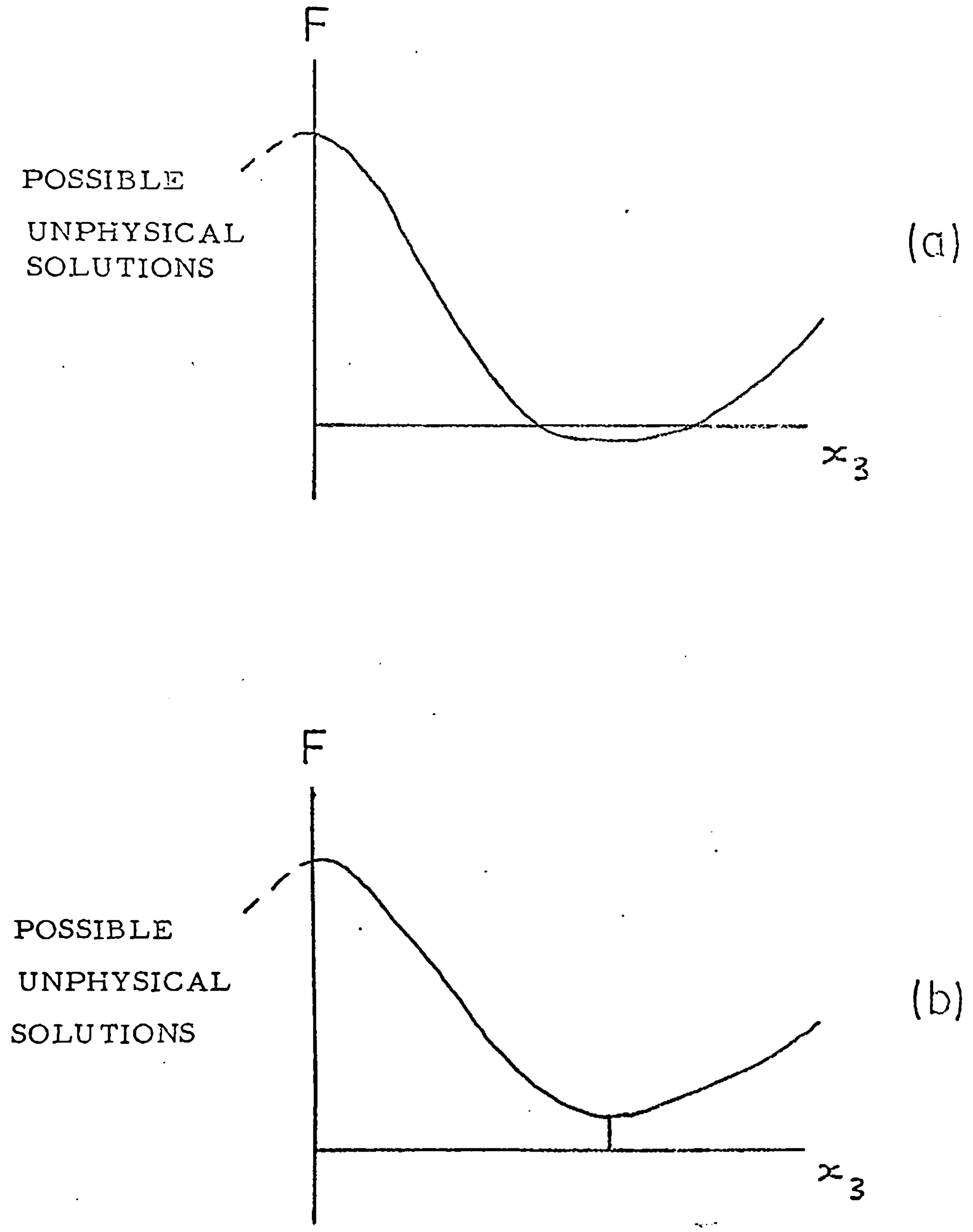

Fig. A2.1. Variation of the Function F

(a) with solutions

(b) no solutions

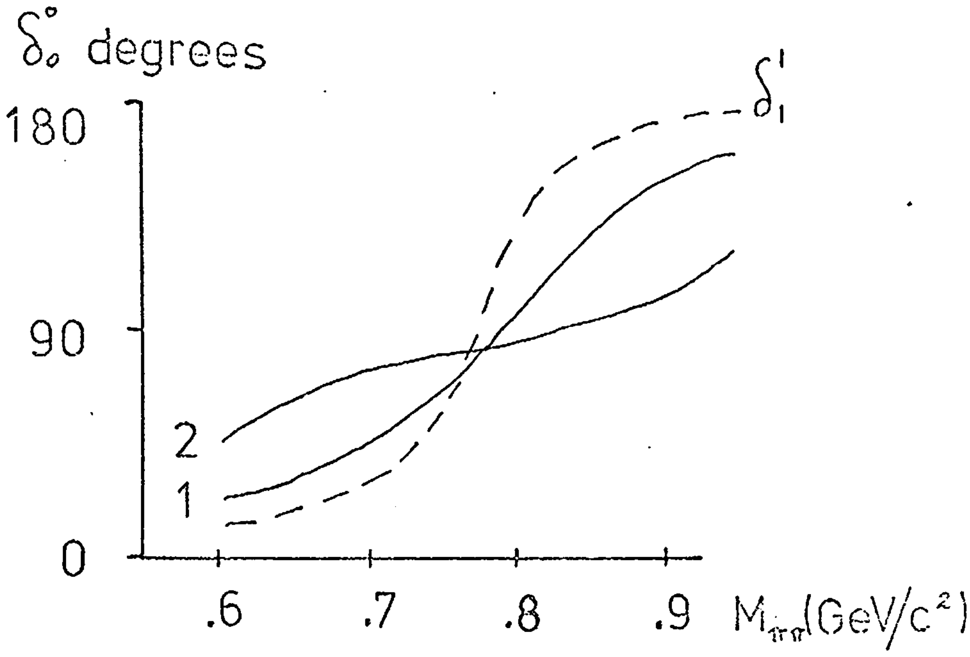

<u>sol 1</u>

$\theta^{11}_{10} > 0$

θ^{10}_{00} small

<u>sol 2</u>

$\theta^{11}_{10} \approx 0$

θ^{10}_{00} large

$$\left[\frac{M_s}{M_o}\right]_{\text{sol 2}} > \left[\frac{M_s}{M_o}\right]_{\text{sol 1}}$$

Fig. A2.2 Schematic Diagram of the UP-DOWN Ambiguity with respect to Amplitude Analysis

Once each root of F has been found, the matrix M may be ennumerated from the parameters x_i. The relation shows to first order the change in each parameter x_i which would result from a change in each constant A_i. The root position may be slightly shifted by going to a system x_i' and A_i'. Then we obtain:-

$$\underline{M}\ (\underline{x} - \underline{x}') = \underline{A} - \underline{A}'$$

$$\underline{x} = (\underline{M}^{-1})\ \underline{A} - (\underline{M^{-1}})\ \underline{A}' + \underline{x}'$$

i.e. $$\sigma^2 x_i = \sum_{ij} [(M^{-1})ij]^2 \ \sigma^2 A_j$$

where $\sigma^2 x_i$ is the variance of each parameter x_i.

It is assumed in this method that the data values A_i are uncorrelated which is not strictly true in this case and which enlarges the errors obtained for the parameters x_i.

APPENDIX 3

Helicity Amplitudes for ρ^o production in the Williams model.

In this appendix we give a brief description of the amplitudes used in calculating the predictions of the Williams model for ρ^o production. These amplitudes have been previously given by Williams [Ref. 32] and by Morgan [Ref. 30] for production of L = 1 and L = 2 dipion states in the high energy limit.

At our energy we are not able to make all the high energy approximations. However, we do assume that $|t|$ is small compared with $|t\ \mathrm{max}|$. [$|t\ \mathrm{max}|$ is the maximum value of $|t|$].

The only non-zero t-channel amplitude for elementary one pion exchange is given by [Ref. 55].

$$T_{++}^{o} = \frac{\sqrt{-t}}{(t - \mu^2)} \tau^L \tag{1}$$

Here the upper index of the amplitude refers to the dipion helicity and the lower index to the helicity transformation at the nucleon vertex.

Also we define

$$\tau = \left\{[t - (m + \mu)^2] [t - (m - \mu)^2]\right\}^{1/2} \tag{2}$$

with L the angular momentum of the dipion state (L = 1 for the ρ^o) and m the dipion mass.

In (1) a possible collimation factor $e^{Bt/2}$ has been suppressed.

Upon crossing into the s-channel, a rotation operation is necessary of the form

$$\begin{bmatrix} H^{L\mu}_{++} \\ H^{L\mu}_{+-} \end{bmatrix} = d^{L}_{\mu o}(\chi) \begin{bmatrix} \cos x & \sin x \\ -\sin x & \cos x \end{bmatrix} \begin{bmatrix} T^{o}_{++} \\ 0 \end{bmatrix} \tag{3}$$

where χ and x are the crossing angles at the meson and baryon vertices respectively [Ref. 56] and $d^{L}_{\mu o}(\chi)$ is the rotation matrix for a dipion state of spin L. The s-channel amplitudes $H^{L\ \mu}_{\lambda\ \lambda'}$ are as described in Chapter 5. The angles χ and x are defined by

$$\cos x = \cos\left(\frac{\theta_s}{2}\right)\sqrt{\frac{t\ min}{t}} \tag{4}$$

$$\sin x = \sin\left(\frac{\theta_s}{2}\right)\sqrt{\frac{t\ max}{t}} \tag{5}$$

$$\sin\chi = \frac{-2m\sqrt{s\,(t\ min - t)\,(t - tmax)}}{\sigma\,\tau} \tag{6}$$

$$\cos\chi = \frac{-[\,(s + m^2 - m_N^2)\,t + (s - m^2 - m^2_N)\,(m^2 - \mu^2)\,]}{\sigma\,\tau} \tag{7}$$

In these formulae, θ_s is the s-channel centre of mass scattering angle (and is related to t by $\sin\frac{\theta_s}{2} = \sqrt{\frac{t_{min} - t}{-t_{max}}}$)

$$\text{and}\quad \sigma = [\,(s - (m + m_N)^2)\,(\,s - (\,m - m_N)^2)\,]^{\frac{1}{2}} \tag{9}$$

with m_N equal to the nucleon mass.

One obtains the following s-channel amplitudes from the t-channel amplitude $T_{++}{}^{o}$ of equation (1) [to each amplitude the value of n,

($n = |\mu + \lambda' - \lambda|$), the net helicity flip, has been added].

$$H^{11}_{+-} = -\frac{1}{(t-\mu^2)} \sin^2\left(\frac{\theta_s}{2}\right) \frac{\sqrt{2}\, m \sqrt{s}\, (-t_{MAX})^{3/2}}{\sigma} \qquad n = 0 \quad (10a)$$

$$H^{10}_{+-} = -\frac{1}{(t-\mu^2)} \sin\left(\frac{\theta_s}{2}\right) \frac{B(t) \sqrt{-t_{MAX}}}{\sigma} \qquad n = 1 \quad (10b)$$

$$H^{1-1}_{+-} = -\, H^{11}_{+-} \qquad n = 2 \quad (10c)$$

$$H^{11}_{++} = \frac{1}{(t-\mu^2)} \sin\left(\frac{\theta_s}{2}\right) \frac{\sqrt{2}\, m \sqrt{s}\, \sqrt{-t_{MIN}} \sqrt{-t_{MAX}}}{\sigma} \qquad n = 1 \quad (10d)$$

$$H^{10}_{++} = \frac{1}{(t-\mu^2)} \quad \frac{B(t) \sqrt{-t_{MIN}}}{\sigma} \qquad n = 0 \quad (10e)$$

$$H^{1-1}_{++} = -\, H^{11}_{++} \qquad n = 1 \quad (10f)$$

with $B(t) = (s + m^2 - m_N^2)\,(m^2 + t) - 2\,m^4$ (11)

The Williams model amplitudes are now easily obtained from equations (10) by retaining in each amplitude only a t - dependence $\sin^n\left(\frac{\theta s}{2}\right)$ all other t - dependent factors (i.e. further powers of $\sin \frac{\theta_s}{2}$, B (t) and Z (t)) are set equal to their values at the pion pole, $t = \mu^2$. The $\sin^n\left(\frac{\theta_s}{2}\right)$ ($\sim (-t)^{n/2}$) is the only part of the amplitude which depends on both t and helicity and which is required by angular momentum conservation about the beam direction. Furthermore, Williams considers the remainder of each amplitude to be collimated in a similar way. This is a model-dependent result which derives from assuming a similar form-factor type behaviour in t for the remainder of each amplitude (at least over a small range at low $|t|$).

For the limit $s \to \infty$ we obtain the three amplitudes we observe in the amplitude analysis.

$$H^{1\,1}_{+\,-} = \frac{\sqrt{2}\, m\, \mu^2}{(t - \mu^2)} \qquad n = 0 \qquad (12a)$$

$$H^{1\,0}_{+\,-} = - \frac{1}{(t - \mu^2)}\, m^2 \sqrt{-t} \qquad n = 1 \qquad (12b)$$

$$H^{1\,-1}_{+\,-} = \frac{1}{(t - \mu^2)} \sqrt{2}\; m\,(-t) \qquad n = 2 \qquad (12c)$$

In fitting the data Williams allows a common overall collimation factor, $\phi(t)$. Recombining the $|\mu| = 1$ components into the contributions $M_{\pm} = H^{1\,1}_{+\,-} \pm H^{1\,-1}_{+\,-}$ one obtains

$$M_o = H^{1\,0}_{+\,-} = \frac{-\sqrt{-t}\; m^2}{(t - \mu^2)}\, \phi(t) \qquad (13a)$$

$$M_+ = -\sqrt{2}\; m\, \phi(t) \qquad (13b)$$

$$M_- = \frac{(t + \mu^2)}{(t - \mu^2)} \sqrt{2}\; m\, \phi(t) \qquad (13c)$$

REFERENCES

1. 2m User's Handbook
   U.5. Beam User's Handbook; C.E.R.N. 1970

2. H.A. GORDON; Ph.D. Thesis, Univ. of Illinois 1970

3. Particle Data Group; Rev. of Mod Phys., Vol. 45, No. 2, Part II 1973.

4. "High Energy Particles" by ROSSI; Prentice-Hall Inc., New York 1952.

5. K.F. ALLEN; Birmingham Internal Report, Oct. 1971

6. BURREN and SPARROW; Rutherford Lab. Report, NIRL/R/14

   A.G. WILSON; Rutherford Lab. Report NIRL/M/38

7. S.W. O'NEALE, P.L. WOODWORTH et al; Birmingham Internal Reports, April and July 1972.

8. L. HULTHEN and M. SUGAWARA; Handbuch der Physik, Springer - Verlag, Berlin 1957. Vol. 39 p.l.

9. M. MORAVCSIK; Nucl. Phys. 7, 113 (1958)

10. G.C. BENSON; Ph.D. Thesis, Univ. of Michigan 1966

11. "Scattering Theory of Waves and Particles" by NEWTON; McGraw-Hill Book Co. 1966

12. B. MUSGRAVE; Proc. Caltech Conf., Part 6, 1971.

13. J.E. BRAU et al, Phys. Rev. Lett 27, 1481 (1971)

14. J.A. CHARLESWORTH et al; Rutherford Lab. Preprint, RPP/H/116 Nucl. Phys. to be published.

15. R.L. EISNER et al; Phys. Rev. 164, 1699 (1967)

    K.J. FOLEY et al; Phys. Rev. Lett. 19, 397 (1967)

    E.W. ANDERSON et al; Phys. Rev. Lett 25, 699 (1970)

16. R.L. EISNER; C.E.R.N./D. Ph. II/Phys. 73-9.

17. J. QUINQUARD; Ph.D. Thesis, Univ. of Paris 1968

18. J.D. JACKSON; Nuovo Cimento 34, 1644 (1964)

19. R. GLAUBER; Phys. Rev. 100, 242 (1955)

20. C. WILKIN; Phys. Rev. Lett 17, 561 (1966)

21. G.F. CHEW and F.E. LOW; Phys. Rev. 113, 1640 (1959)

22. A.D. MARTIN and P. ESTABROOKS; Proc. of Daresbury Meeting on Pion Exchange 1973.

G. FOX; ZGS Workshops, Summer 1971, Vol 2, ANL/HEP - 7208

23. G. GRAYER et al:- C.E.R.N. - Munich 17.2 GeV/c π^-p Experiment.

24. R. ODORICO; Phys. Lett. 38B, 411 (1972)

25. See for example

S.D. PROTOPOPESCU et al; Berkeley Preprint LBL-970

G. GRAYER et al; Proc. Philadelphia Conf. April 1972

26. P. ESTABROOKS and A. D. MARTIN; Phys. Lett 41B, 350 (1972)

27. P. SONDEREGGER and P. BONAMY; Lund Conf. 1969

P. SONDEREGGER; Stony-Brook Conf. 1969

28. L. GUTAY; Phys. Rev. Lett 30, 465 (1973)

29. J.A.J. MATTHEWS et al; Nucl. Phys. B32, 366 (1971)

30. D. MORGAN; Rutherford Lab. Preprint RPP/T/27

31. P.E. SCHLEIN; Phys. Rev. Lett 19, 1052 (1967)

C.D. FROGGART and D. MORGAN; Phys. Lett. 40B, 655 (1972)

32. P.K. WILLIAMS; Phys. Rev. 181, 1963 (1969)

P.K. WILLIAMS; Phys. Rev. D1, 1312 (1970)

33. J.D. KIMEL and E. REYA; Phys. Lett 42B, 249 (1972)

34. P. ESTABROOKS and A.D. MARTIN; C.E.R.N. TH - 1661

35. J.H. SCHARENGUIVEL et al; Phys. Rev. 186, 1387 (1969)

36. See also Ref. 32

G. KANE; Proc. Argonne Conf. 1969 plus discussion between KANE and GUTAY at the end of this paper

37. J.P. BATON et al; Phys. Lett 33B, 528 (1970)

38. W.D. APEL et al; Phys. Lett 41B, 542 (1972)

39. A. SKUJA et al; Phys. Rev. Lett 31, 653 (1973)

40. D. MORGAN and G. SHAW, Phys. Rev. D2, 520 (1970)

41. G. ASCOLI et al; Phys. Rev. Lett 21, 1712 (1968)

42. J.C. ANDERSON et al; Carnegie-Mellon Univ. Preprint - Submitted to Phys. Rev. Lett.

43. N.N. BISWAS et al; Phys. Rev. 5D, 1564 (1972)

44. J. BERNSTEIN and G. FEINBERG; Nuovo Cimento 25, 1343 (1962)

45. L. BANYAI and V. RITTENBERG; Nucl. Phys. B15, 199 (1970)

46. R. EHRLICH et al; Phys. Rev. Lett. 20, 686 (1968)

47. GARFINCKEL et al; Phys. Rev. 186, 1400 (1969)

48. J. BENECKE and H.P. DURR; Nuovo Cimento, 56, 269 (1968)

49. G. WOLF; Proc. Argonne Conf. 1969

50. H.P. DURR and H. PILKUHN; Nuovo Cimento, 40, 899 (1965)

51. B.Y. OH et al; Phys. Rev. D1, 2494 (1970)

52. J. BARTSCH et al; Nucl. Phys. B22,109 (1970)

53. P. ESTABROOKS and A.D. MARTIN; C.E.R.N. TH- 1668

54. P. ESTABROOKS - Rutherford Laboratory Talk 1972

55. "The Interactions of Hadrons" by H. PILKUHN; North- Holland Pub. Co., 1967.

56. "Elementary Particle Theory" by A.D. MARTIN and T.D. SPEARMAN; North-Holland Pub. Co., 1970.

35. J.H. SCHARENGUIVEL et al; Phys. Rev. 186, 1387 (1969)

36. See also Ref. 32

G. KANE; Proc. Argonne Conf. 1969 plus discussion between KANE and GUTAY at the end of this paper

37. J.P. BATON et al; Phys. Lett 33B, 528 (1970)

38. W.D. APEL et al; Phys. Lett 41B, 542 (1972)

39. A. SKUJA et al; Phys. Rev. Lett 31, 653 (1973)

40. D. MORGAN and G. SHAW, Phys. Rev. D2, 520 (1970)

41. G. ASCOLI et al; Phys. Rev. Lett 21, 1712 (1968)

42. J.C. ANDERSON et al; Carnegie-Mellon Univ. Preprint - Submitted to Phys. Rev. Lett.

43. N.N. BISWAS et al; Phys. Rev. 5D, 1564 (1972)

44. J. BERNSTEIN and G. FEINBERG; Nuovo Cimento 25, 1343 (1962)

45. L. BANYAI and V. RITTENBERG; Nucl. Phys. B15, 199 (1970)

46. R. EHRLICH et al; Phys. Rev. Lett. 20, 686 (1968)

47. GARFINCKEL et al; Phys. Rev. 186, 1400 (1969)

48. J. BENECKE and H.P. DURR; Nuovo Cimento, 56, 269 (1968)

49. G. WOLF; Proc. Argonne Conf. 1969

50. H.P. DURR and H. PILKUHN; Nuovo Cimento, 40, 899 (1965)

51. B.Y. OH et al; Phys. Rev. D1, 2494 (1970)

52. J. BARTSCH et al; Nucl. Phys. B22, 109 (1970)

53. P. ESTABROOKS and A.D. MARTIN; C.E.R.N. TH- 1668

54. P. ESTABROOKS - Rutherford Laboratory Talk 1972

55. "The Interactions of Hadrons" by H. PILKUHN; North- Holland Pub. Co., 1967.

56. "Elementary Particle Theory" by A.D. MARTIN and T.D. SPEARMAN; North-Holland Pub. Co., 1970.